The Pennsylvania State University

The Graduate School

COMPLIANT MECHANISMS USING SUPERELASTIC NITINOL

A Thesis in

Mechanical Engineering

by

Jiening Liu

Submitted in Partial Fulfillment
of the Requirements
for the Degree of

Master of Science

December 2012

The thesis of Jiening Liu was reviewed and approved* by the following:

Mary I. Frecker
Professor of Mechanical Engineering
Thesis Advisor

Jason Z. Moore
Assistant Professor of Mechanical Engineering

Karen A. Thole
Professor of Mechanical Engineering
Department Head of Mechanical and Nuclear Engineering

*Signatures are on file in the Graduate School

ABSTRACT

NiTiNOL which is a nickel and titanium alloy exhibits the superelastic effect at desired temperature so that it can provide large strain up to 10% under loading. The superelastic property of NiTiNOL could benefit compliant mechanisms which relays on elastic deformation of the material to transfer motion, force or energy. The goal of this research is to explore compliant mechanisms using superelastic NiTiNOL in new or current applications and evaluate the performance of new designed compliant mechanisms with superelastic NiTiNOL. Two applications are investigated in this thesis.

First, a device that can provide articulation to surgical tool tips is needed in natural orifice transluminal endoscopy surgery (NOTES). We propose a compliant articulation structure that uses superelastic NiTiNOL to achieve a large deflection angle and force in a compact size. Six geometric parameters are used to define this structure, and constraints based on the fabrication process are imposed. Using finite element analysis, a family of designs is evaluated in terms of the free deflection angle and blocked force. The same family of designs is evaluated for both NiTiNOL and stainless steel. It can be seen that significant benefits are observed when using NiTiNOL compared to 316 stainless steel; a maximum free deflection angle of 64.8^{o} and maximum blocked force of 24.7 N are predicted. The designs are refined to avoid stress concentrations, and design guidelines are recommended. The meso-scale articulation structure is fabricated using both a Coherent Avia Q-switched, 355 nm laser and a Myachi Unitek 200 W single mode pulsed fiber laser with active water cooling. Select fabricated structures are then tested to validate the finite element models.

Second, a contact-aided compliant mechanism, or compliant spine, that was previously developed in our Engineering Design and Optimization Lab at the Pennsylvania State University is redesigned and modeled using superelastic NiTiNOL. The new one-joint compliant spine using superelastic NiTiNOL can reduce 50% of the size compared to Delrin design while not exceeds the weight of Delrin design. The tip deflection and length ratio of NiTiNOL design is about 150% of Delrin design, which means that NiTiNOL could make the compliant spine much smaller thus possibly lighter while still provide large deformation.

TABLE OF CONTENTS

LIST OF FIGURES

LIST OF TABLES

ACKNOWLEDGEMENTS

I would like to first gratefully acknowledge my advisor Dr. Frecker for her guidance and advice while getting my Masters. I would like to thank Dr. Moore for serving as a reader for my thesis. I would also like to extend my thanks to both Dr. Trethewey and Dr. Chen who recommended me to join the Master program at Penn State.

There are many other people who helped me greatly during my time at Penn State. I would like to thank Benjamin Hall and Dr. Ted Reutzel at Penn State Applied Research Lab for fabricating the laser micro-machined parts as well as Brennan DeCesar at Miyachi Unitek. I would also like to thank Dr. Zoubeida Ounaies and Hassene Ben Atitallah who kindly provided their lab equipment and helped me with my experiment. I would like to extend my thanks to NDC and Johnson Matthey companies who provided free samples of NiTiNOL tubes for our research.

I would also like to thank my fellow EDOG lab members for their support and friendship. Finally, I would like to extend a huge thank you to my friends and especially my family for all of their love and support through my time at Penn State.

NOMENCLATURE

E^A = Young's modulus of Austenite
μ = Poisson's ratio of NiTiNOL
α = Material response ratio between tension and compression
$\bar{\varepsilon}_L$ = Maximum residual strain
σ_s^{AS} = Starting stress value for the forward phase transformation
σ_f^{AS} = Final stress value for the forward phase transformation
σ_s^{SA} = Starting stress value for the reverse phase transformation
σ_f^{SA} = Final stress value for the reverse phase transformation
d = Outside diameter of compliant articulation structure
a = Ring thickness of compliant articulation structure
L = Length of compliant articulation structure
w = Width of compliant articulation structure
t = Thickness of compliant articulation structure
r = Fillet radius of compliant articulation structure
l = Unsupported length of the columns at compressive load
k = Least radius of gyration

Chapter 1

Background and Motivation

1.1 Introduction

NiTiNOL (nickel and titanium alloy) exhibits the superelastic effect at desired temperature so that it can provide large strain up to 10% under loading. The high flexibility of this material could enhance the performance of compliant mechanisms which are flexible mechanisms that transfer motion, force or energy using elastic deformation. With the use of superelastic NiTiNOL, a very large recoverable deformation can be achieved compared to the same compliant mechanisms of traditional materials like stainless steel or ceramics.

The goal of this research is to examine the potential use of superelastic NiTiNOL to improve the performance of compliant mechanisms. Two different applications are studied using superelastic NiTiNOL. The first application is a compliant articulation structure for endoscopic surgery. A compliant articulation structure using superelastic NiTiNOL is proposed to provide large deflection in limited space during endoscopic surgery. The articulation structure is modeled in ANSYS and then fabricated using laser processing. An experiment is carried out to verify the simulation. A similar approach is extended to a compliant spine for flapping wings unmanned aerial vehicles. Due to the superealstic effect, compliant mechanisms can not only provide large recoverable deformation but can be small, compact, and light weight.

1.2 Research Objectives

The objectives of this research include the design, analysis and fabrication of compliant mechanisms using superelastic NiTiNOL. The main research objectives are as follows:

1. Model superelastic effect in ANSYS, finite element analysis software, as well as large deformation and contact.
2. Design and analyze the compliant articulation structure using superelastic NiTiNOL.
3. Fabricate and test a proof of concept device for the compliant articulation structure.
4. Design and analyze the compliant spine using superelastic NiTiNOL.

1.3 Literature Review

This section will present related work on NiTiNOL, compliant mechanisms, NOTES, articulation structures used in endoscopic surgeries, compliant spine for flapping wing vehicles, and then fabrication of meso-scale structures.

1.3.1 Superelastic NiTiNOL

In the 1960s, Buehler and Wiley developed a series of nickel-titanium alloys with a composition of 53% to 57% nickel by weight. Those alloys can regain their original shape after a thermal cycle when severely deformed with residual strains of 8~15% [1]. Since it was developed at the Naval Ordnance Laboratory, the new alloy was named NiTiNOL [2].

NiTiNOL was further studied later on with efforts by many researchers. Two major effects of NiTiNOL were called the shape memory effect and superelastic effect [3]. The name shape memory effect explains itself. When the alloy is permanently deformed at a low temperature, this permanent deformation could be fully recovered if the alloy is heated above a critical temperature. In fact, both effects are attributed to phase transformation between two crystal structures: martensite and austenite. Phase transformation could be induced in several ways, such as heating and applying load [4]. Generally speaking, any energy input to NiTiNOL could cause phase transformation, if it is large enough. Thus, not only raising the temperature, but electricity and manipulating the magnetic field could also help NiTiNOL achieve a shape memory effect as well. Figure 1-1 shows a typical phase transformation during the shape memory effect. Four critical temperatures, austenite start temperature, austenite finish temperature, martensite start temperature and martensite finish temperature, are defined to characterize this transformation. The shape memory effect can be explained in more detail as two kinds: one-way shape memory effect (Figure 1-2(a)) and two-way shape memory effect (Figure 1-2(b)) [3]. Normally, the shape memory effect requires the working temperature to be lower than the martensite finish temperature so that the alloy is full of the marteniste structure. In order to fully recover deformation, the deformed NiTiNOL needs to be heated above the austenite finish temperature, where a more stable crystal structure is formed and rearranged.

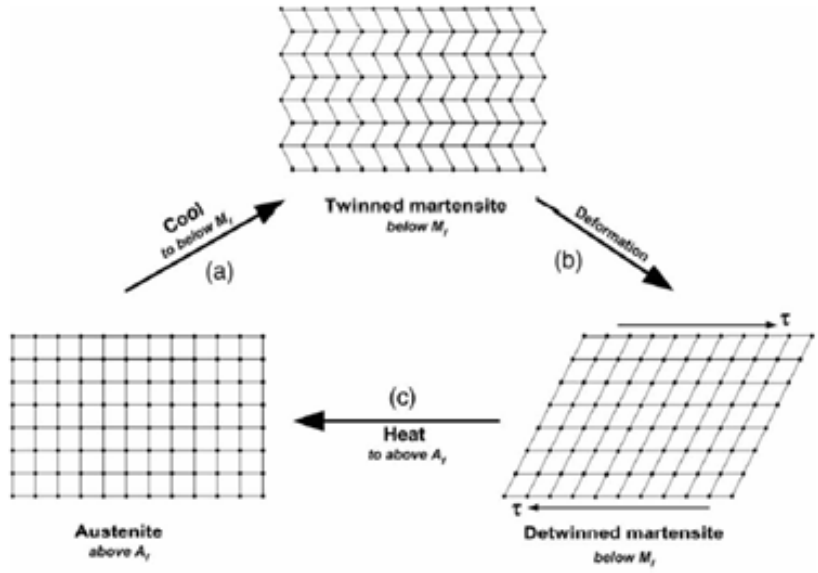

Figure 1-1 Microstructure variation during shape memory effect [4].

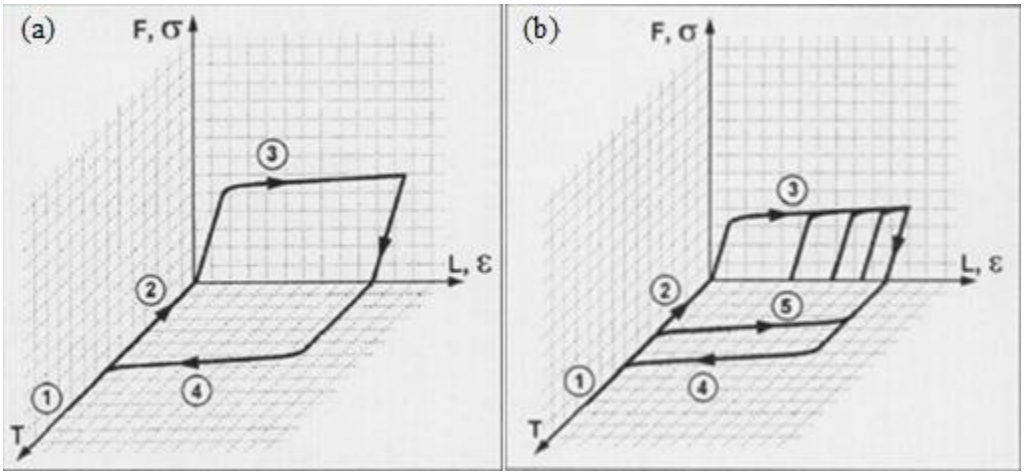

Figure 1-2 (a) One-way shape memory effect; (b) Two-way shape memory effect [3].

The superelastic effect, on the other hand, does not require temperature variation. However, this effect is only preserved at a temperature that is higher than the austenite finish temperature. In other words, only an austenite structure has the superelastic effect. In the superelastic effect, phase transformation is induced by external loading or stress increase within the material. Figure 1-3 presents a schematic of the phase transformation and mechanical behavior at different strain levels as the material is loaded until it fractures.

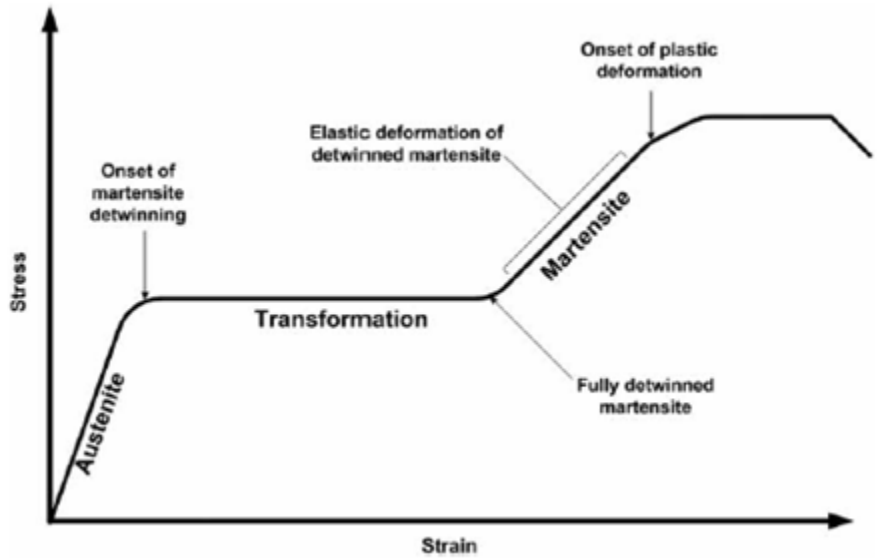

Figure 1-3 Phase transformation during superelastic effect [4].

The physical and mechanical properties of NiTiNOL can be tailored by adjusting the composition of nickel and titanium or adding a third metal into the alloy [5]. That is to say, decreasing the amount of titanium or increasing the nickel within the alloy can lower phase transformation temperatures. For medical devices that take advantage of the superelastic effect, the working temperature, which is room temperature or human body temperature, should be higher than austenite finish temperature [6]. However, the austenite finish temperature should not deviate far away from the temperature in the application since the superelastic effect only exists within a certain temperature range [7]. Figure 1-4 shows data from a NiTiNOL wire with an austenite finish temperature of 11^{o}C undergoing a tension test at different temperatures from -100 ^{o}C to 150^{o}C. Starting from 100 ^{o}C, the superelastic effect no longer exists. Meanwhile, the large temperature difference between the austenite finish temperature and the working temperature could increase the phase transformation stress of NiTiNOL.

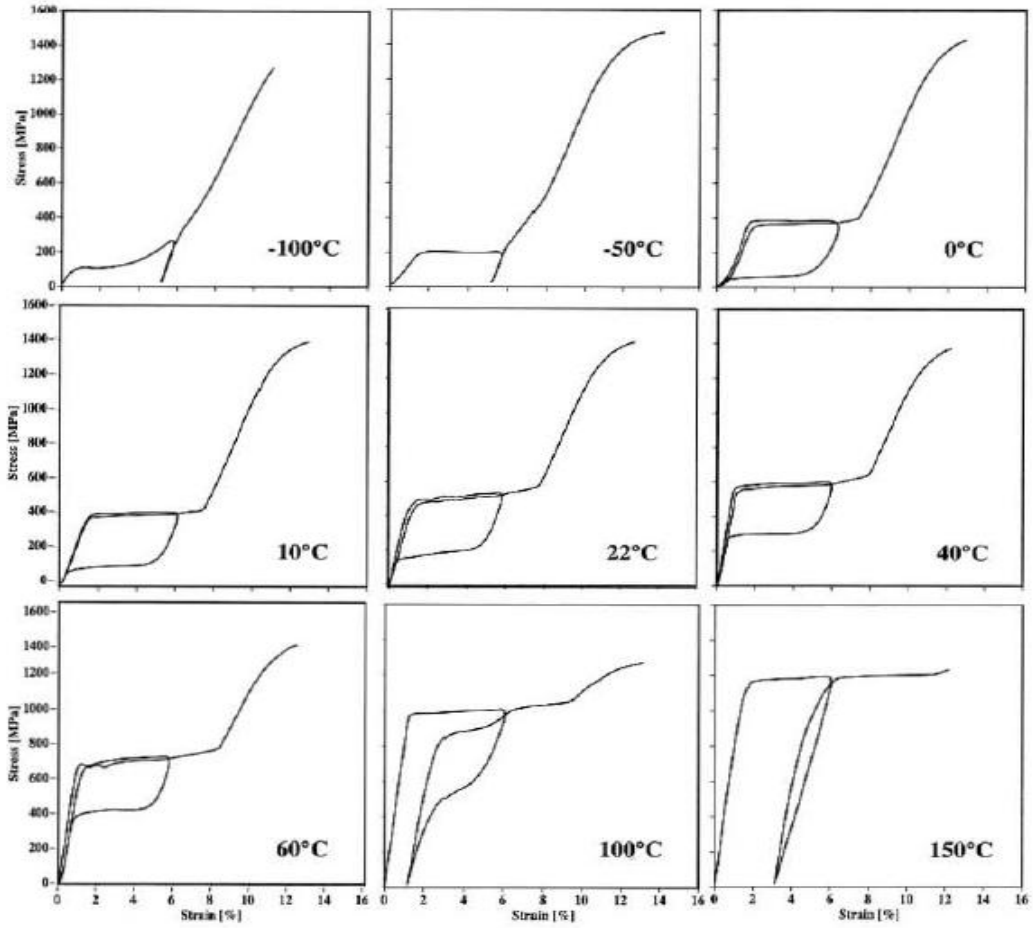

Figure 1-4 Mechanical behavior of NiTiNOL at different temperature [7].

Bio-compatibility is crucial for any material that is utilized for medical devices in surgery. The biocompatibility of NiTiNOL has been studied for a long time from different aspects. A NiTiNOL sample was immersed in human cell culture to evaluate the potential influence on bio structure. The releasing of nickel was detected during the experiment and the concentration of nickel in the culture solution stabilized after two days. The dissolution level of nickel did not induce any toxic effects in human cell proliferation or grow throughout the whole experiment [8]. Further experiments were performed using living animals where a NiTiNOL device was implanted into rats. Researchers found that the inflammation caused by NiTiNOL was very similar to stainless steel or Ti-6Al-4V which have already been commonly used in medical devices such as implants and surgical tools [9]. NiTiNOL's biocompatibility was also studied based on different fabrication methods. Powder metallurgy (PM) and arc melting made NiTiNOL samples were both tested with cells growing on them. Healthy cells proved the biocompatibility

for both fabrication processes. Meanwhile, PM shows a higher corrosion resistance to living cells compared to arc melting [10]. Furthermore, the passive titanium-oxide layer found on the NiTiNOL surface could protect corrosion and stop nickel oxidation [11, 12]. Surface treatment such as electropolishing, heat treatment (in air and in a salt bath), and nitric acid passivation were studied and have all shown their ability to improve the corrosion resistance of NiTiNOL which is essential for implants [13].

With its good biocompatibility, NiTiNOL has been used widely in medical devices. One of the most commonly seen applications is artery stent (Figure 1-5). The NiTiNOL stent can withstand large deformation and be compressed to fit in a small catheter. The catheter is then inserted into the blood vessel and moved to the place where the vessel collapsed. At the right location, the stent is released. Due to its superelastic effect, the stent will restore its original shape which helps open the blood vessel [14]. A similar idea is applied in interventional radiology for the treatment of Atrial-Septal defect using a double umbrella (Figure 1-6) made of NiTiNOL [15]. NiTiNOL also has been used to fabricate micro-forceps (Figure 1-7) for retrieval of intravascular objects. Due to the compliance of NiTiNOL, the forceps could fit into a 0.89-mm diameter working channel and open up to 12.5 mm of jaw distance [16]. Besides those meso-scale devices, NiTiNOL, especially porous NiTiNOL, is utilized more in implants for bone fracture due to its similar mechanical behavior as natural human bones [17].

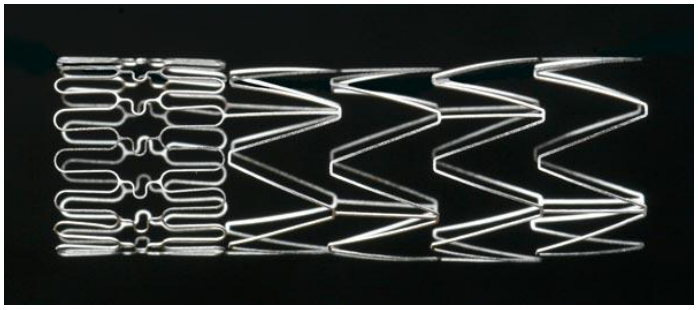

Figure 1-5 NiTiNOL stent for vascular support [18].

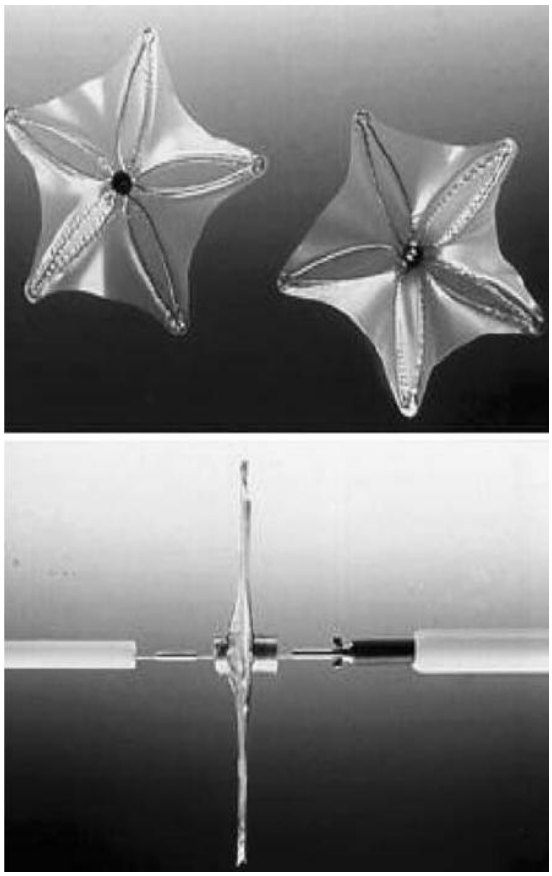

Figure 1-6 Double umbrella releases from a catheter and expands to full size [15].

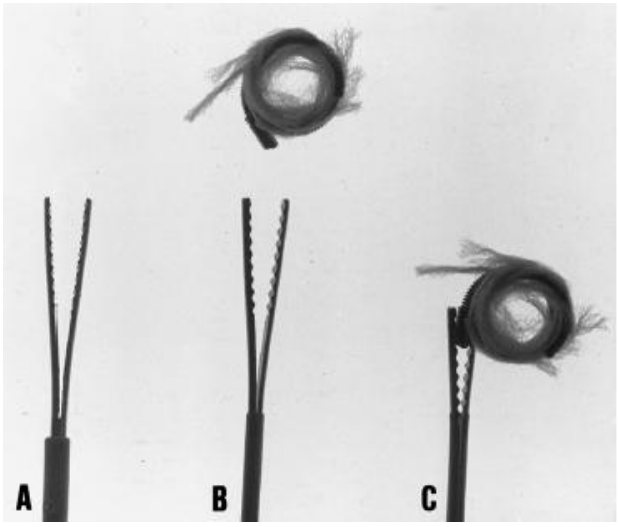

Figure 1-7 NiTiNOL micro-forceps are retrieving objects in experiment [16].

1.3.2 Compliant Mechanisms

Compliant mechanisms are flexible mechanisms that transfer motion, force, or energy using the benefit of elastic deformation [19]. These single-piece compliant mechanisms are designed to transfer motion, force, or energy via elastic deformation of the members rather than from conventional rigid body kinematic pairs [20]. Compliant mechanisms offer the benefits of not needing assembly, lack of wear and backlash, and no lubrication requirements [21]. They can also achieve very high precision which is highly desired in surgery. One drawback of compliant mechanisms is that they may not be able to produce the same range of motion as rigid link mechanisms [19]. One way to resolve the problem is to use a highly flexible material, like superelastic NiTiNOL, which can go under a large strain during operation and provide larger range of motion.

Several research efforts have been conducted recently on designing small surgical tools for minimally invasive surgery (MIS) and natural orifice trans-luminal endoscopic surgery (NOTES) using compliant mechanisms. A three-fingered, fully compliant and monolithic kidney-gripper was developed for laparoscopic and robot-assisted surgery [22]. Figure 1-8 shows the CAD model of a compliant kidney gripper and a kidney. The gripper, manufactured using wire electrical discharge machining (EDM), can fold and fit into a 15-mm diameter scope. During surgery, the gripper can deploy and expand to be 70 mm in diameter [22]. Figure 1-9 is a compliant multifunctional scissors-forceps for minimally invasive surgery. The scissors-forceps, fabricated using wire EDM, can fit into a 5-mm diameter laparoscopic port. It can achieve both cutting and grasping actions with a smooth surface and a textured surface, respectively [23]. A compliant suturing instrument for NOTES can be seen in Figure 1-10. A prototype was fabricated using wire EDM and can pass through a 3.3-mm working channel in an endoscope. An experiment was conducted successfully to place two sutures in an ex-vivo porcine model [24]. More recently, the compliant narrow-gauge forceps in Figure 1-11 was developed for NOTES [25]. It was fabricated using the lost mold rapid infiltration forming (LMRIF) method [25-28] which allows for production of large numbers of parts simultaneously. The forceps is a 1 mm in diameter, however it still provides blocked forces as high as 1.5N and pull-off force of 1.2N [25].

The monolithic nature of compliant mechanisms is ideal for small-scale surgical applications [22]. With novel materials and an advanced fabrication process, new designs could be developed and built to help surgeons with NOTES.

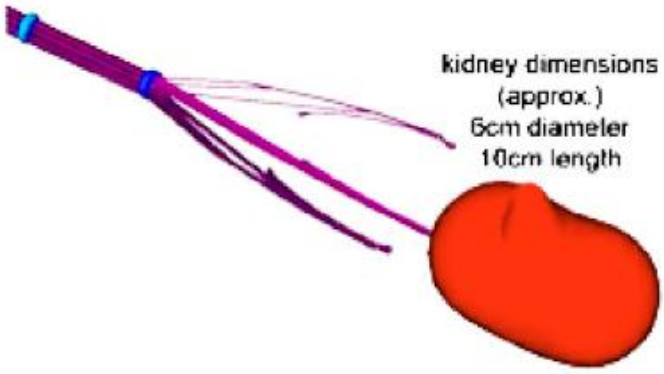

Figure 1-8 CAD model of a compliant kidney gripper and a kidney [22].

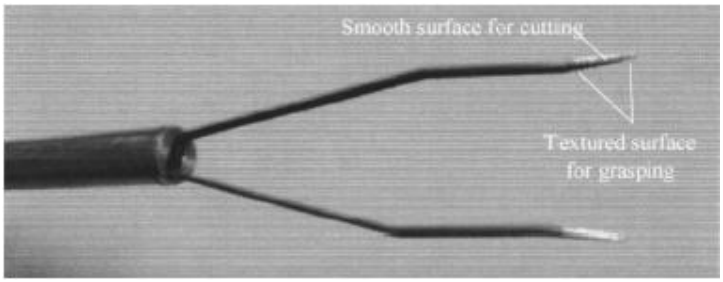

Figure 1-9 Compliant multifunctional scissors-forceps can performing cutting and grasping during surgery [23].

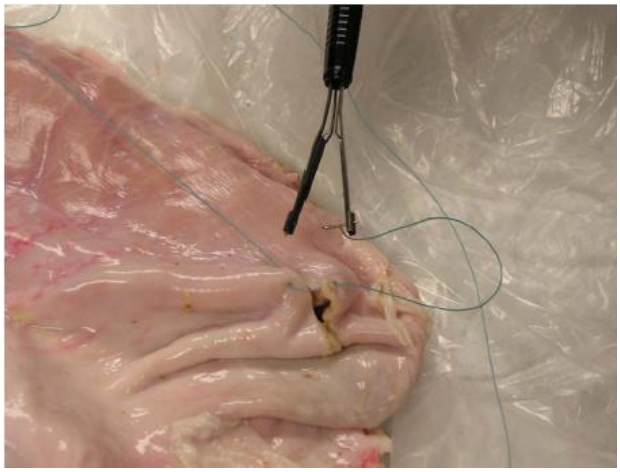

Figure 1-10 Compliant suturing instrument tested on porcine stomach [24].

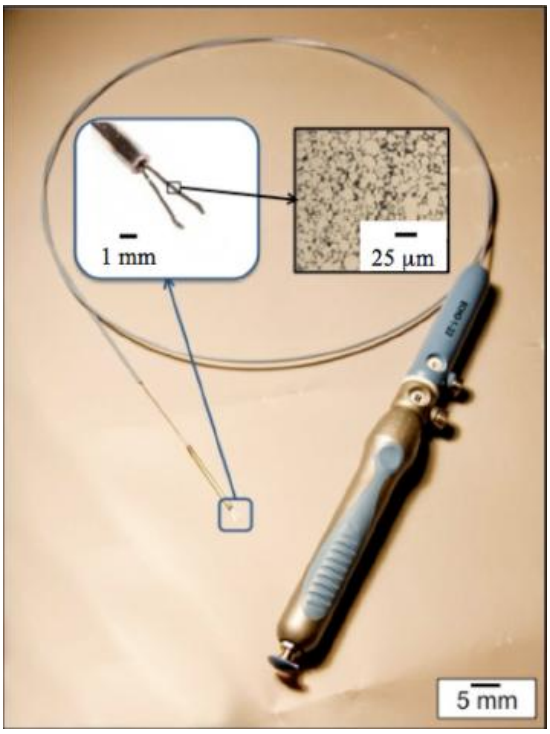

Figure 1-11 Assembled meso-scale forceps prototype for NOTES [25].

1.3.3 Natural Orifice Translumenal Endoscopic Surgery (NOTES)

Natural Orifice Transluminal Endoscopic Surgery (NOTES) is a surgical technique whereby 'scarless" abdominal operations can be performed using an endoscope passed through a natural orifice, then through an internal incision thus avoiding any external incisions or scars [29]. The history of NOTES could date back to 1901 when Dimitri Oskarovich Ott performed the first endoscopic examination of the peritoneal cavity through the vagina [30] which has become a common access point in NOTES. Later in 1976, the concept of NOTES was first described in a transcolonic appendectomy surgery [31]. After that, a number of NOTES procedures were performed as shown in Figure 1-12.

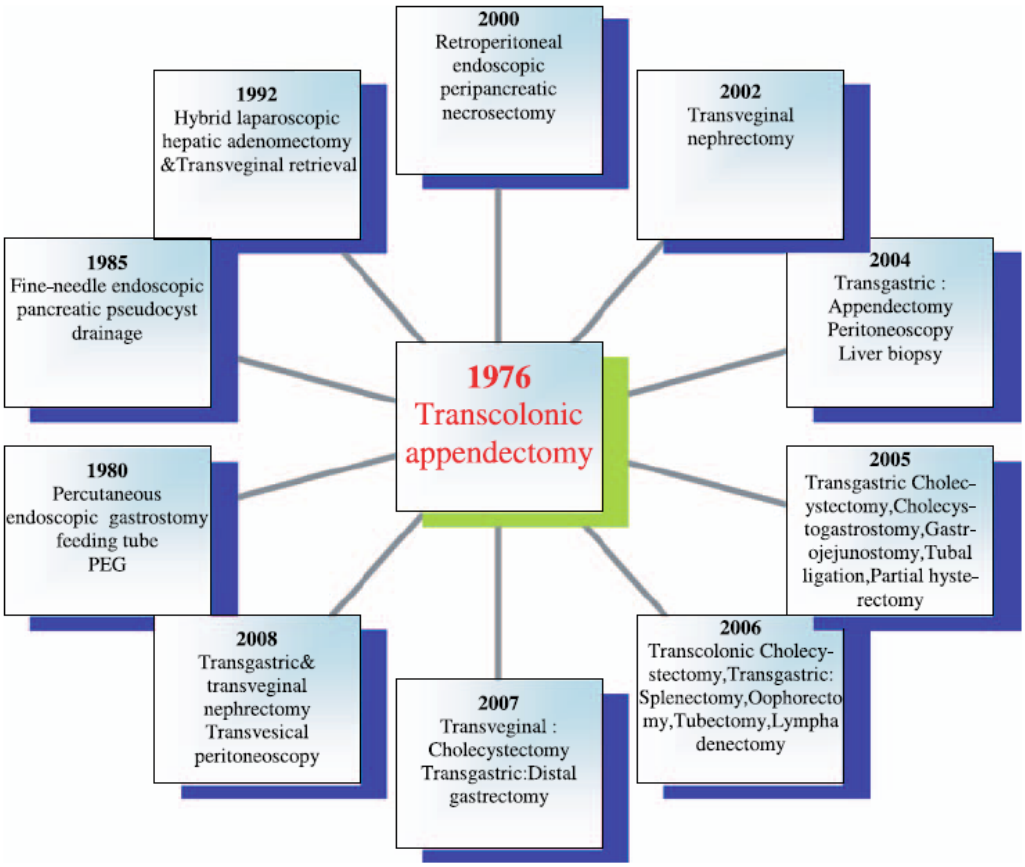

Figure 1-12 Time line development of different NOTES procedures [31].

Today's NOTES was officially introduced in 2005 when fourteen leaders from the American Society of Gastrointestinal Endoscopy (ASGE) and the Society of American Gastrointestinal and Endoscopic Surgeons (SAGES) agreed on the potential advantages of performing surgeries through natural orifices [32]. A working group that is dedicated to the development of NOTES was also formed soon after the discussion and it is known as the Natural Orifice Surgery Consortium for Assessment and Research (NOSCAR) [32, 33]. NOSCAR registered human NOTES in the United States in 2008 with the support of both SAGES and ASGE [34] and holds the annual International Symposium on Natural Orifice Surgery to encourage the development of NOTES.

In the past, complex surgeries required large incisions to have a successful outcome. However, laparoscopic surgery already reduces the incision to one or several ports whose size is only a few millimeters. Furthermore, NOTES could possibly replicate laparoscopic procedures in

an “incisionless” manner [35]. Many successes in laparoscopic surgery have made surgeons and researchers optimistic about NOTES.

Unlike traditional open surgeries or laparoscopic surgeries which require incisions through the skin, an endoscope is inserted through a natural orifice, and an intentional puncture is made through one of the viscera (e.g. stomach, vagina) to access the abdominal cavity and perform the intra-abdominal surgery [36]. An example of a NOTES procedure, transgastric gallbladder removal, is shown in Figure 1-13. A flexible endoscope is inserted through the patient’s month, and an incision is then made through the stomach wall which allows the endoscope to access the abdominal cavity and remove the gallbladder. Figure 1-14 shows a general endoscope for NOTES. It usually contains light sources (light guided lens), a camera (objective lens) and one or more working channels.

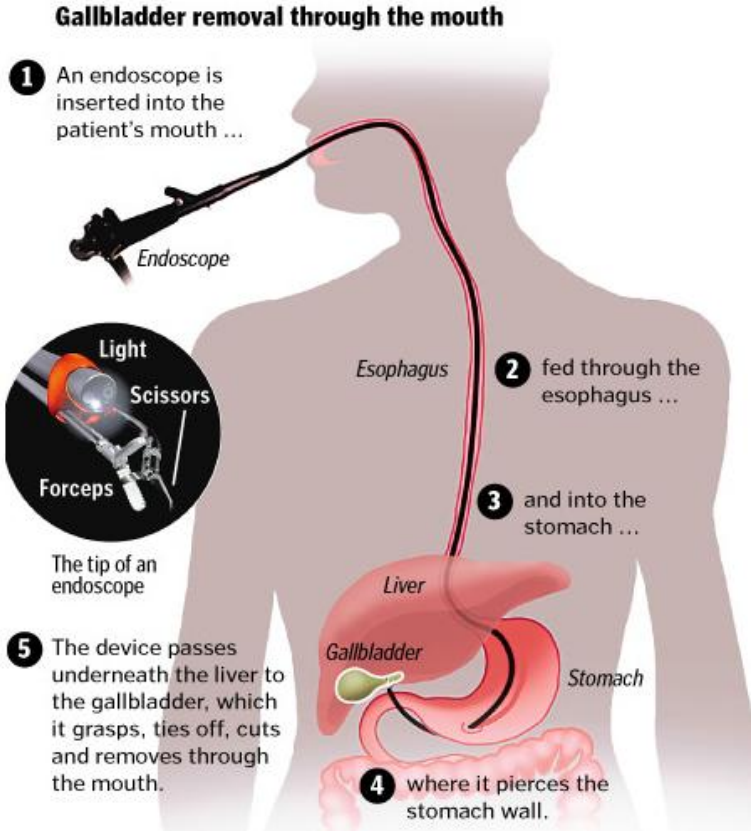

Figure 1-13 Transgastric gallbladder removal surgery [37].

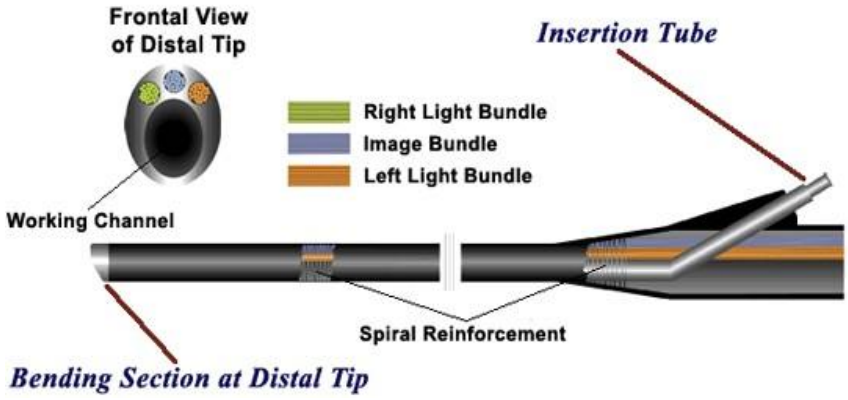

Figure 1-14 A general endoscope for NOTES [24].

This less invasive approach to surgery reduces pain and risk of infection, as well as intra- and post-operative complications. This leads to faster recovery times and better cosmesis compared to traditional or laparoscopic surgery [31-33]. Furthermore, surgeons believe that NOTES could be performed without anesthesia [36, 38]. Therefore, patients could undergo NOTES in the intensive care unit or endoscopic suite in an out-patient procedure, rather than a standard operating room, which can possibly reduce procedure costs [38]. Many potential benefits have driven surgeons and researchers to conduct experiments to evaluate NOTES.

So far, from animal and cadaver tests, several natural orifices have been examined as routes for access to the peritoneal cavity. These include oral, anal, vaginal, or urethral orifices, although the optimal access paths and methods are still under investigation [34]. The size of the orifice will impose a limitation on the size of endoscope as well as the surgical tools that pass through it. Cadaver experiments proved it was difficult to insert an 18-mm endoscope into natural orifices and a 16-mm endoscope showed better performance [39]. Furthermore, the urethral orifice has an even smaller diameter. Thus, smaller, flexible and precisely maneuverable endoscope platforms need to be developed [40].

With the help of newly developed platforms and devices for NOTES, surgeons are able to apply this novel idea to patients. A review shows that 432 cases have been treated using NOTES [41]. It is expected that NOTES will continue to advance in the future. The type of surgeries that could be possibly performed using NOTES include cholecystectomy, appendectomy, esophageal myotomy, nephrectomy, partial gastrectomy, adjustable gastric band, sigmoidectomy, liver resection, splenectomy, hernia repair, renal cyst resection, PEG rescue, proctosigmoidectomy, and transanal pull-through [41]. And if we classify current NOTES surgeries by where the incision is made, they can be characterized as transvaginal, transgastric, transrectal, transophageal,

transvesical and transcolonic [34, 41]. Every new access or incision that is discovered for NOTES may require corresponding new devices such as endoscopes, suturing tools, etc.

Although surgeons have encountered hundreds of cases using NOTES, only 9.7% of these total 432 cases were conducted using pure NOTES [41]. It means that only about 42 cases in the literature are performed using purely flexible endoscope access from natural orifices. The other 90.3% of cases, called hybrid-NOTES, have been performed with transabdominal assistance and thus an incision has to be made through the skin. Surgeons indicated that safe access into the peritoneum and inadequate flexible instrumentation are the two primary reasons for the predominance of the hybrid approach [41]. Several other issues have limited the development of NOTES. Current flexible endoscopes have issues with stability. New techniques need to be introduced for endoscopes to meet both flexibility and stability requirements [41]. One approach to compromising between flexibility and stability is to add a locking system which fixes the endoscope after it reaches the desired position. Surgeons have also found it difficult to access the retroperitoneal cavity due to the abundant adipose (loose connective tissue composed of adipocytes) tissue in humans which limits the scope view [42]. A tapered shape head on the scope or forceps that could help split out those heavy tissues might help in this situation. Insufflation during NOTES is also not as easy as in laparoscopic surgery based on current devices. Flexible endoscopes usually lack both the ability to deliver a high flow of CO_2 to create adequate pneumoperitoneum and the safety mechanism of a laparoscopic insufflator [43]. Therefore, surgeons have to get help from laparoscopic devices used through the abdomen to provide insufflation and monitor pressure in the peritoneal cavity [41, 43-45]. The current NOTES process also lacks effective closure and suturing devices which are essential to prevent new complications and increase recovery [38, 46]. Another example is a self-approximating translumenal access technique (STAT, Figure 1-15) which creates better access through the stomach to abdominal cavity [47]. Although forceps have been developed to help this special incision, instruments that can help provide faster access to the abdominal cavity are preferred [48].

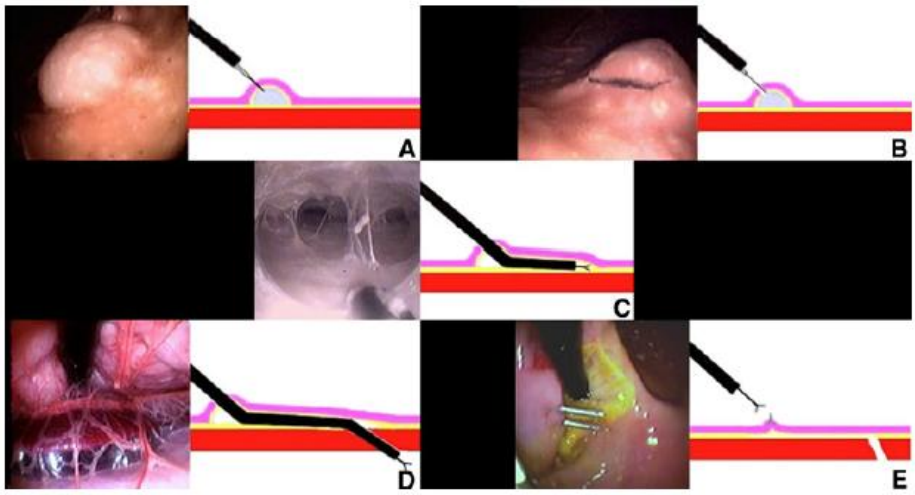

Figure 1-15 Self-approximating translumenal access technique (STAT): (A) A submucosal cushion is created in the gastric submucosal space. (B) A 1- to 1.5-cm incision is created with a needleknife. (C) A flexible rat tooth grasping forceps is used for sharp and blunt dissection to create a submucosal tunnel. (D) A 1- to 1.5-cm linear incision in the seromuscular layer is made and may be dilated with a 16-mm radial expansion balloon, completing the gastrostomy. (E) At scope withdraw the Z-tract naturally self-approximates, and the mucosa is closed with endosclips for added security[47].

NOTES has been increasingly regarded as the future of surgery. It could bring us many advantages compared to traditional or laparoscopic surgery. With its novel access to reach unhealthy organs and other benefits associated with that access, great efforts have been made by researchers and doctors to further develop this process. The untraditional access of NOTES requires a small diameter endoscope, thus making small and effective surgical tools in a magnitude of meso-scale highly needed. The small scale and other constraints require innovative design, new materials, and a suitable fabrication process.

One goal of this research is to design, fabricate, and, finally, test a compliant articulation structure. The compliant articulation structure is designed to enlarge the working space during NOTES by providing a more flexible tool. With the help of this articulation structure, the efficiency of NOTES could be improved, and could broaden the range of surgeries that could be performed using NOTES.

1.3.4 NOTES Instruments and Articulation Structures

Surgeons and engineers have been working together to develop new effective devices for NOTES since 2005, when it was introduced. There are some practical devices developed so far, and some of them have already been commercialized. They can be divided into two categories: platforms and tool tips.

Three new endoscopic platforms have been developed. One is called the "R" scope from Olympus, Tokyo Japan in Figure 1-16(a) [43]. It can be flexible during insertion and lock its shape during surgery, but the complex control system and lack of pulling force limit its performance [43]. Another commercial platform for NOTES is called Transport in Figure 1-16(b) [43]. It can also switch between flexible mode and rigid mode depending on the operation. The disadvantages are a complex hand control system and lack of triangulation [43]. The third platform in Figure 1-16(c) is called the Cobra. It has a similar flexible and locking system. Also, it provides better triangulation when compared to the previous two platforms. However, the cable-driven control system is imprecise and surgeons are unable to change tool tips on a daughter scope during surgery unless the whole endoscope is retracted [43].

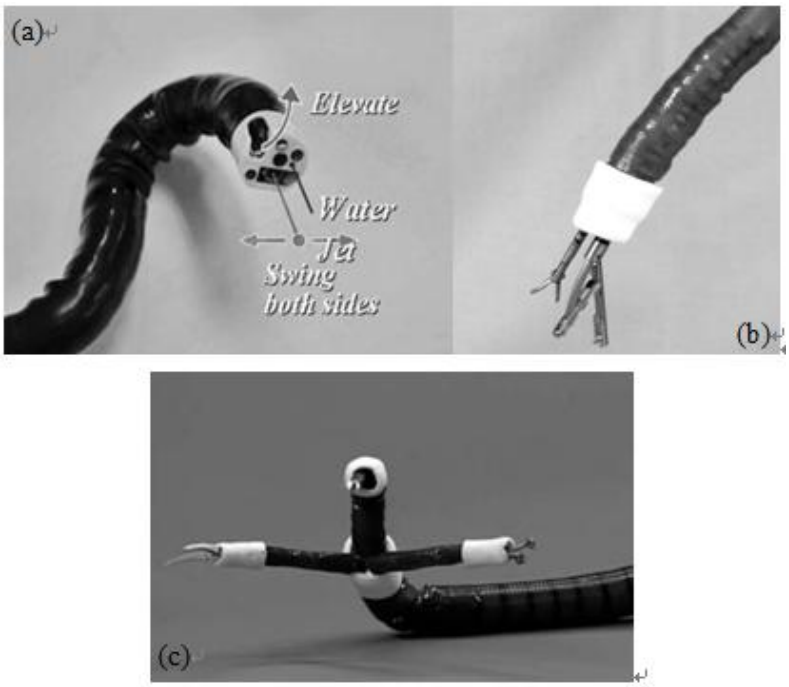

Figure 1-16 (a) The "R" scope from Olympus, Tokyo, Japan; (b) Transport from USGI medical, San Capistrano, CA, USA; (c) The Cobra from USGI medical, San Capistrano, CA, USA [43].

More NOTES platforms are under development in research labs. A master and slave translumenal endoscopic robot in Figure 1-17 was developed at the National University of Singapore, Singapore [49]. The whole platform consists of a master console, a telesurgical workstation, and a slave manipulator which holds two end-effectors [50]. The control system is modeled after human hands. Thus, two end-effectors can move and operate according to the hand motions of a surgeon [49]. However, an overtube has to be inserted first in order to insert the robot with ease and avoid unintentional scratching by the slave manipulator [51]. Also, with only two tool tips, it is sometimes difficult or impossible to complete the procedure. Surgeons also have to fully remove the platform in order to switch to a third surgical tool.

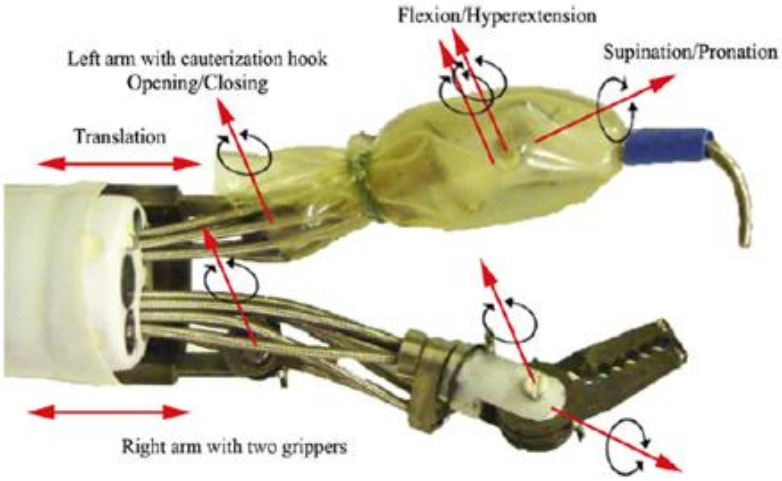

Figure 1-17 The slave manipulators [50].

Unlike traditional NOTES platforms with endoscopes and tool tips, a novel robotic system using a dexterous, miniature, in-vivo robot was developed at the University of Nebraska-Lincoln [52]. This new platform in Figure 1-18 explored a different path by sending the whole robot into the peritoneal cavity to perform NOTES. Nevertheless, inability to change tool tips during surgery, stability, and triangulation issues need to be resolved before being used on patients.

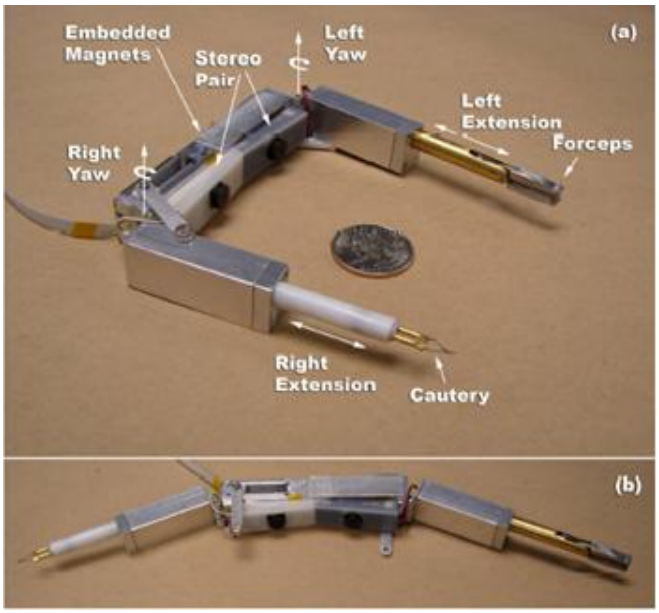

Figure 1-18 A dexterous miniature in-vivo robot for NOTES [53].

In addition to platforms with endoscope and control systems, surgical tool tips are desperately needed for NOTES. There are dozens of tools used in traditional or laparoscopic surgeries such as scalpels, forceps, suction, grasper, etc. Similar instruments are needed in NOTES as well, if surgeons are trying to duplicate traditional or laparoscopic surgeries using NOTES [32].

Figure 1-19 shows an electro-cautery hook, scissors, needle driver, grasper, Kelly, and dissector which were originally used in laparoscopic surgery and then modified to fit in a NOTES endoscope [54]. These tool tips have a diameter of 7.2 mm since they are designed for laparoscopic surgery [54]. The size of these instruments limits the number of tools that can be inserted through the endoscope at the same time. Therefore, it will affect the duration of surgery and could make it impossible to perform complex surgeries. Multifunctional forceps which can fit into a 3.0-mm endoscope were developed at the Pennsylvania State University [48], and shown in Figure 1-20. The multifunctionality of the forceps refers to the ability to both spread and grasp tissue. The dual functionalities and small size are ideal for NOTES. An even smaller compliant forceps (Figure 1-21) which can fit into a 1-mm working channel were also developed [25, 55]. This monolithic forceps combined with LMRIF method demonstrates the potential of fabrication of large arrays of meso-scale tool tips for NOTES.

Figure 1-19 Modified tool tips originally from Laprotek laparoscopic instruments [54].

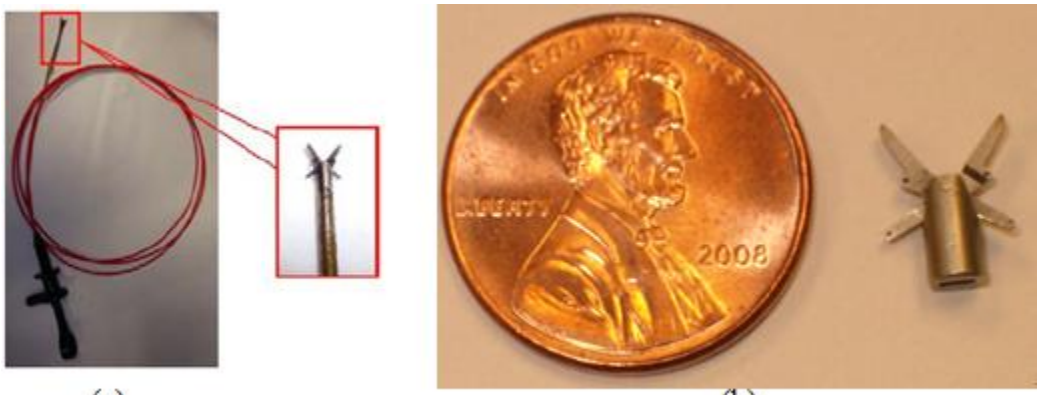

Figure 1-20 (a) The multifunctional forceps are installed at the end of a endoscopy [48]; (b) The multifunctional forceps can both spread and grasp tissues [56].

Figure 1-21 Compliant forceps can fit into 1-mm diameter scope [57].

While development of endoscopic platforms and tool tips are essential to advancing NOTES, surgeons encounter difficulties in steering tool tips during surgery. Efforts have been put

into development of different articulation structures including endoscope articulation and tip articulation [58].

A flexible-and-rigid articulation structure (Figure 1-22) for an endoscope was developed using a thermoplastic polymer [59]. This temperature actuated polymer structure could be flexible at high temperatures (~43^{o}C) and rigid enough to carry 305g weight at low temperatures (~5^{o}C) [59]. However, lack of multi-temperature stiffness and working temperature range data has slowed down further development and optimization of this structure.

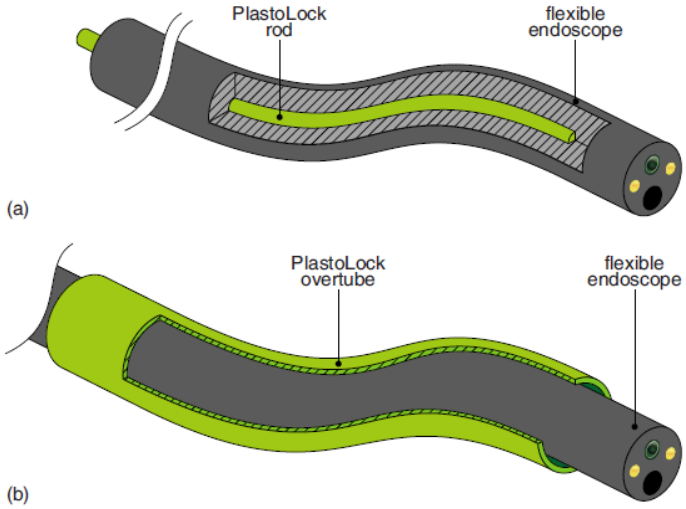

Figure 1-22 (a) PlastoLock shaft embedded in a flexible endoscope; (b) PlastoLock overtube installed outside a flexible endoscope [59].

Endoscope articulation could provide non-linear access in a large scale during insertion. However, during the surgical operation, when high precision is required and space is limited, a tip articulation structure would be highly desired. A spine-like structure (Figure 1-23) provides a way to articulate a tip tool during surgery [60]. The disposable design of the structure can mitigate or eliminate problems associated with the chemical colitis, cross contamination, overuse and improperly performed repairs. On the other hand, the resistive force of the organ is at minimum 0.64 N for a tip module of 11 mm in diameter and 2.9 mm in length which is the size of this articulation structure [60]. The maximum force generated by the current design is far below 0.64 N, due to the motor power and structure. Another similar design shown in Figure 1-24 and is also composed of a stack of sectors. Each sector is designed to have a maximum of 5 degrees of deflection [61], thus more sectors could give larger overall deflection. Actuated by four wires, the segmented mechanism could bend up to 90 degrees and form various configurations including the

one shown in Figure 1-24. Nevertheless, the current prototype is a scaled-up model and it is difficult to fabricate a small scale version of the structure which can fit into the working channel of an endoscope. Also, there are several common disadvantages for long, segmented structures. Current sectors can only provide a limited deflection angle. Thus, a large number of sectors is needed in order to meet the articulation requirement. What's more, the longer of those structures, the larger actuation force they require to manipulate the tip tool against tissues [60].

Figure 1-23 Spine-like articulation system using motor actuation [60].

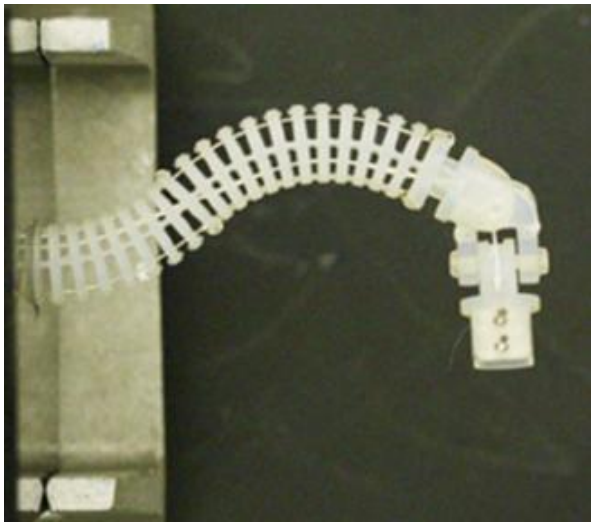

Figure 1-24 Multi-sector flexible snake driven by four cables [61].

A different design uses ball joints to achieve articulation. A prototype of the micro manipulator is shown in Figure 1-25 with diameter of 2.4 mm and bending radius of 2.45 mm [62]. Although this small structure can fit in most working channels of current endoscopes and provide deflection as large as 90 degrees, assembling of these ball joints is cumbersome and may not be suitable for a disposable instrument.

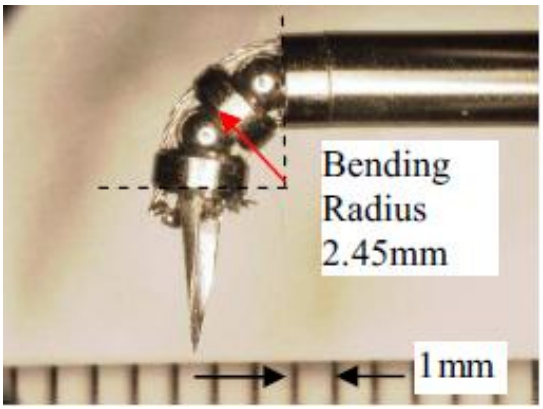

Figure 1-25 Micro manipulator using ball joint in bending position [62].

1.3.5 Flapping Wing in Unmanned Aerial Vehicles

Another application that will be discussed here using superelastic NiTiNOL is compliant spine for flapping wing. Our lab collaborating with Aimy Wissa and Dr. James Hubbard from University of Maryland has been designing and developing compliant spine used in flapping wing for years. It is worth to see how the compliant spine will behave by using superelastic NiTiNOL.

A morphing aircraft is defined as an aircraft that changes its configuration to maximize its performance at radically different flight conditions [63]. Wing morphing is naturally the most important aspect of aircraft morphing as it dictates the aircraft performance in a given flight condition [63]. Aircraft morphing concepts can be used for morphing of large-scale manned aircraft or small-scale Unmanned Aerial Vehicles (UAVs).

Flapping wing unmanned aerial vehicles (UAVs), or ornithopters, have presented the potential for advancing and revolutionizing UAV performance in both the civil and military sectors [64]. Ornithopters can combine the agility and maneuverability of rotary wing aircraft with excellent performance in low Reynolds number flight regimes [65].

Current wing reconfiguration techniques utilize rigid-link mechanisms or involve active wing reconfiguration techniques [66]. Comparing with rigid-link mechanisms and active wing reconfiguration, passive wing-shape-change mechanisms require no additional energy expenditure, and have minimal weight addition and complexity [65]. A contact-aided compliant mechanism (CCM) for passive wing reconfiguration has been developed and optimized to improve the performance of ornithopters during flight in our Engineering Design and Optimization Lab at the Pennsylvania State University [65] in Figure 1-26.

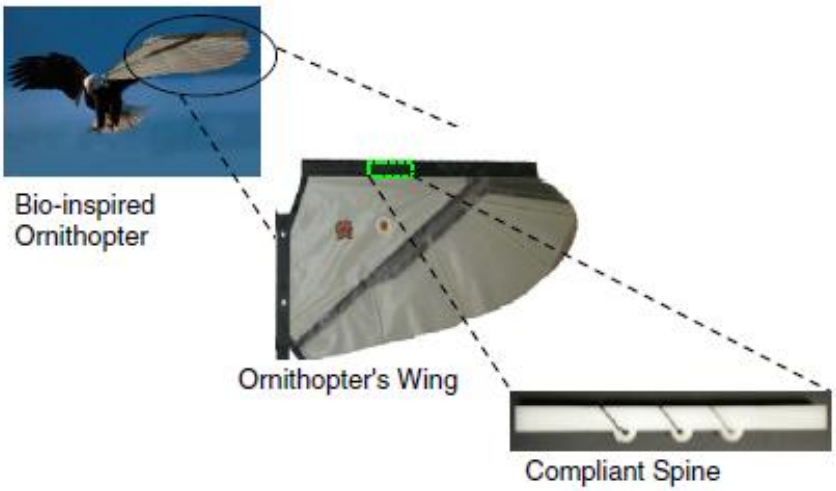

Figure 1-26 The compliant spine is inserted into the leading edge spar to mimic the function of an avian wrist [65].

The compliant spine shown in Figure 1-26 has three compliant joints. Each compliant joint consists of two major mechanisms, contact pair (illustrated as contact gap in Figure 1-27) and compliant hinge (Figure 1-27).

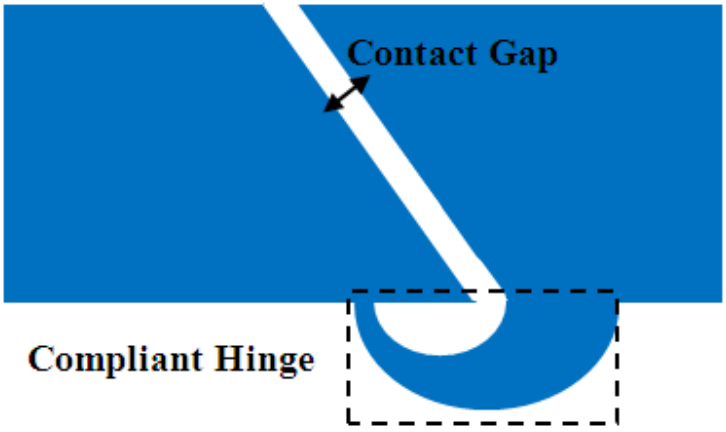

Figure 1-27 Illustration of single compliant joint consisting of one contact gap and one compliant hinge (Courtesy: Yashwanth Tummala).

The contact-aided compliant spine is inserted in the leading edge of the flapping wing. When the wing moves upward (during upstroke), the compliant joints in the compliant spine can help generate large deformation. When the wing moves downward (during downstroke), the compliant joints will also try to generate large deformation. However, contact will happen at this time so that the compliant spine becomes much stiffer and allows little deformation if the contact

gap is small. This wing shape change during flight mimics the wing flapping in the real birds, which increases the lift force during flight.

The current compliant spine for passive wing morphing is manufactured using Delrin, because of its good fatigue properties, elastic strength, manufacturability and availability [65]. However, more deflection is desired during upstroke while Delrin design could not provide such deflection within the stress limit. Additionally, the compliant spine increases the weight of wing somewhat. A lighter and smaller design will be needed to help decrease the total. Superelastic NiTiNOL is explored here for the compliant spine in order to reduce the volume, weight and increase deflection.

1.3.6 Fabrication of NiTiNOL Meso-scale Structures

Many micro-fabrication methods that have been used with different materials can also be used to fabricate NiTiNOL products. These manufacturing techniques can be classified as removal and additive approaches. Removal techniques use existing NiTiNOL material such as a film or a tube. Part of the material will be removed from the original piece, which results in the final product. For example, a robot leg (Figure 1-28) of an endoscopic capsule is cut from a plain NiTiNOL plate using wire electrical discharge machining (EDM) [67]. The resolution depends on the diameter of the wire which can be as small as 100 nanometers [68]. However, the capability of wire EDM is limited to 2D designs. Myunghoon *et al*. presented a novel bi-layer lift-off method based on photolithography to be able to fabricate large number of arrays of MEMS valve (Figure 1-29) from NiTiNOL films [69]. But the products are still constrained to 2D. A more precise laser cutting is utilized to fabricate artery stent (Figure 1-30) from a tube. With multi-axis laser machine, a complex geometry like a stent can be fabricated [70]. However, like other laser cutting process, the fabrication ability is limited by raw materials, e.g. a tube or rod.

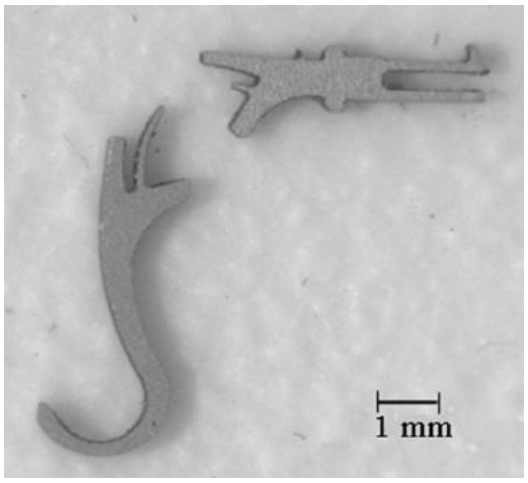

Figure 1-28 NiTiNOL robot leg fabricated using wire EDM [67].

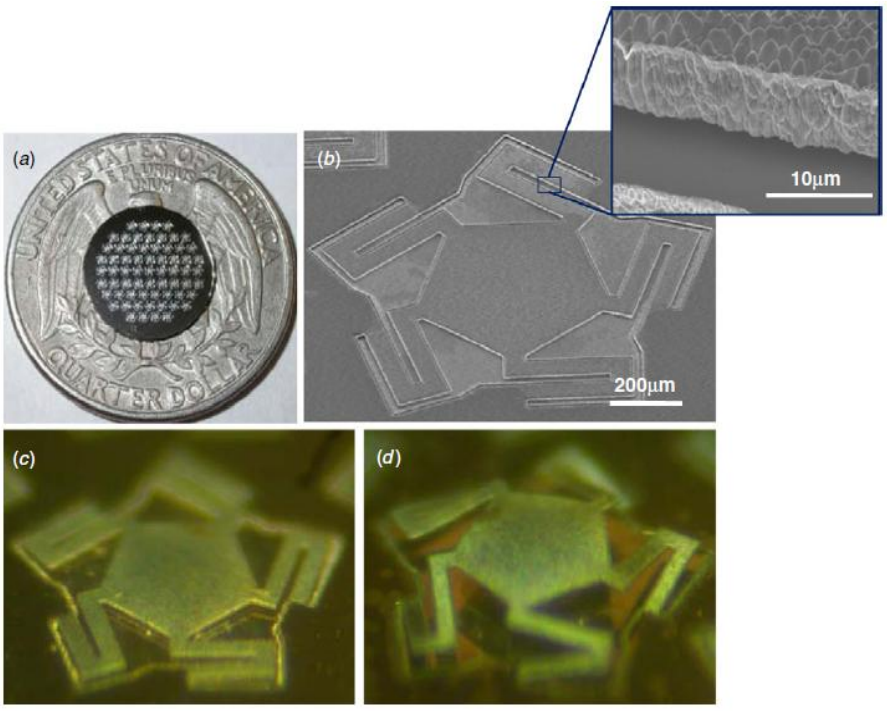

Figure 1-29 Arrays of NiTiNOL MEMS valve fabricated using bi-layer lift-off method [69].

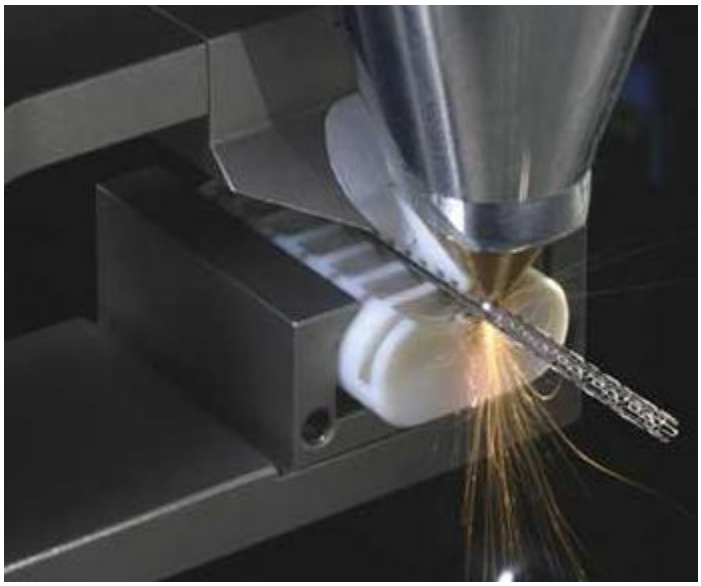

Figure 1-30 NiTiNOL stent is cut from a tube using high-precision laser processing [71].

Additive manufacturing is a more robust fabrication process that can build complex 3D parts [72]. This process makes parts by adding successive layers of the material, rather than removing the material, such that there is little or no waste. Each layer is melted according to an exact geometry defined by a three-dimensional computer aided design model. With short pulse laser, the melting zone can be minimized so that high resolution can be achieved. Additive manufacturing methods for NiTiNOL are only just beginning to be investigated, however.

1.4 Thesis Outline

This research is focused on analysis and design of different compliant mechanisms using superelastic NiTiNOL. The remainder of the thesis is organized as follows.

In this thesis, Chapter 2 presents a compliant mechanism using superelastic NiTiNOL for articulation purposes in NOTES. A parametric model is built to represent this structure. Finite element analysis is then performed to evaluate the deflection and blocked force. The design is refined to improve the performance of this structure. Finally a design guide is developed for this application.

Chapter 3 presents the fabrication of the NiTiNOL compliant articulation structure, followed by experimental validation of the previous modeling. The fabrication is done by laser processing from a NiTiNOL tube.

Chapter 4 presents another NiTiNOL compliant mechanism applied in passive morphing wings for ornithopoters. A NiTiNOL compliant spine is analyzed using finite element analysis and a comparison is made between NiTiNOL and Delrin spine.

Chapter 5 presents a summary of the work as well as major conclusions. It also presents contributions of the research, and states potential future work.

Chapter 2

Design and Analysis of Compliant Articulation Structure

This chapter details the process of designing and modeling the articulation structure. It describes the structure geometry as well as the finite element analysis used to calculate deflection and blocked force in the structure. The variables that define the articulation structure are presented followed by the constraints imposed based on available raw material, stress concentration, fabrication ability and other physical constraints.

2.1 Design Concept

Through our collaboration with Pennsylvania State University Hersey Medical Center, it was determined that a deflection of 45^{o} to 90^{o} of the tool tip is highly required during NOTES. Meanwhile, the size of this articulation structure should be small enough to go through a typical endoscopic working channel which is about 3 mm in diameter. The force that this structure can withstand should also be as large as possible to prevent failure when the tool tip moves against tissue.

In this chapter, a monolithic compliant structure is proposed. This structure would be attached to the surgical tool tip and when actuated, would allow the tool tip to articulate, or bend (Figure 2-1).

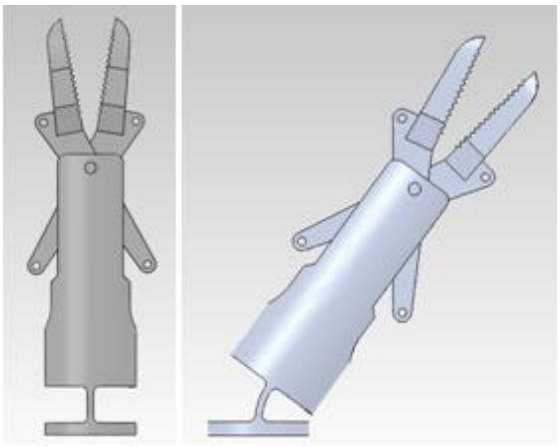

Figure 2-1 A surgical tool tip mounted on the compliant articulation structure. Articulation increases the functional space and improves dexterity of the surgical instrument.

The basic geometry of compliant articulation structure is shown in Figure 2-2. Six design parameters, including the outside diameter (d), ring thickness (a), width (w), length (L), thickness (t) and fillet radius (r), are used to define the articulation structure. In order for the device to be useful in NOTES procedures, the outside diameter of the articulation structure must be smaller than the inner diameter (ID) of the working channel of an endoscope. The rest of the five parameters have to be carefully chosen to achieve the desired performance.

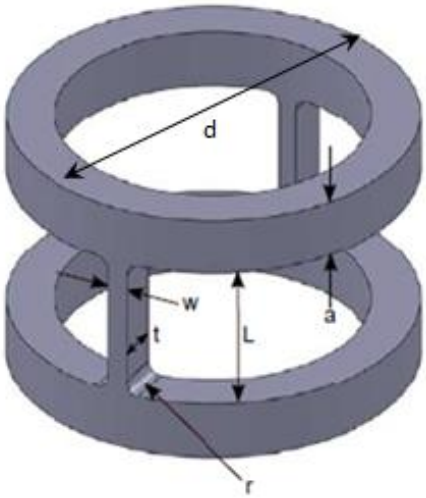

Figure 2-2 Geometric model of the compliant articulation structure, used to develop families of different designs.

The ability to articulate will allow the surgeon nonlinear access to the surgical site, which will improve dexterity and surgical efficiency in procedures such as laparoscopy or NOTES. A preliminary analysis of the compliant articulation structure design indicated that the articulation angles are quite small when using a conventional biocompatible material such as stainless steel [56]. Thus a highly flexible, biocompatible material such as superelastic NiTiNOL is needed for this compliant articulation structure. NiTiNOL can withstand very large deformations if the working temperature is above Austenite finish temperature [3]. By using NiTiNOL in the compliant articulation structure, we expect to obtain increased articulation angle and blocked force compared to stainless steel.

2.2 Modeling the Articulation Structure

Modeling of non-linearity of the NiTiNOL material will be first studied. Then the NiTiNOL is combined with the compliant articulation structure. A quasi-static analysis with large deformation will be conducted to evaluate the free articulation angle and blocked force of the structure.

2.2.1 Superelastic Model in ANSYS

Modeling of NiTiNOL has been studied for many years. The suerpelastic constitutive model has been improved from one-dimensional phenomenological characterization of pure tension [73-75] to fully three-dimensional models [76-79]. Additionally several numerical implementation methods have been developed using techniques from computational plasticity in order to realize those models computationally [80-83]. Modeling of NiTiNOL using the finite element method was integrated into commercially available software only a few years ago. ANSYS and ABAQUS implement the superelastic model of NiTiNOL developed by Auricchio and his group [79, 84, 85]. The material model has been used in varied research topics like MEMS valve, stents, bolted end-plate connections and leg designs for an endoscopic capsule [67, 86-89].

In this research, ANSYS12.1 (research version) is used for finite element analysis. The nonlinear superelastic model has already been embedded in ANSYS since its eighth version.

Though the model is named Shape Memory Alloy, it can simulate only the superelastic effect (SE) of NiTiNOL. The schematic of this model is shown in Figure 2-3 [90] in stress-strain form. A total of 8 parameters are needed for this specific material model, including Young's modulus of Austenite (E^A), Poisson's ratio (μ), material response ratio between tension and compression (α), maximum residual strain ($\bar{\varepsilon}_L$), starting stress value for the forward phase transformation (σ_s^{AS}), final stress value for the forward phase transformation (σ_f^{AS}), starting stress value for the reverse phase transformation (σ_s^{SA}), and final stress value for the reverse phase transformation (σ_f^{SA}). These material properties can be obtained from a typical tension and compression test. However, the hysteresis loops in tension and compression are different [91, 92], shown in Figure 2-4. Some significant differences are that stress at the same strain is larger in compression than in tension and the slopes of hysteresis curve are steeper in compression as well [93].

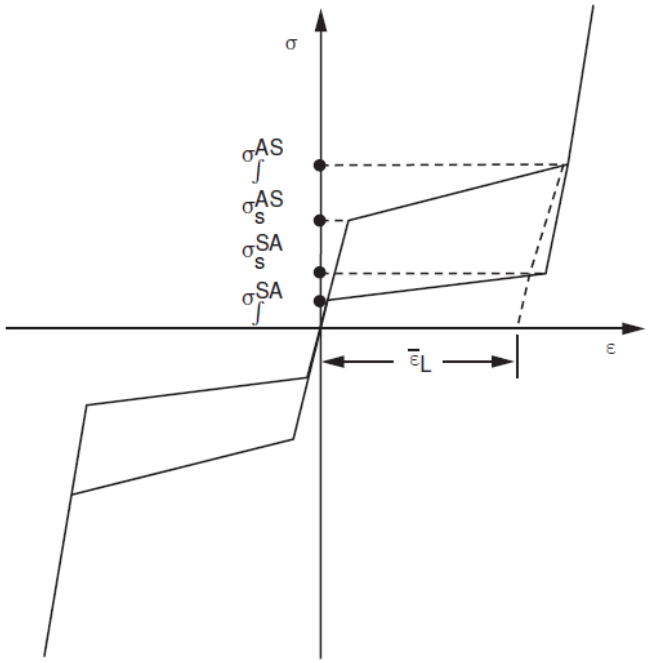

Figure 2-3 Superelastic Model in ANSYS [90].

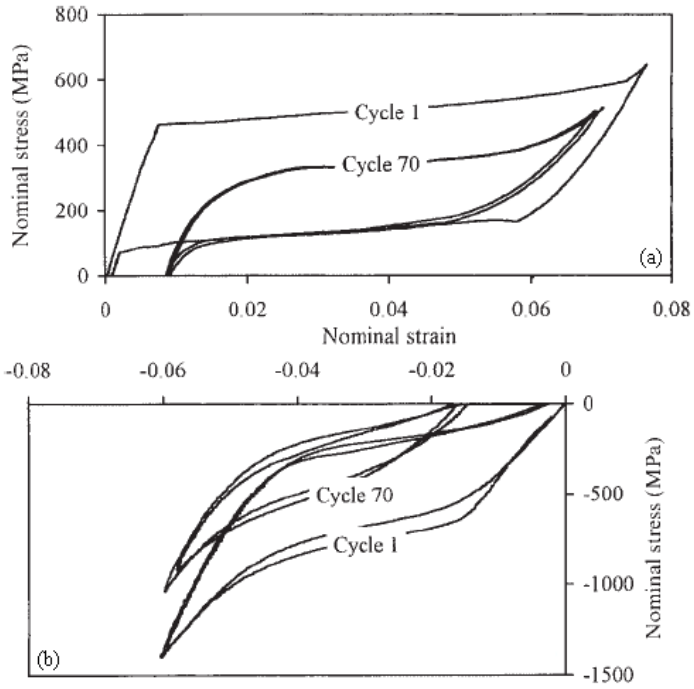

Figure 2-4 (a) Stress-strain curve at tension test; (b) Stress-strain curve at compression test [93].

In the ANSYS model, all these differences are characterized by one parameter α, which accounts only for the difference in stress at the starting stress value for the forward phase transformation, as shown in Equation (2-1). Here σ_c^{AS} is the initial value of Austenite to Martensite phase transformation in compression, and σ_t^{AS} is the initial value of Austenite to Martensite phase transformation in tension. The slopes are defined to be the same as the Young's modulus of Austenite in tension.

$$\alpha = \frac{\sigma_c^{AS} - \sigma_t^{AS}}{\sigma_c^{AS} + \sigma_t^{AS}} \qquad (2\text{-}1)$$

2.2.2 Material Model Validation

In order to have comprehensive understanding of the superelastic model, three progressive examples that appear in the literature are analyzed using finite element analysis in ANSYS. These three examples are the standard tension test simulation, cantilever beam bending simulation and an orthodontic archwire deformation simulation. All of these three simulations are

then compared with their counterpart from the literature to validate the ANSYS SMA material model.

First a tension simulation is performed and then compared to results from [67]. Since the detail dimensions of the dog bone model are not listed in the literature that we want to compare with, new dimensions (Table 2-1) are calculated to match the sizes in the literature based on ASTM standards (Figure 2-5).

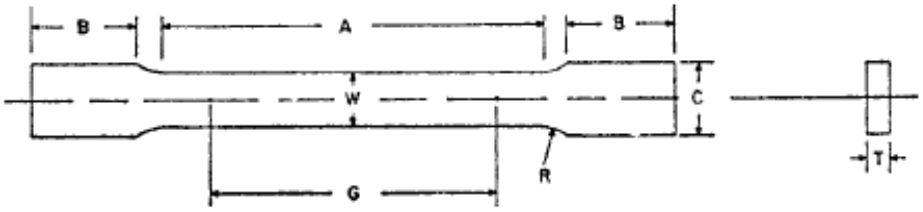

Figure 2-5 Dog bone tension test specimen [94].

Table 2-1 Dimensions for dog bone specimen.

Specimen Dimensions	mm
G, Gage length	-
W, Width	0.5
T, Thickness*	0.5
R, Radius of fillet, min	4
A, Length of the reduced section, min	12
B, Length of the grip section, min	8
C, Width of grip section, approximate	8

*All other data are scaled based on thickness

Due to the symmetry, only a quarter of the dog bone is simulated. A front view of the model with boundary and loading conditions is plotted in Figure 2-6. The specimen is fixed on the top and symmetry condition is applied on the right side.

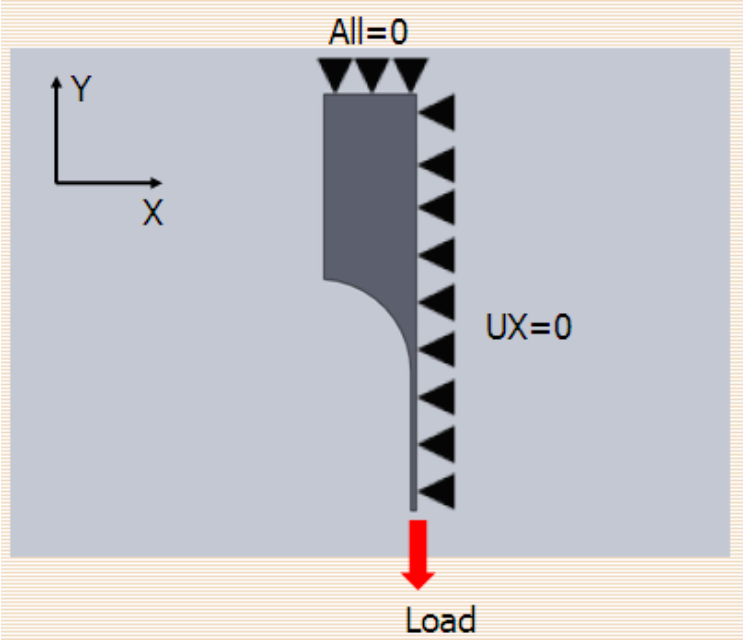

Figure 2-6 Boundary and loading conditions for tension simulation.

Due to material non-linearity, large deformation and the 3D model, 20-node Solid 186 elements are chosen and are used through all the models later in this thesis. Material properties of NiTiNOL are imported from [67] and shown in Table 2-2. A quasi-static analysis is performed with a cyclic loading to obtain the hysteresis behavior of the material. The cyclic load was calculated to be from 0 N to 110 N so that the maximum stress within the specimen can fall in the superelastic region. The hysteresis loop of stress-strain from my simulation is shown in Figure 2-7. The data reported from literature is shown in Figure 2-8. The enclosed area of the hysteresis loop is calculated in order to make a comparison. The area from Figure 2-7 is 10.87 $mJ \cdot mm^{-3}$ while the area from Figure 2-8 (simulation) is 10.75 $mJ \cdot mm^{-3}$. It demonstrates good agreement between my simulation and the simulation from literature. Since the two dog bone specimens have slight difference in dimensions, the two simulation results are not exactly the same.

Table 2-2 NiTiNOL material properties for the dog bone specimen [67].

$E\ (GPa)$	μ	$\sigma_s^{AS}\ (MPa)$	$\sigma_f^{AS}\ (MPa)$	$\sigma_s^{SA}\ (MPa)$	$\sigma_f^{SA}\ (MPa)$	$\bar{\varepsilon}_L$	α
27.5	0.3	339	440.95	185.5	112.6	0.048	0

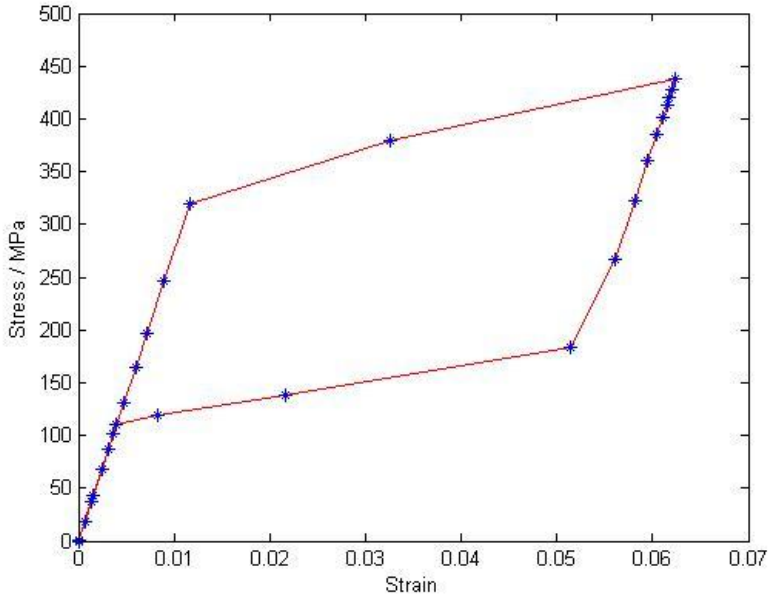

Figure 2-7 Stress-strain hysteresis plot for tension simulation.

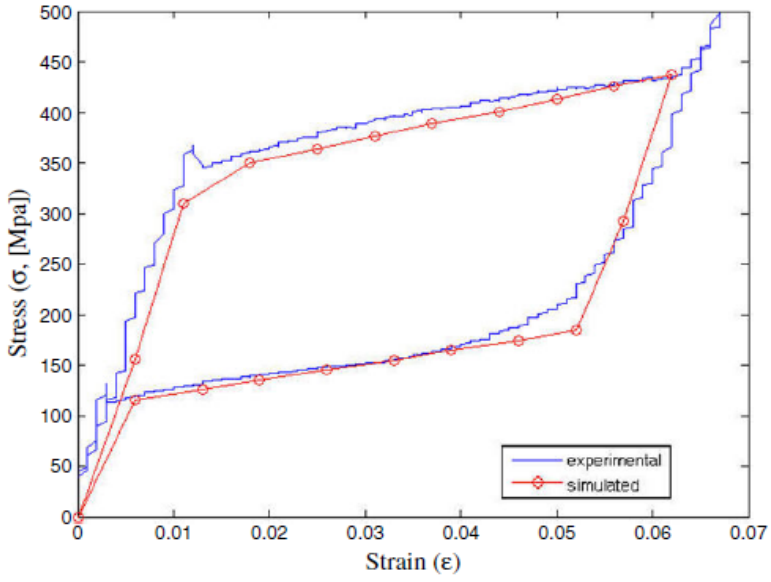

Figure 2-8 Experiment and simulation hysteresis loops are compared to prove the high accuracy of the model [67].

A bending analysis is performed here to further understand the modeling of superelastic effect in ANSYS. A cantilever beam is modeled in ANSYS with a 1 mm by 1 mm square cross-section and 10 mm span. Boundary and loading conditions are shown in Figure 2-9.

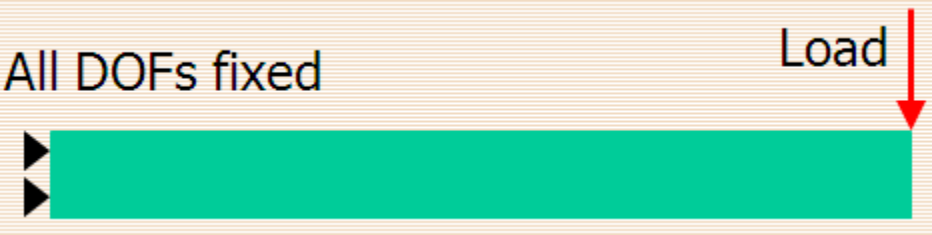

Figure 2-9 Boundary and loading conditions of bending simulation.

The beam model is in 3D where a uniform mesh is applied. Material properties (Table 2-3) are adopted from literature [95]. Similar to tension simulation, a cyclic loading is applied in quasi-static condition to get the hysteresis plot of stress and strain (Figure 2-10). The cyclic loading is calculated to be from 0 N to 1.8 N so that the maximum stress could fall in the superelastic region. Four curves represent different mesh on the beam. The variable 'NX' represents the number of elements along the span since it is a uniform meshing, while meshing in the other two directions are the same for all four simulations. For example, when NX is 24, it means that there are 24 evenly distributed elements along the span. The more elements along the span, the more accurate the result will be. The corresponding simulation result (Figure 2-11) is taken from literature. The two simulation results are almost identical. Differences may be caused by the loading condition which is not specified in the literature whether it is a point loading or line loading. Experimental results are not reported for this problem.

Table 2-3 NiTiNOL material properties for the cantilever beam [95].

$E\ (GPa)$	μ	$\sigma_s^{AS}\ (MPa)$	$\sigma_f^{AS}\ (MPa)$	$\sigma_s^{SA}\ (MPa)$	$\sigma_f^{SA}\ (MPa)$	$\bar{\varepsilon}_L$	α
71.1	0.3	500	700	400	200	0.044	0

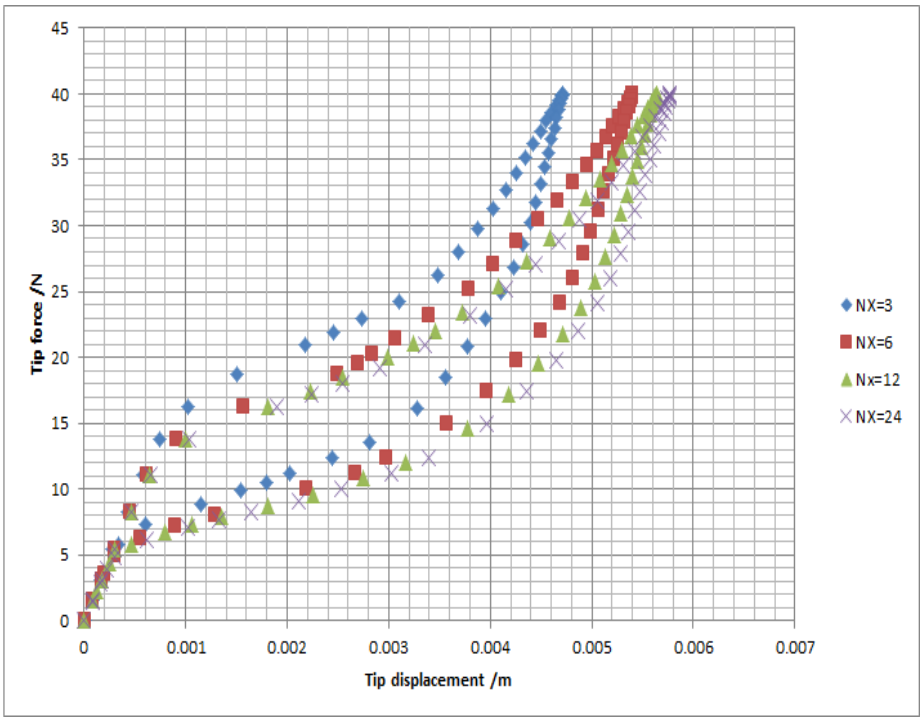

Figure 2-10 Tip force vs. tip displacement results with different number of elements.

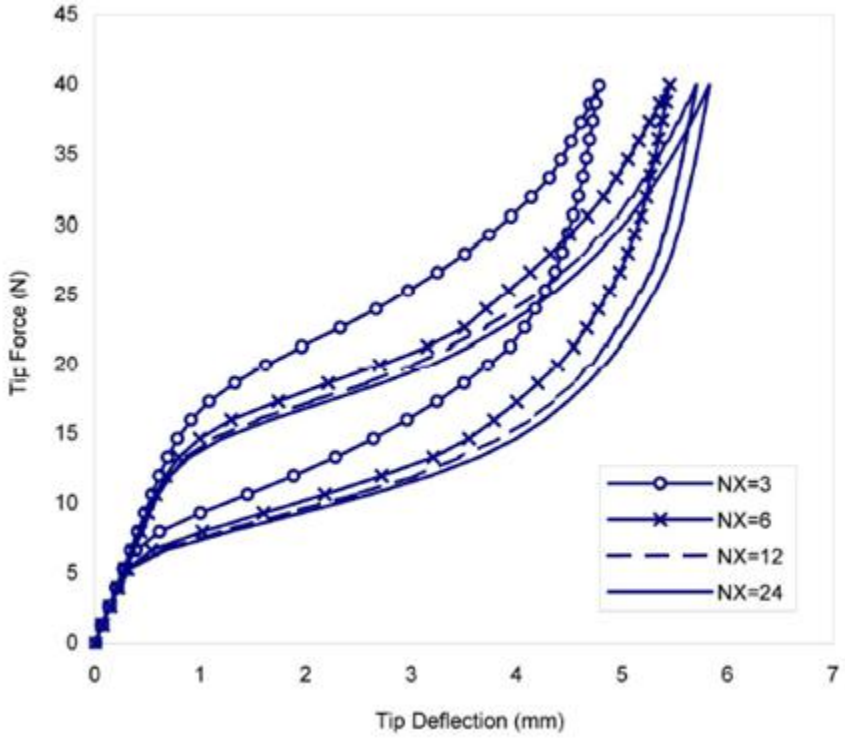

Figure 2-11 Tip force vs. tip deflection from literature [95].

Finally, an orthodontic wire is modeled in ANSYS to evaluate the understanding of complex geometry and deformation modeling using superelastic NiTiNOL. The orthodontic wire case is chosen from [96]. The corresponding NiTiNOL material properties are shown in Table 2-4. The 3D wire is fixed at the upper left end while a displacement load (7 mm) is applied horizontally at the lower right end to pull the wire to the right. Figure 2-12 shows my simulation result with maximum von Miese stress of 756 MPa, while Figure 2-13 is the corresponding simulation result from the literature with maximum von Mises Stress of 765 MPa. The difference can be calculated as 1.18%. And we can also see good agreement on the stress plots of these two simulations. The difference may be caused by different element types and meshing density which both are not presented in the literature.

Table 2-4 NiTiNOL material properties for orthodontic wire [96].

$E\ (GPa)$	μ	$\sigma_s^{AS}\ (MPa)$	$\sigma_f^{AS}\ (MPa)$	$\sigma_s^{SA}\ (MPa)$	$\sigma_f^{SA}\ (MPa)$	$\bar{\varepsilon}_L$	α
50	0.3	500	500	300	300	0.07	0.136

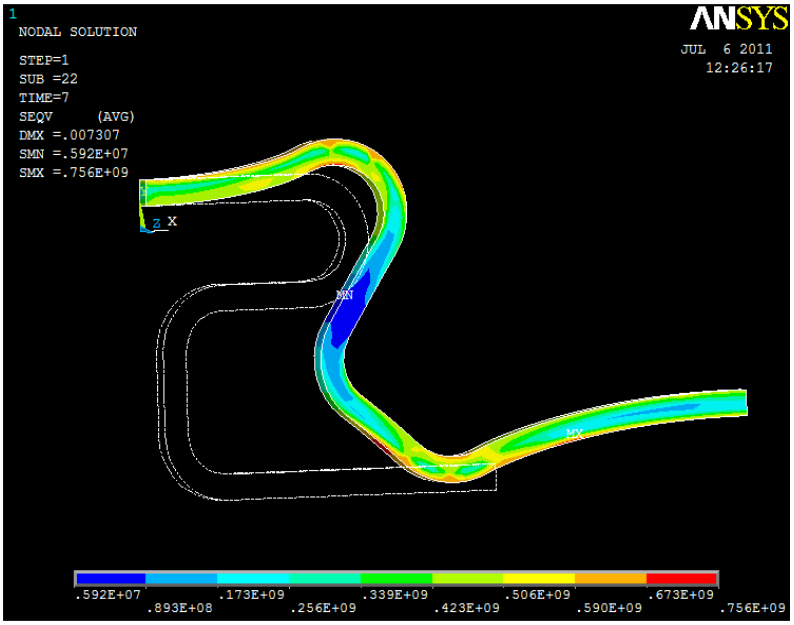

Figure 2-12 Von Mises stress plot of orthodontic wire simulation.

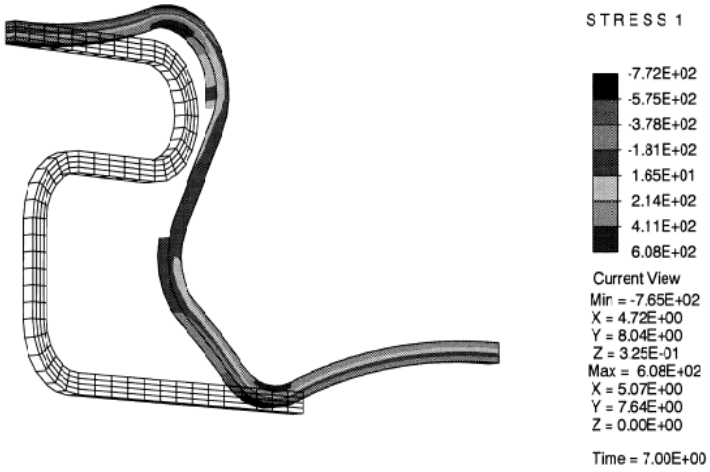

Fig. 7. Orthodontic archwire: deformed mesh in the maximum deformed configuration.

Figure 2-13 Stress plot of orthodontic wire simulation from literature [96].

Thus, based on all three simulations and their good agreement with data reported in the literature, we are confident in modeling more complex and customized geometries using superelastic model in ANSYS.

2.2.3 Meshing Method

More studies are conducted to find a suitable meshing approach and element size so that simulation can be done in acceptable time duration and the result converges.

A simple cantilever beam with 1 mm by 1 mm square cross-section and 10 mm span is considered a basic model to explore a proper meshing method that satisfy convergence and save computational time. The boundary and loading conditions are the same as the one shown in Figure 2-9.

The superelastic material model in previous bending simulations and orthodontic wire case was observed non-convergence at the first phase transient point during loading at regions that has severe stress changing or large curvature. Figure 2-14(a) shows a non-convergent stress-strain plot from one of bending simulations in previous section, where red circle highlights the non-convergent region, while Figure 2-14(b) gives a convergent stress-strain plot for the same analysis.

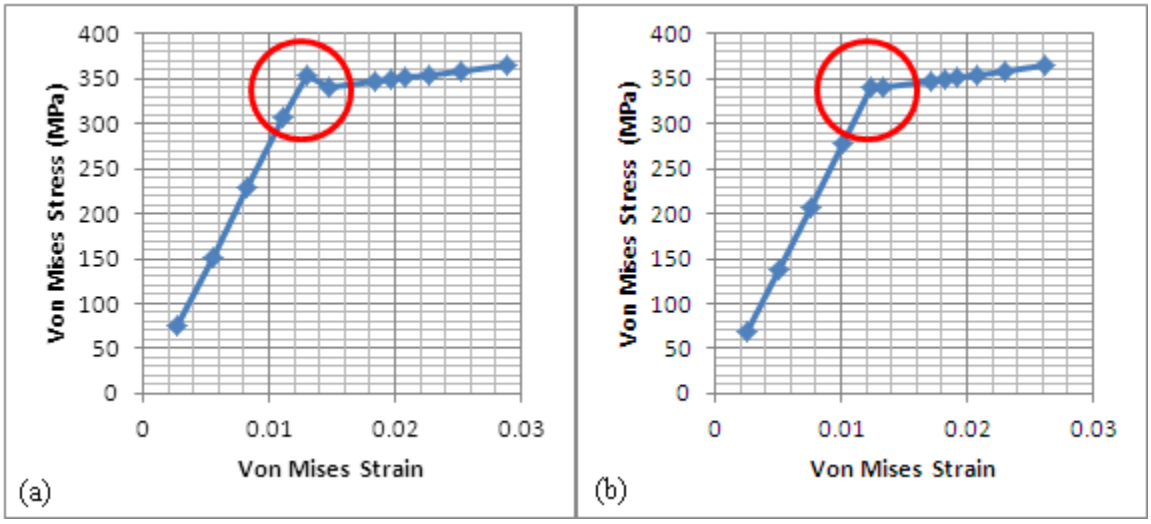

Figure 2-14 (a) Stress-strain curve of a bending cantilever beam with non-convergent response; (b) Stress-strain curve of a bending cantilever beam with convergent response.

There are typically several reasons that may lead to non-convergence in non-linear analysis, such as insufficient number of elements and large time step. Usually, either decreasing the time step, or increasing the number of elements will help convergence. Thus, two variables, time steps and element number, are investigated. First, the beam is meshed by 8-2-24 (Figure 2-15) which means there are 8 elements across the thickness, 2 elements across the width and 24 elements across the span.

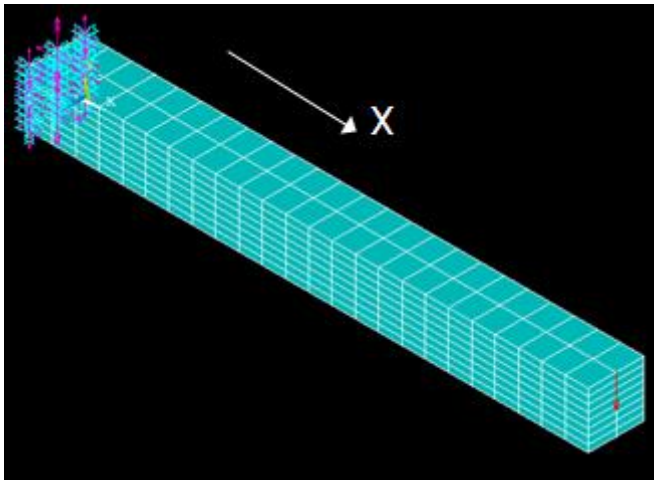

Figure 2-15 A cantilever beam is uniformly meshed in ANSYS.

Different time steps, $t = 0.05, 0.01, 0.005$, are chosen to evaluate the convergence. One important thing to notice is that the computation time of non-linear analysis especially in 3D is very sensitive to time step and number of total elements in the model. Thus we didn't choose time step that is smaller than 0.005, which might take about 20 mins to solve a simple beam problem. The simulation result is shown in Figure 2-16, where NX represents the number of elements across the span. All the simulation models here are the same except the time step. It can be observed that when the time step becomes smaller the non-convergence region doesn't disappear. We could further decrease the time step. However, this creases the computation time.

On the other hand, we can increase the number of elements to see if it could help with convergence. In order to compare with the time-step variation, we preserve all the model properties from the previous simulation. The only change right now will be the number of elements across the span. We choose time step to be 0.05 and number of elements across the span to be 12, 24 and 48. Figure 2-17 shows the result of element density study. When the number of element across the span increases to 48, the non-convergence region disappears. What's more, the last plot (right lower corner) in Figure 2-17 demonstrates the non-convergence is more sensitive to number of elements than the time step. Thus, by increasing the number of elements in regions of high stress we could overcome this non-convergence issue. Also, detail meshing and number of elements to prevent the non-convergence region is model dependent. It needs to be evaluated before simulating any superelastic model in ANSYS.

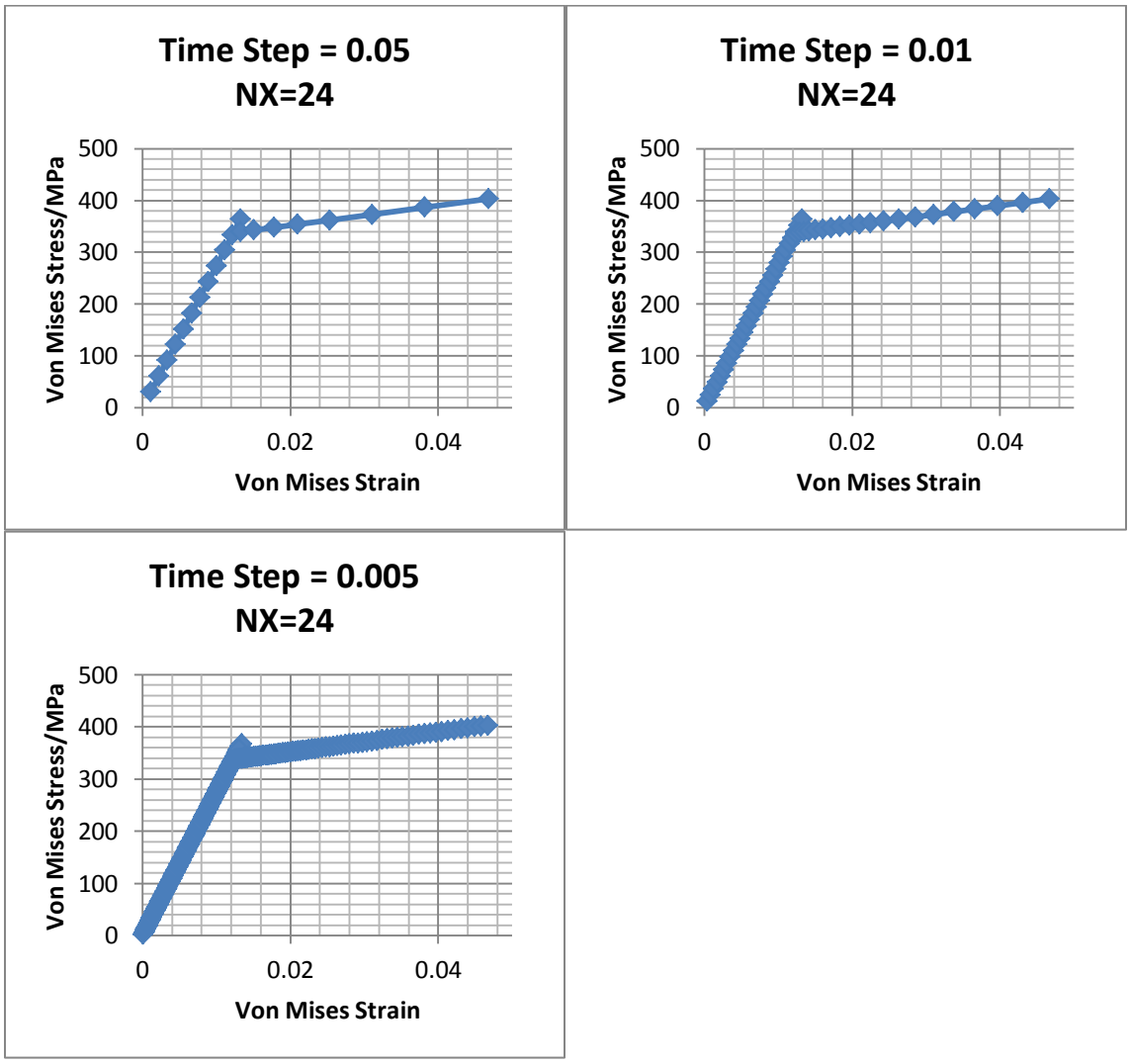

Figure 2-16 Investigate the influence of time step on convergence.

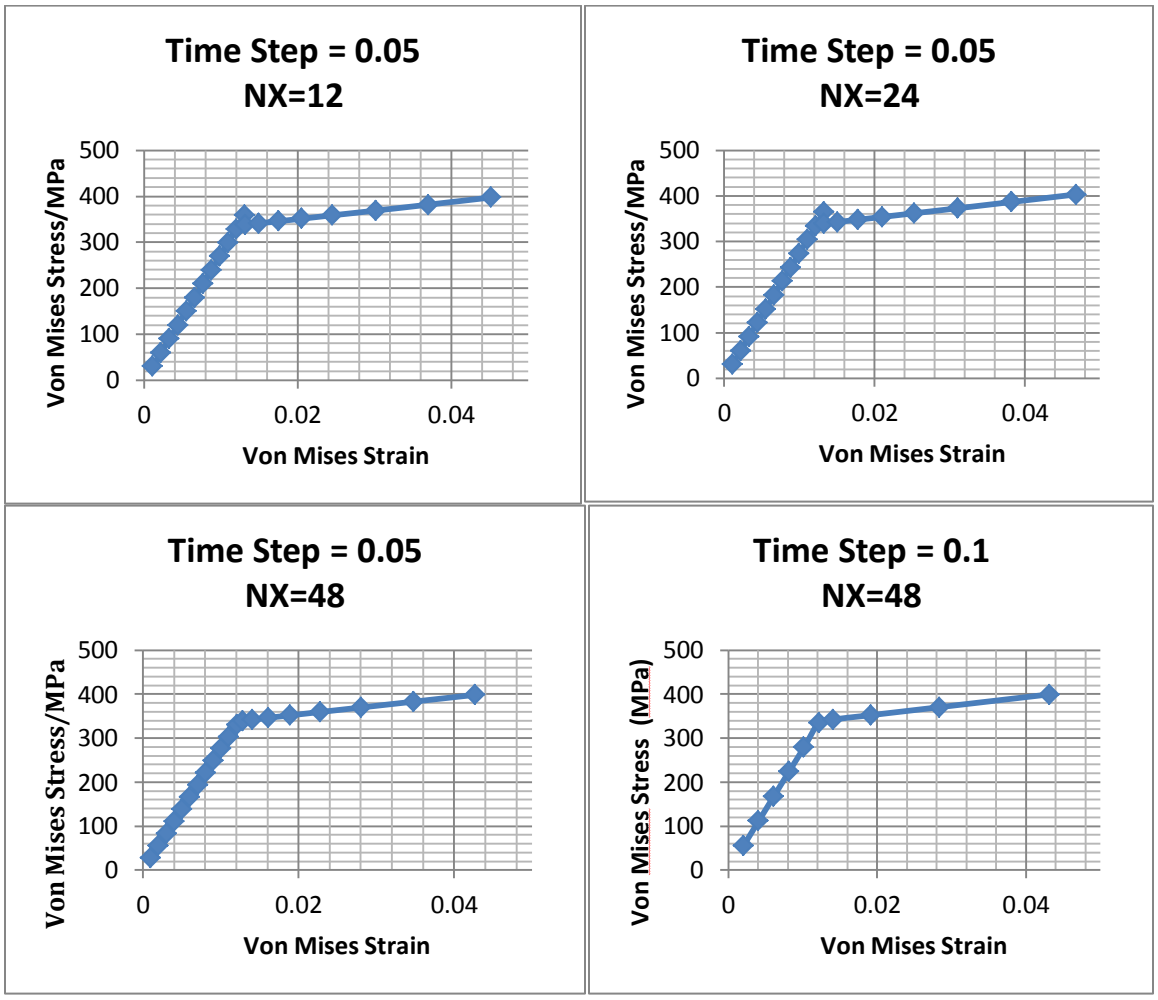

Figure 2-17 Investigate the influence of element density on convergence.

2.2.4 Articulation Structure Modeling

The design we proposed in Figure 2-2 will be analyzed to evaluate its performance. Since the model is 3D, and because material nonlinearity will increase the computational time dramatically, symmetry conditions are applied. Thus only half of the actual structure is simulated. The compliant articulation structure must articulate or deform to a very large angle, as large as 90 º. At the same time, the structure must be able to withstand sufficient force so that it is stiff enough for the surgical tool tip to manipulate tissue effectively. These conflicting design requirements are modeled using two performance metrics, free articulation angle and blocked force. The definition of the deflection, or articulation angle, is shown in Figure 2-18. X_1 and Z_1

are the coordinates of higher end while X_2 and Z_2 are the coordinates of lower end. The articulation angle can be calculated as in Equation (2-2). Free articulation angle is calculated under the assumption of no external force or resistance, and thus represents the maximum articulation angle that can be achieved. In the finite element analysis, the articulation angle is defined as the maximum angle that can be achieved without exceeding the material stress limit.

$$\phi = arctan\left(\frac{Z_1 - Z_2}{X_1 - X_2}\right) \qquad (2\text{-}2)$$

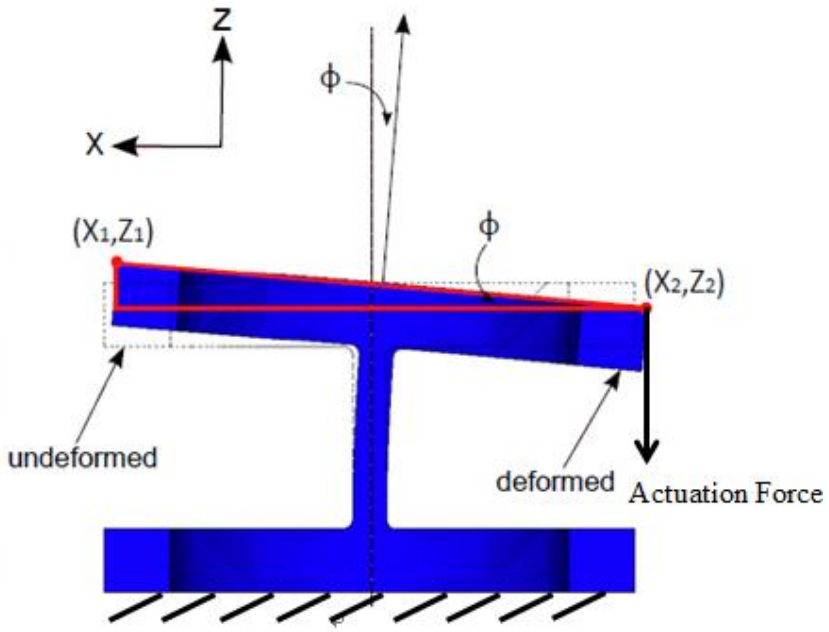

Figure 2-18 In the half symmetry model, articulation angle (ϕ) is calculated based on the displacement of two key points in the model.

The blocked force is used as a measure of the ability of the compliant articulation structure to withstand or induce external force. The actual forces encountered by the articulation structure will depend on how it is used. For example, if the attached surgical tool tip is used to manipulate tissue, the force against will depend on the stiffness of the tissue. Also, the force will depend on the length of tool tip. A longer tool tip will have larger moment on the articulation structure under the same external force. A 0.3-mm layer is added on top of the articulation structure as bonding layer for articulation structure and tool tip, where also the boundary condition for blocked force simulation is applied. Blocked force is chosen as a conservative measure for design; the actual force encountered will always be less than this value. The blocked force is modeled as shown in Figure 2-19, where the X-direction displacement of the top surface

of the ring is fixed. The articulation structure is actuated by applying a force in the negative Z direction at the edge of the structure until the maximum stress reaches a pre-set limit. Then the total reaction force at the constrained side (red in Figure 2-19) is defined as one half of total blocked force, since only half symmetry model is analyzed in ANSYS.

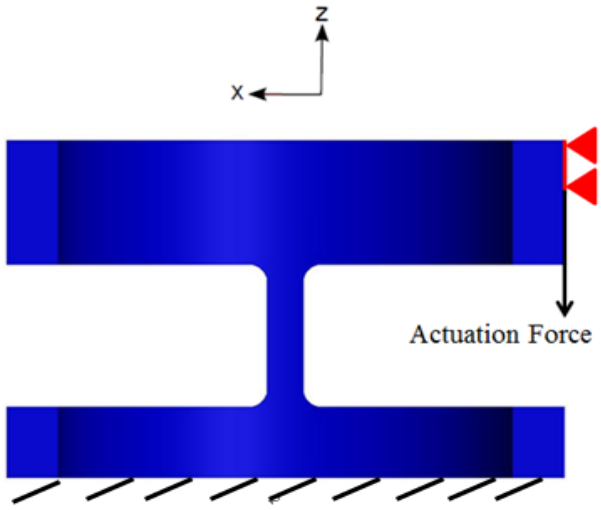

Figure 2-19 In the half symmetry model, half blocked force is defined as the reaction force at the nodes shown in red.

A convergence study is conducted in the free articulation case to find a suitable meshing approach. A medium articulation structure is picked with dimensions shown in Table 2-5. Uniform hexahedron meshing is applied on the structure (Figure 2-20).

Table 2-5 Dimensions of an articulation structure in convergence study, unit: mm

	Outside Diameter (d)	Length (L)	Width (w)	Radius (r)	Thickness (t)	Link Thickness (a)
Dimension	3.0	1.6	0.075	0.03	0.28	0.28

The boundary and loading conditions are identical to Figure 2-18 since it is the free articulation case. During articulation, peak stresses will be within the middle member and regions that have large curvatures, like fillets. Figure 2-21 presents a stress plot of the articulation structure used for the convergence study. The maximum stress is located at bottom fillets. Thus, we need to refine mesh or increase number of elements within fillets to see how the result will change and also avoid the non-convergence issue mentioned in previous section.

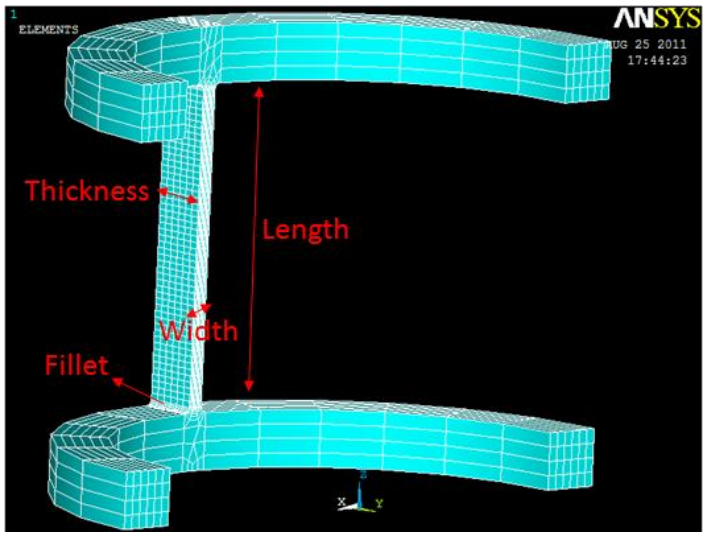

Figure 2-20 Uniform hexahedron meshing on the structure.

Figure 2-21 Von Mises stress plot of an articulation struture under free articulation.

Since we are using uniform hexahedron meshing for the structure, it is easy to see that two meshing parameters will affect the number of elements within fillets. They are number of elements across thickness and number elements along fillets, which are two orthogonal directions of meshing. For convenience, I will simply name the number of elements across thickness to be thickness and number of elements along fillets to be fillet in this section. In order to make a comparison, series of thickness and fillet combinations are evaluated where thickness is changing from 3 to 16 and fillet is changing from 4 to 16. Before the convergence study, the overshooting

issue is first investigated. While fillet is increased from 4 to 16, the maximum von Mises stress is recorded and plotted in Figure 2-22. It can be seen that when fillet is larger than 12, overshooting disappears. Therefore, for further simulation the number of elements along fillets needs to be at least 12.

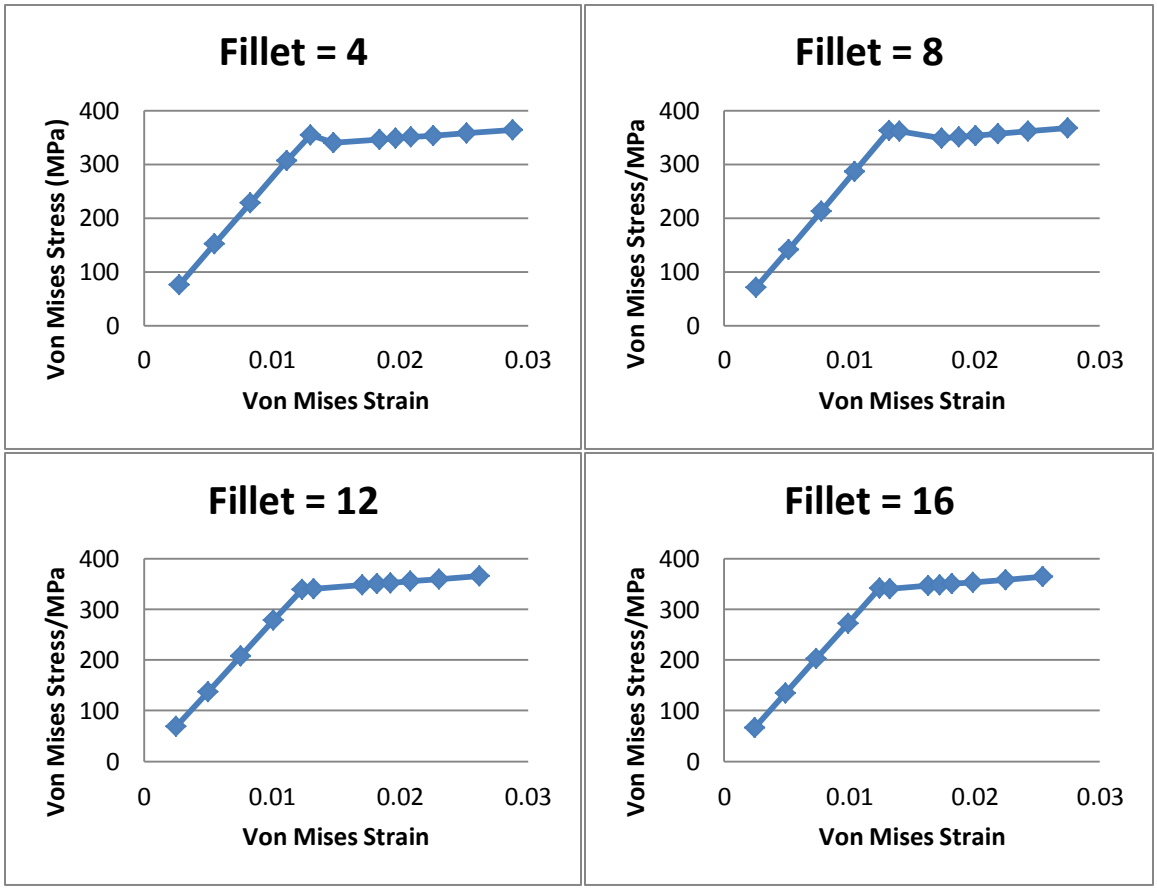

Figure 2-22 Stress-strain plot when the number of elements along fillet is changing.

Now we start refining the mesh within the fillet to complete convergence study. A thickness variation study is performed as shown in Figure 2-23. The four data points on each plot represent different number of elements along fillets (fillet = 4, 6, 12, 16 from left to right in each plot). In all four plots the stress converges at the third point where fillet equals to 12. So we can use any number of elements along fillet that is greater than or equal to 12. Considering the previous overshooting study result and the computation time increasing with the number of elements, we set 12 elements along fillet as our final meshing. By setting that, we can extract the stress value in four plots (Figure 2-23) where fillet equals to 12 and re-plot it in Figure 2-24 to determine the sensitivity of the result to thickness. In Figure 2-24, the four points represent four

different thickness (= 3, 6, 10, 16, from left to right). The stress result converges when thickness equals 6. Similarly, we choose thickness to be 6 in order to reduce computation time.

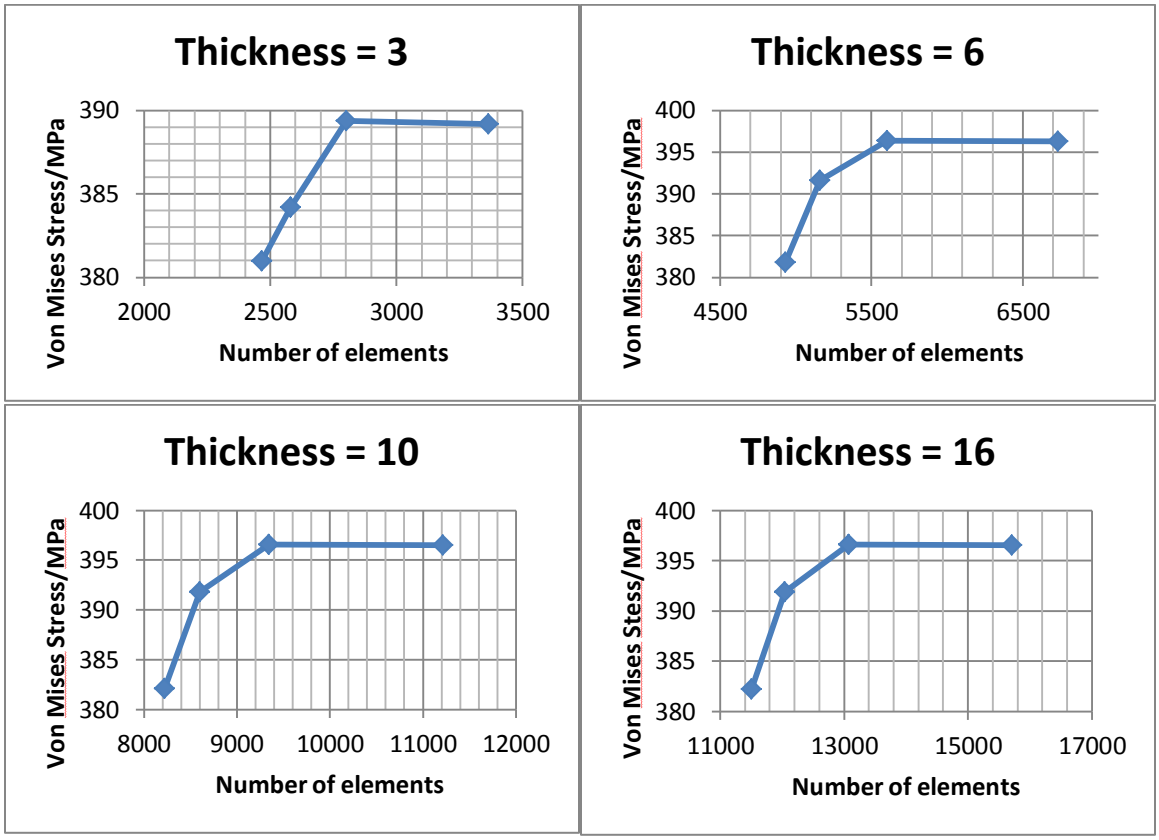

Figure 2-23 Maximum von Mises stress plotted against number of elements when both thickness and fillet are changing.

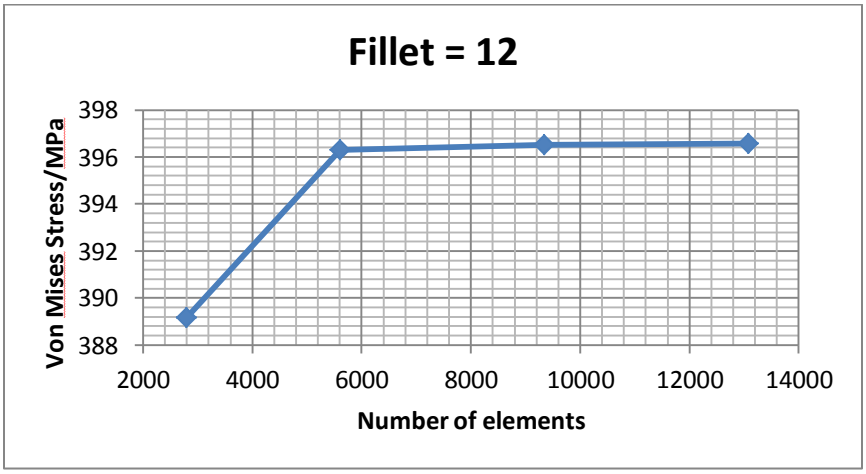

Figure 2-24 Maximum von Mises stress plotted against number of elements when fillet equals 12 and thickness changes from 3 to 16.

The best mesh within the structure depends on the particular geometry. So far, we can decide the meshing approach for the articulation structure. Uniform hexahedron meshing is utilized with 48 elements across the length, 10 elements across the width, 6 elements across thickness and 12 elements along fillets (refer to Figure 2-20).

2.3 Design Guide and Simulation Domain

The articulation structure is defined by six design parameters. In order to further understand the performance of the articulation structure, more simulations are performed to determine the impact of each parameter on free deflection angle and blocked force. These results are then used to form a design guide. A family of designs are selected according to the design guide and evaluated in ANSYS.

2.3.1 Design Guide

Geometric constraints are first taken into consideration. The outside diameter of the compliant articulation structure must be smaller than the inner diameter (ID) of the working channel of the endoscope, which yields $d < \text{ID}$.

Then, we consider constraints on the length of the compliant articulation structure. In the use the of articulation structure, a deflection angle of more than 90^o would cause the tool tip to contact the tip of the endoscope. An articulation structure is allowed to bend up to 90^o in the simulation; the deformed shape is shown in Figure 2-25(right). Since a longer length makes the structure more flexible, which results in an articulation angle of more than 90^o, an upper limit of the length needs to be set. The length in its deformed shape is regarded to be the maximum length. The middle compliant member is approximated as one-fourth of an ellipse with a major axis of $d/2$ and minor axis of $d/2 - t$, shown in Figure 2-25(left). Thus the upper boundary of the length can be derived as $\pi d/4 + (1 - \pi/2)t$. The lower limit is constrained by the radius of the fillets, since we expect fillets to reduce stress concentration. Thus, we should have $L \geq 2r$.

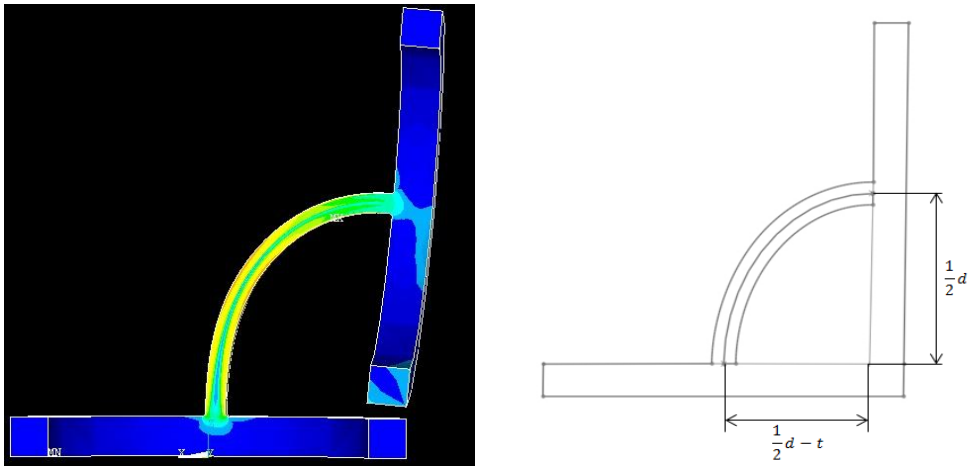

Figure 2-25 Left: illustration of an articulation structure bending up to 90°; Right: an ellipse model is fitted to calculate the maximum length.

The width of the compliant articulation structure is constrained primarily by the fabrication process. Since the articulation structure will be cut from a NiTiNOL tube using laser processing, the resolution (re) capability of laser machining will be the lower boundary of width, i.e. $w > re$. The minimum width of material that can be removed depends on the radius of the laser beam (d^*), which means $d - d^*$ will be the upper bound for the width of a given cut.

A fillet radius study is then carried out to explore how different radii will affect the blocked force and articulation angle. Three groups ($L = 0.8$, 1.2, 1.6, unit: mm) of designs are analyzed in ANSYS. Designs in each group have the same length, but the radius is varied. The remaining parameters, OD, w, t and a, are all the same among groups. Blocked force and deflection angle are plotted in Figure 2-26. Six radius values (0.01, 0.03, 0.06, 0.1, 0.2, $L/2$, unit: mm) are simulated in an individual group. Three groups are plotted with different colors. In Figure 2-26, each point represents a feasible design which satisfies the stress limit (σ_f^{AS}). Designs that are located toward the upper right region on the plot are desired since they have the largest possible blocked force and deflection angle. Thus we want to avoid designs that fall in the lower left region in Figure 2-26. The results show that with the same length, blocked force will always increase with increment of radius while deflection angle will increase first and then decrease after radius is greater than 0.06 mm. Since most stress concentration happens at the fillets, larger radius will help release the stress concentration thus improve the blocked force and deflection angle. However, larger fillet radius increases the stiffness of the structure against bending which results in smaller deflection angle. Consequently, a lower limit on radius (0.06 mm) is selected such that

designs with blocked force and deflection angle at lower left region are avoided. The upper boundary of the radius is apparently constrained by length of the structure, i.e. $r \leq L/2$.

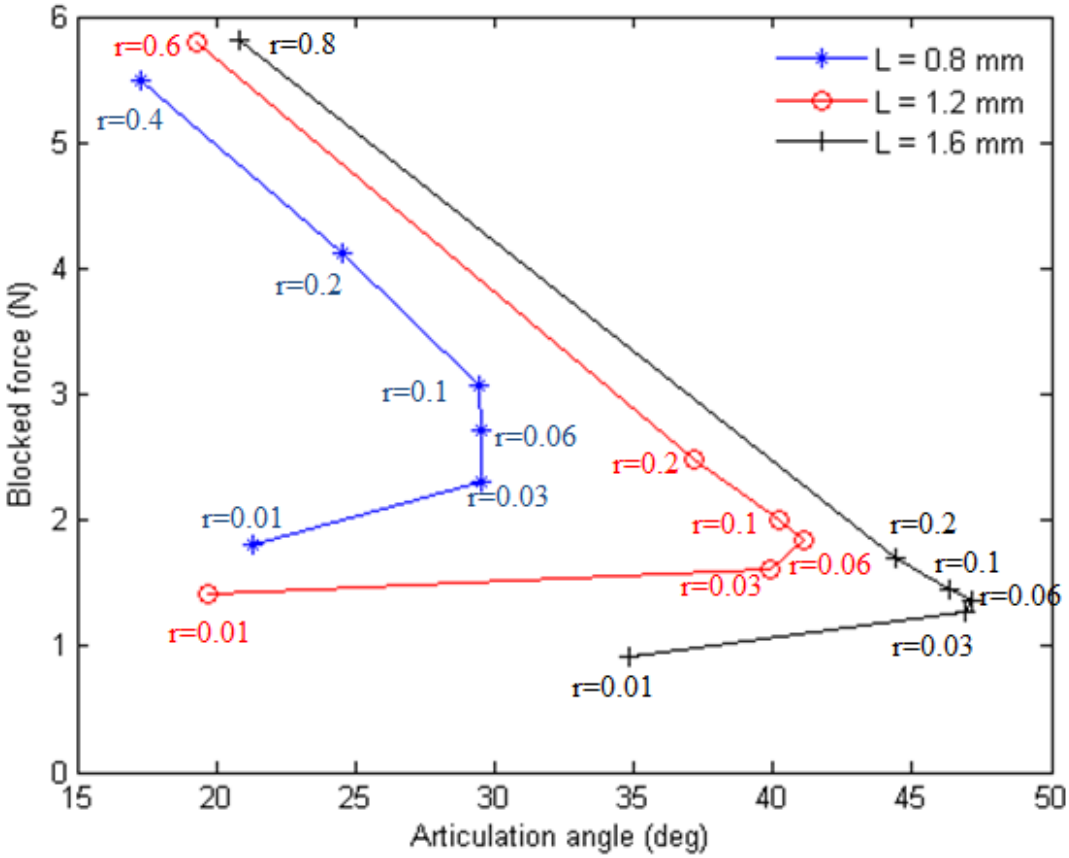

Figure 2-26 Blocked force and deflection angle for designs with three different lengths (represented by three different colors) and varying radius.

Furthermore, the ring thickness is limited to avoid stress concentration on rings. Similar to the radius analysis, a series of designs with the same outside diameter (d = 3 mm), length (L = 2 mm), fillet radius (r = 0.06 mm), thickness (t = 0.285 mm) and width (w =0.3 mm), but different ring thicknesses are analyzed in ANSYS. The ring thickness is varied from 0.3 mm to 0.6 mm. The von Mises stress contour plots are shown in Figure 2-27. Results show that the stress concentration at the top ring will decrease with increases in ring thickness. Additionally, considering the total size of the design, the smallest ring thickness (0.6 mm) that minimizes stress concentration in rings is selected. This result is then generalized for different widths, and we conclude the relationship between ring thickness and width to be $a = 2w$.

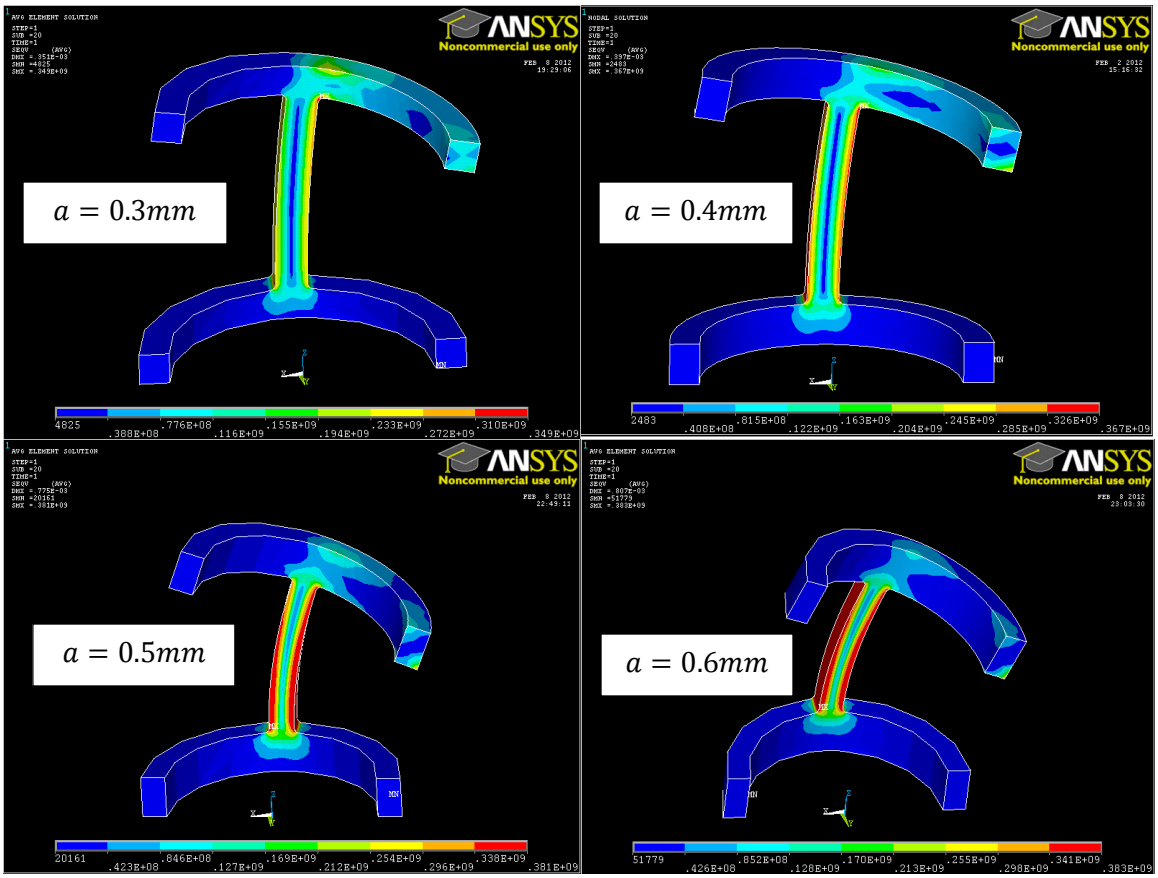

Figure 2-27 Von Mises stress plot of articulation structures with different ring thickness.

Since the laser processing will use a NiTiNOL tube as raw material, the thickness is then limited by the wall thickness of the tubes that are available in the market (t_b).

Finally, these results are summarized as design guidelines for the compliant articulation structure in Table 2-6. The same or similar guidelines can be used for design of the structure for other applications.

Table 2-6 Design guide for similar designs in other possible applications.

Geometric Parameter	Constraints
Outside diameter, d	$d < ID$
Length, L	$2r \leq L \leq \pi d/4 + (1 - \pi/2)t$
Width, w	$re \leq w \leq d - d^*$, where d^* is the diameter of the laser beam, which is about 0.03 mm.
Radius, r	$0.06\ mm \leq r \leq L/2$
Ring thickness, a	$2w$
Thickness, t	t_b, tube thickness

2.3.2 Buckling Analysis

In order for an articulation structure to provide enough deflection, the width of the structure will be much smaller than the length, and buckling could happen in the middle member. A buckling analysis is performed to predict when buckling will happen and the constraints that need to be applied to avoid that.

NiTiNOL has very unique buckling property. According to the literature, the critical load a for NiTiNOL column to buckle depends on slenderness ratio (l/k), shown in Figure 2-28 [97]. In the figure, SMA represents superelastic NiTiNOL (Ti49.3 at.%, Ni50.2 at.%, V0.5 at.%). When the slenderness ratio is smaller than 28, buckling will not happen in NiTiNOL regardless of the compressive load. When the slenderness ratio becomes larger, we can see buckling in NiTiNOL. Also, the critical compressive load for NiTiNOL to buckle is decreasing when the slenderness ratio increases. For the middle member in the compliant articulation structure, we can calculate the slenderness ratio as following. The area of the middle member can be calculated from equation 2-3. Least moment of inertia of the cross-sectional area of middle member is shown in equation 2-4. Then the least radius of gyration of the cross-section area can be derived and shown in equation 2-5. Finally, the equation for slenderness ratio is derived (equation 2-6).

$$A = wt \qquad (2\text{-}3)$$

$$I = min\left(\frac{tw^3}{12}, \frac{wt^3}{12}\right) \qquad (2\text{-}4)$$

$$k = \sqrt{\frac{I}{A}} = min\left(\frac{w}{\sqrt{12}}, \frac{t}{\sqrt{12}}\right) \qquad (2\text{-}5)$$

$$\frac{L}{k} = max\left(\frac{\sqrt{12}L}{w}, \frac{\sqrt{12}L}{t}\right) \qquad (2\text{-}6)$$

According to the laser fabrication limitation, the width has to be greater than 0.1 mm ($w \geq 0.1mm$). The NiTiNOL tube that we will use has an outside diameter of 3.07 mm (L) and a thickness of 0.285 mm (t). Thus, we find the slenderness ratio to be as following (equation 2-7).

$$\frac{L}{k} \leq 104 \qquad (2\text{-}7)$$

According to Figure 2-28, when slenderness equals 108, the critical buckling load for NiTiNOL is 550N. For slenderness that is smaller than 108, the critical load will be even higher. In the real surgery, it is very unlikely to have 550N load within human body. Therefore, the buckling is not likely to happen in the NiTiNOL compliant articulation structure.

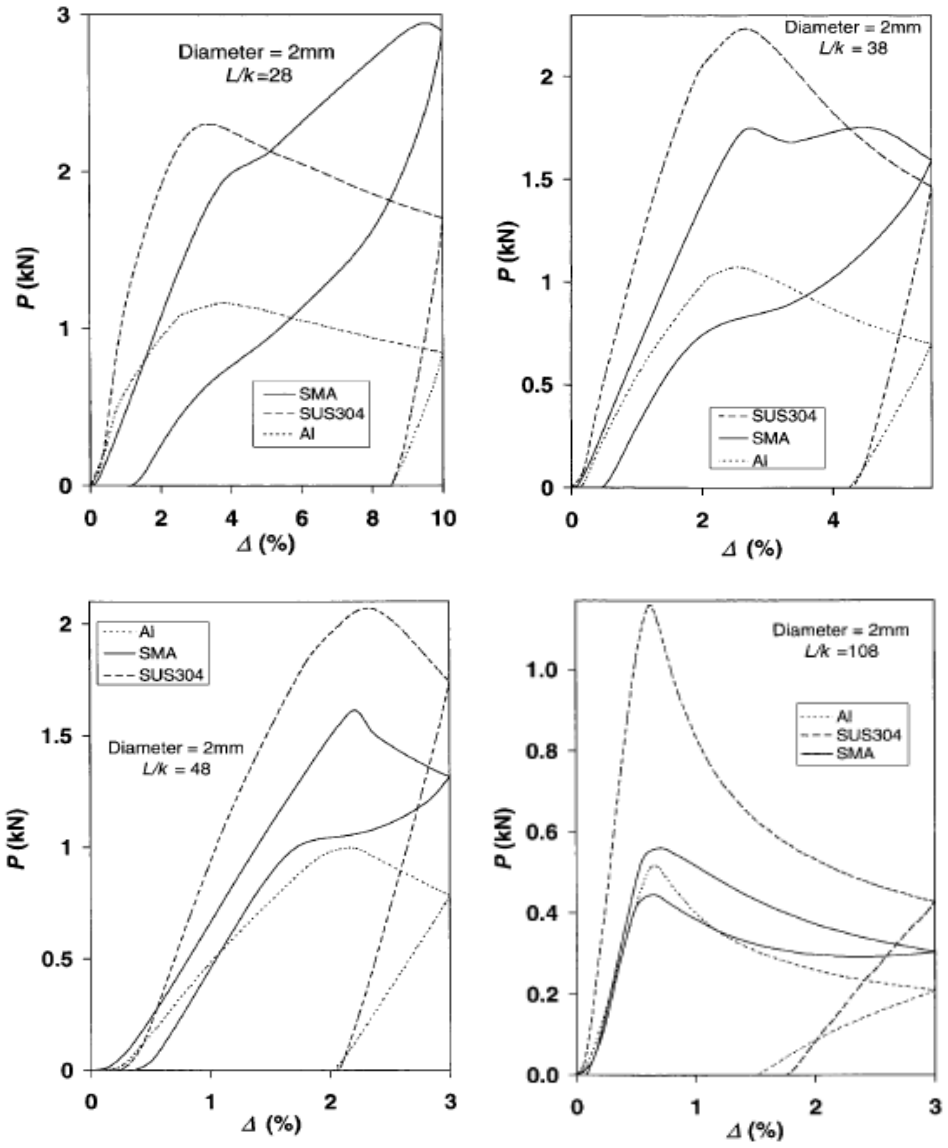

Figure 2-28 Experiment load-strain curve for different materials with different slenderness ratios [97].

2.4 Parametric variation analysis

In order to have a better understanding of the performance of the compliant articulation structure, a parametric variation analysis is performed to evaluate a family of designs. The working channel of a common endoscope is 3.2 mm in diameter. Thus a NiTiNOL tube with outer diameter of 3.07 mm ($d = 3.07\ mm$) is selected from existing products in the market. This

3.07 mm NiTiNOL tube (Appendix B) comes with thickness of 0.285 mm ($t_b = 0.285\ mm$). For the geometry of the tube considered here, this corresponds to an upper limit of 2.2 mm on L. Since the NiTiNOL material model is very sensitive to the mesh size in FEA, different meshing approaches needs to be developed for small and large designs considering the geometry. However, a uniform meshing approach is used here in order to analyze large amount of designs. So a compromised upper bound for width (0.5 mm) was picked for simulation, similar for the lower bound of length (0.8 mm). The lower bound for width is decided based on the laser fabrication limitation and chosen to be 0.1 mm. Consequently, the design domain is set up for this family of designs in Table 2-7. The NiTiNOL material properties are inherited from Table 2-2. In addition, another material 316 stainless steel (Table 2-8) which is commonly used in medical devices is evaluated at the same time for comparison.

Table 2-7 Detailed geometric values for the family of designs.

Geometric Parameter	Evaluated Values (mm)
Outside diameter, d	3.07
Length, L	$0.8 \leq L \leq 2.2$
Width, w	$0.1 \leq w \leq 0.5$
Radius, r	$0.06 \leq r \leq \min\{0.7, L/2\}$
Thickness, t	0.285
Ring thickness, a	$2w$

Table 2-8 Material properties for 316 stainless steel.

Property	Value
Young's Modulus, E	193 GPa
Poisson's Ratio, μ	0.3
Yield Strength, σ_Y	240 MPa

A family of designs is evaluated within the design range listed in Table 2-7. 3D elements, Solid186, were used and 105 NiTiNOL designs were evaluated in ANSYS. An upper limit on the stress, which is assumed to be the same value as Austenite finish stress (σ_f^{AS}), is set as the stress constraint for all the NiTiNOL designs. The simulation results are pictured in Figure 2-29 with results using 316 stainless steel (stress limit is the yield strength) as comparison.

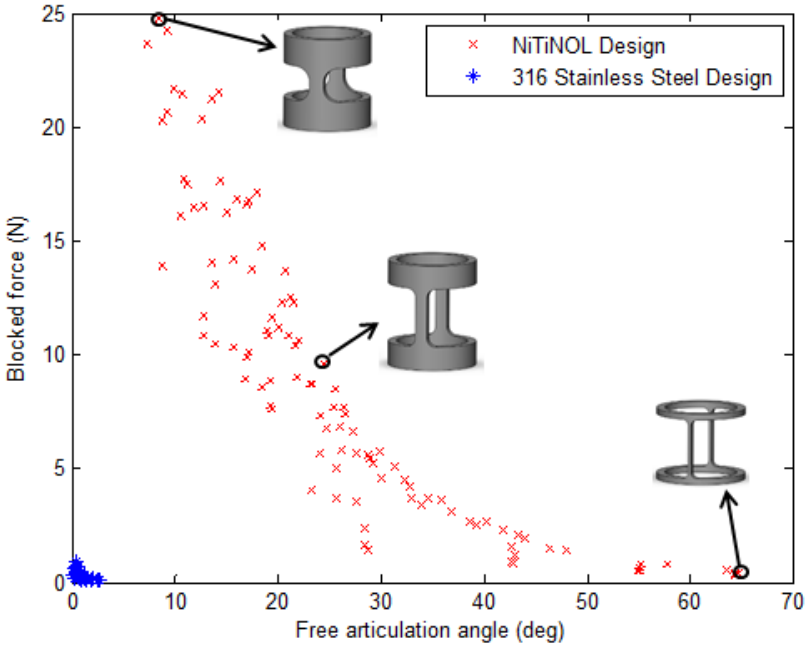

Figure 2-29 Blocked force and free articulation angle results of the family of designs, with comparison to 316 stainless steel results.

In Figure 2-29, each point represents a feasible articulation structure design within the specified design family. Each design satisfies the stress limit constraint in both free articulation angle and blocked force simulations. It can be seen that significant improvement in blocked force and free articulation angle are obtained when using NiTiNOL compared to 316 stainless steel. For NiTiNOL, a maximum blocked force of 24.7 N and a maximum free articulation angle of 64.8^{o} are predicted. However, the ideal design that has both high blocked force and free articulation angle cannot be achieved while satisfying the stress constraint. Instead, there is a tradeoff between free articulation angle and blocked force, i.e., increasing the free articulation angle will lead to a decrease in blocked force. Based on the design requirements for a particular application, the designer can choose one or more articulation structure sections to fulfill the force and articulation angle requirements. There are three sample designs on the figure as well to illustrate the relationship between the geometry of the structure and articulation angle/blocked force.

ANSYS simulation results of a sample design ($d = 3.07, a = 1, w = 0.5, L = 1.2, t = 0.285, r = 0.5, unit: mm$) with moderate angle and force (middle image on Figure 2-29) are pictured in Figures 2-30. This design is predicted to have blocked force of 9.6 N and free articulation angle of 24.4^{o}. The deformation and element von Mises stress contour are shown in the Figures. It can be seen that the maximum stress and stress concentration occur within the

middle compliant member, especially in regions close to fillets. The top and bottom rings are barely deformed which ensures that there is no negative impact on tool tip or any structures attached to it.

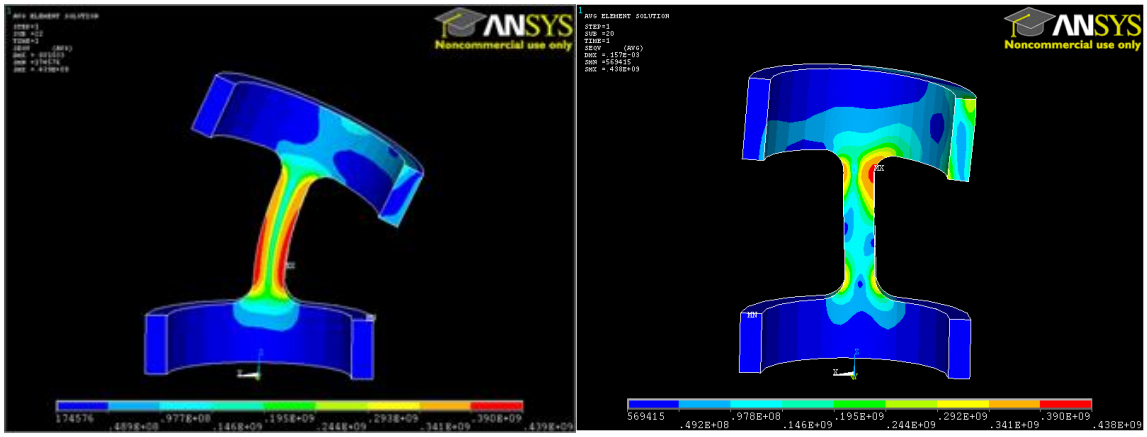

Figure 2-30 Left: von Mises stress plot of half symmetry model in Free Articulation Angle case; Right: von Mises stress plot of half symmetry model in Blocked Force case.

2.5 Summary

This chapter presented the modeling of the superelastic material in ANSYS, a design guide for the articulation structure and computational results obtained using ANSYS. It first explains the detail of superelastic modeling approach in ANSYS and validates the model by comparing to the literature. A design guide is established based on analytical analysis and computational analysis, which is then generalized for similar kinds of articulation structure. Finally, a parametric analysis is performed to evaluate a family of designs using superelastic NiTiNOL and 316 stainless steel. Results are compared and reveal that NiTiNOL can improve the performance of the articulation significantly compared to traditional 316 stainless steel. Sample designs proposed in this chapter will be fabricated and the simulation results will be utilized later to compare with experiment results.

Chapter 3

Fabrication and Experimental Validation

This chapter discusses the fabrication process and the experimental validation of the superealstic compliant articulation structure. First, the laser fabrication process will be introduced. Three sample designs are fabricated using laser processing. The fabricated structures are tested using a dynamic mechanical analyzer. Finally, the experiment results are compared with the simulation results to validate the finite element analysis and material model.

3.1 Fabrication of NiTiNOL Articulation Structure

Laser micromachining and the detailed fabrication process of articulation structure will be introduced. Two different laser systems are used to fabricate the articulation structure. Fabrication results are compared and discussed.

3.1.1 Laser Micromachining

Processing NiTiNOL can be particularly challenging due to its high hardness and the sensitivity of thermal effects and mechanical properties to processing conditions. Means of micromachining NiTiNOL include: milling, drilling, sawing, EDM, photochemical etching, and pulsed laser processing [98].

Lasers have become an increasingly popular choice due to their high processing speeds and flexibility. With pulsed laser processing there are three distinct operating regimes: gated continuous wave (CW) laser (10^{-3}~10^{-6} second pulse duration), Q-switched lasers (10^{-9} second pulse duration), and ultrafast laser (10^{-12}~10^{-15} second pulse duration). Each of these processing regimes offer a particular set of advantages.

The high average power and millisecond/microsecond pulse durations associated with gated CW lasers allow for rapid processing, but require the processed sample to be actively

cooled with liquid coolant and a high-pressure, coaxially supplied gas to reduce the heat affected zone (HAZ), control oxidation, and remove processing debris. The dominant mechanism for material removal is through heat conduction and melting. In experiments performed by Leitz et al., 80 microsecond pulses at 1064 nm wavelength with a fluence of 140 J/cm^2 on stainless steel were shown to have a significant recast of expelled molten material when compared to the other methods [99].

Q-switched lasers have pulse durations in the nanosecond range and offer a processing regime in which material is ablated, with expelled material comprising both liquid and gas phases. Due to the shorter pulse duration and correspondingly reduced duty cycle, coupled with the different mechanism of material removal, a smaller HAZ is produced. Melting still occurs, but removal rate is driven by the increasingly dominant ablation/vaporization mechanism. For example, in experiments performed on Nitinol tubing with a wall thickness of ~200 microns by Schuessler et al. using a 100 ns laser at 1064 nm wavelength and a repetition rate of 10 kHz, an ablation region was observed extending 50 microns into the cut, while below it melting was obvious [100].

Ultra-short pulsed lasers including picosecond and femtosecond lasers are of growing importance in the fabrication of NiTiNOL parts, and have proven to have excellent processing characteristics [101]. The extremely short pulse duration enhances laser energy coupling through a nonlinear multi-photon absorption mechanism and produces virtually no residual heat [99], thus preserving the microstructure as evidenced using X-ray diffraction (XRD) [102], and mechanical properties [103].

3.1.2 Laser Micromachining of Compliant Articulation Structure

Representative designs are fabricated using laser processing. This process was performed by our collaborators, Dr. Edward W. Reutzel and Benjamin Hall at the Pennsylvania State University Applied Research Lab, and is summarized here. Two lasers were used to process a 3.07 mm diameter Nitinol tube with 285 micron wall thickness (Appendix B):

1. 355 nm Coherent Q-switched ultraviolet laser (Avia 355) with a 30 nanosecond, 185 microjoule pulse at a repetition rate of 11 kHz, in conjunction with a GSI Lumonics beam-scanning galvanometer.

2. 1064 nm Miyachi Unitek 200 W single mode fiber laser system (Sigma Laser Tube Cutter) with a repetition rate of 1.5 kHz and pulse energy of 50 mJ with a 500 micron output nozzle and 55 psi coaxially driven flow of O_2 assist gas.

Machining on the Avia laser was performed with a combination rotary and linear stage at a travel speed of ~1.7 mm/s. Neither active cooling nor assist gas was used. Due to the low pulse energy, multiple passes were required to penetrate the tube wall. The optical focal length was fixed at ~250 mm, which contributed to degraded cut quality, as discussed in the results.

Processing on the Miyachi Unitek tube cutting system utilized flowing water through the tube during processing to cool the sample, remove debris, and protect the back wall from incident laser radiation. The focal length was 80 mm and the sample was cut in a single pass at a rate of 3.8 mm/s using a fixed beam and rotary stage.

Several articulation structures were fabricated from a SE508 tube from NDC (with outside diameter of 3.07 mm, inner diameter of 2.50 mm, and Austenite finish temperature of -2.33 ^{o}C, Appendex B) using two different laser systems, Coherent Avia and Miyachi Unitek. The NiTiNOL tube was held by a rotary stage connected to X and Y linear stages. The tube had its top surface at the focal plane of the laser and was rotated and translated to process the desired features with the beam held at a fixed position. Due to constraints on the articulation rate of the stages and feature size, a velocity of 1.8 mm/s was chosen. The beam was pulsed at a rate of 11 kHz, corresponding to a pulse with energy of approximately 185 microjoules. It was noted that, despite the short pulses, significant heat buildup had occurred by the visible discoloration of a developing oxide layer. Although the laser could be seen penetrating through the thickness of the outer wall after the first 10 passes, re-welding of the interface seemed to have occurred, due to the small (50~60 micron) kerf-width and local heat concentration. After 50 passes, the tube was immersed in an ultrasonic cleaner to remove processing debris. The cutout remained connected to the sample, and required application of force to remove it. Measurements indicated an edge roughness of approximately 15 microns. Total sample processing time was 11 minutes.

The results from the Miyachi Unitek system were significantly better, with a clean, smooth cut and a reduced visible HAZ. The short focal length and single mode beam profile allowed for a small spot size, helping to increase fluence and localize heat effects. The surface roughness was on the order of 5 microns, and processing time was less than 5 seconds per sample. The samples produced for this evaluation are shown in Figure 3-1.

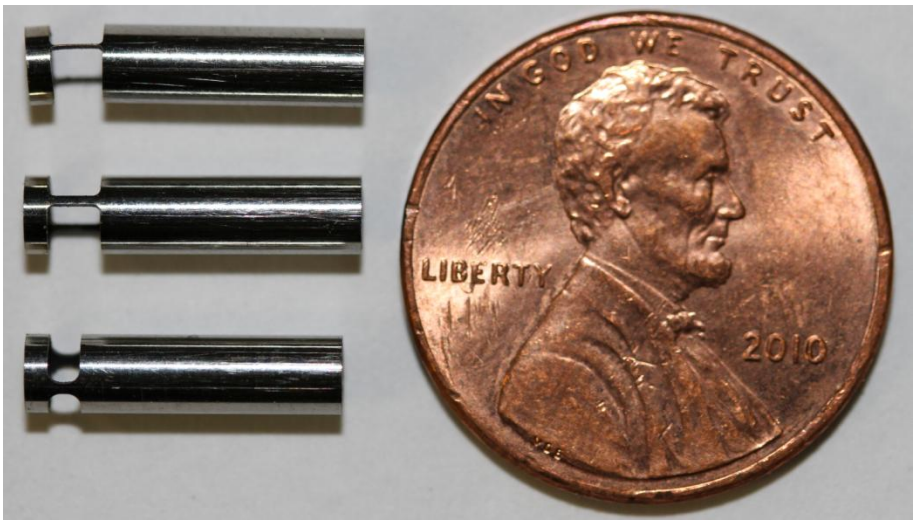

Figure 3-1 Three sample designs fabricated using laser processing.

Finally, the three designs pictured in Figure 2-29 for experiment were fabricated using the Miyachi Unitek system. These three designs (from left to right in Figure 2-29) are one with maximum blocked force, an intermediate one with moderate blocked force and articulation angle, and a third one with maximum free articulation angle. They are labeled as Ⅰ, Ⅱ and Ⅲ, respectively, in Table 3-1. The fabricated structures have extended tube length so that they can be fixed in the test setup.

Table 3-1 Geometric properties of three designs, unit: mm.

Geometric Parameter	Ⅰ	Ⅱ	Ⅲ
Outside diameter, d	3.07	3.07	3.07
Length, L	1.20	2.00	2.00
Width, w	0.50	0.40	0.10
Radius, r	0.50	0.30	0.20
Thickness, t	0.285	0.285	0.285
Ring thickness, a	1.00	0.80	0.20

3.2 Experimental Validation

Prior to the experiment, more simulations were run to evaluate the differences in the articulation structure model caused by material properties, geometry and loading conditions. Three major differences were considered: material properties, geometric differences introduced by the fabrication process, and the loading condition in the experiment. Therefore, three more

simulations were computed. Combining the initial simulation, four simulation results are then compared with experiment results.

3.2.1 Modified Finite Element Analysis

In the initial simulation described in section 2.2.4, the material properties were imported from the literature. This material is different from the actual tube material that was provided by the manufacturer. The material properties used for simulation are obtained from the stress-strain curve of NiTiNOL tube tensile test from the manufacturer (Appendix A) and listed in Table 3-2. The second major difference is the geometric dimensions between fabricated articulation structures and original designs. The error in the laser processing leads to the differences in the fabricated structures. All geometric properties of the fabricated parts (except radius, since it was not measured directly) were measured and listed in Table 3-3. The third difference is the loading condition. In the initial simulation, it is assumed that the articulation structure is actuated by two wires so that the actuation force is applied at the edge of the structure. In the experiment, the load will be applied from the top of the structure. The loading condition can be illustrated as Figure 3-2.

Table 3-2 Material properties of NDC NiTiNOL tube at 22°C.

Property	Value
E	$44.0GPa$
μ	0.3
σ_s^{AS}	$440MPa$
σ_f^{AS}	$472MPa$
σ_s^{SA}	$218MPa$
σ_f^{SA}	$206MPa$
$\bar{\varepsilon}_L$	0.045
α	0

Table 3-3 Geometric properties of fabricated parts.

Geometric Parameters	I	II	III
Outside diameter, d, mm	3.07	3.07	3.07
Length, L, mm	1.16	1.96	1.90
Width, w, mm	0.48	0.35	0.08
Radius, r, mm	0.50	0.30	0.20
Thickness, t, mm	0.285	0.285	0.285
Ring thickness, a, mm	0.90	0.92	0.96

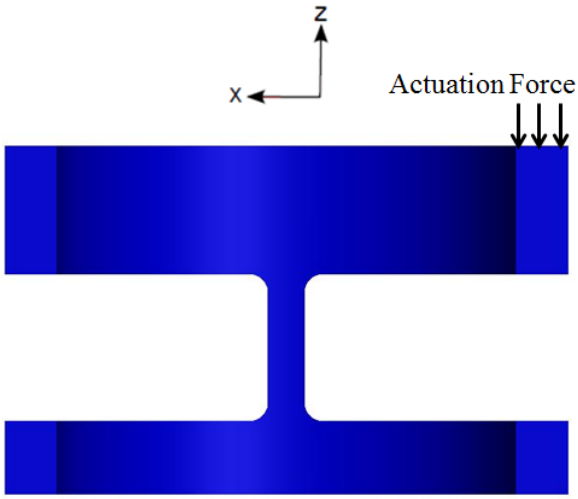

Figure 3-2 Loading condition in experiment, taken into consideration during modified FEA.

In order to have better understanding of the different simulations, a matrix is designed and shown in Table 3-4. Four simulations, named Sim1, Sim2, Sim3 and Sim4, were computed. Sim1 is the initial simulation which uses material from literature, geometry as designed and loading condition as in Figure 2-18. Sim2 changes material properties to the actual tube material. Sim3 changes one more variable which is geometry. Finally, Sim4 changes all three variables. In all four simulations, the articulation structure is loaded from 0 to ~14 N and then unloaded back to 0 N. Also, all simulations assume quasi-static loading and consider large deformation. The stress-strain hysteresis loop is recorded and compared with experiment result in section 3.2.3.

Table 3-4 Modified simulation groups with different properties.

	Sim1	Sim2	Sim3	Sim4
Material-Literature	✓			
Geometry-Designed	✓	✓		
Loading Condition-Simulation	✓	✓	✓	
Material-Manufacturer		✓	✓	✓
Geometry-Fabricated			✓	✓
Loading Condition-Experiment				✓

3.2.2 Experiment

An experiment is designed and carried out to test the compliant articulation structure under free articulation in order to verify the FEA results. The experiment was performed using a dynamic mechanical analyzer RSA-G2 at room temperature. The articulation structure sits in a dead hole and is fixed by a set screw (Figure 3-3). During this quasi-static experiment, the force gauge will move to apply a compressive force on one side of the ring. The test is performed for a complete loading and unloading cycle. Every time the force is incremented, a photo of the deformed articulation structure is taken using a camera (Canon 7D with EF-S 60mm macro lens) from the side. Meanwhile, force and displacement readings are recorded in the analyzer.

Figure 3-3 Experimental setup used to perform free articulation test.

Each image taken from the camera is imported to tpsDig, image processing software, to calculate the free articulation angle. An example is shown here to explain how the free articulation angle is calculated. First, every image was amplified untill the limitation of the software. Then, two points were picked on the edge of the load tip (Figure 3-4, point A and point B). These two points define a line, called line AB. Another point was picked on the right edge of the top ring (Figure 3-4, point C). Similarly, a second line is defined and called line AC. The software can automatically calculate the angle between these two lines (Figure 3-4, angle θ). It is assumed that the deformation of the top ring of the articulation structure is negligible. Then the free articulation angle can be calculated as $(\theta - 90^o)$. A landmark is not needed, since the angle

will not change whether the picture is zoomed in or out. Finally, a force-verse-articulation angle plot is made to compare with simulation results.

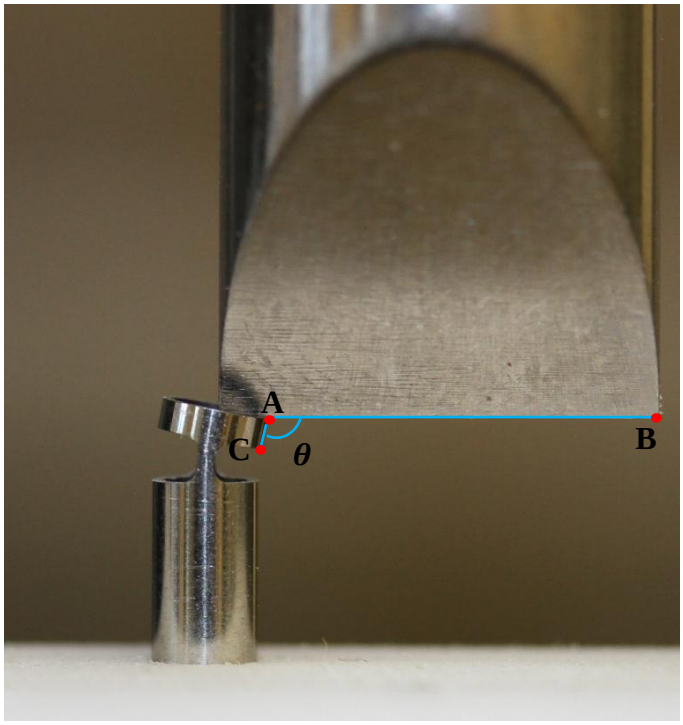

Figure 3-4 Free articulation angle is calculated from deformed articulation structure.

Design Ⅰ in Table 3-3, middle in Figure 3-1, was tested at a temperature of 25°C. In the experiment, the articulation structure was loaded from 0 to ~13.5 N and then unloaded back to 0 N. During loading period, the compressive force was increased by ~0.5 N every 60 seconds. Similarly, the force was decreased by ~0.5 N every 60 seconds during unloading. The photo was taken when the force was stabilized.

3.2.3 Results and Comparison

The experimental results and all simulations are compared in Figure 3-5. Due to the residual strain induced during fabrication, the experiment data curve does not start at zero. And the experiment curve does not close at the right end because there is residual strain caused by loading in the structure which cannot be recovered due to imperfect transformation between Austenite and Martensite. Thus the articulation structure cannot fully return to its original shape. The difference in the experiment and simulation results is attributed to the difference in material

properties, loading conditions in the experiment, and design geometry as mentioned previously. A lower phase transformation stress in Sim1 makes the loop shift to the left compared to the experimental result and other three simulations which use the same material as experimental tube. Because a low phase transformation stress (say Sim1) means that the material can reach the superelastic region with less force compared to material with high phase transformation stress (say Sim2~4). Thus, the structure in Sim1 provides larger deflection than the structure in Sim2~3 under same actuation force. The maximum articulation angle in Sim1 is larger than that in Sim2~3, because the maximum residual strain ($\bar{\varepsilon}_L$) in Sim1 larger.

It also can be seen from Figure 3-5 that results from Sim2, Sim3 and Sim4 have better agreement with experiment results than result from Sim1. However, the differences within the Sim2, Sim3 and Sim4 are very small. This means that the simulation is more sensitive to material properties than to the geometry and loading conditions. Additionally, all the simulations are performed under the assumption that the tension and compression hysteresis loops are the same. However, the characteristic phase transformation stress in compression can be as large as twice of that in tension [93], which can affect the accuracy of the simulation.

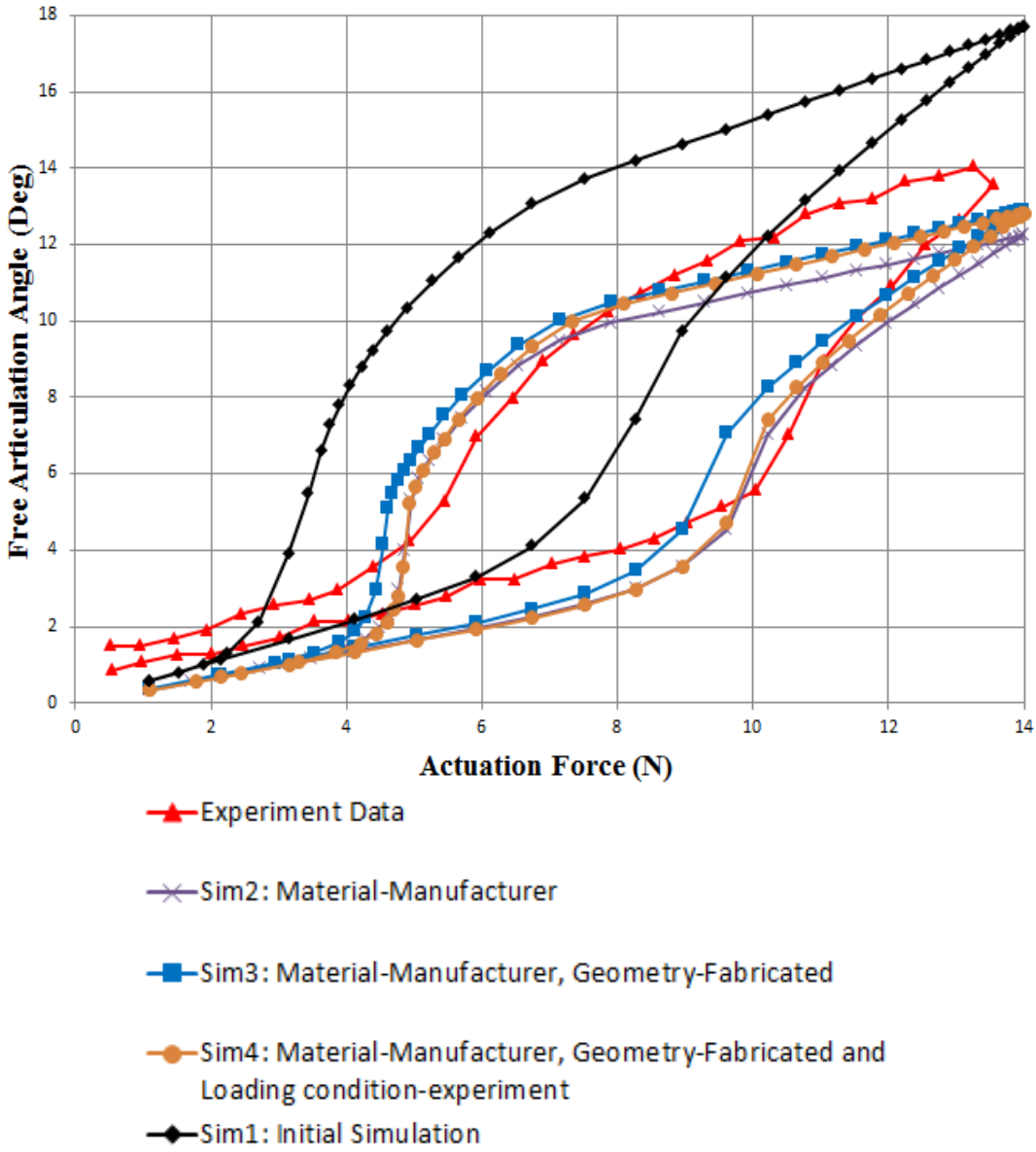

Figure 3-5 Experiment result compared to simulations listed in Table 3-4.

The actuation displacement versus free articulation angle from the experiment is also plotted in Figure 3-6. It shows that the displacement at the actuation point is nearly linearly related to the free articulation angle. This relationship could simplify the control system and help surgeons to easily manipulate the articulation structure.

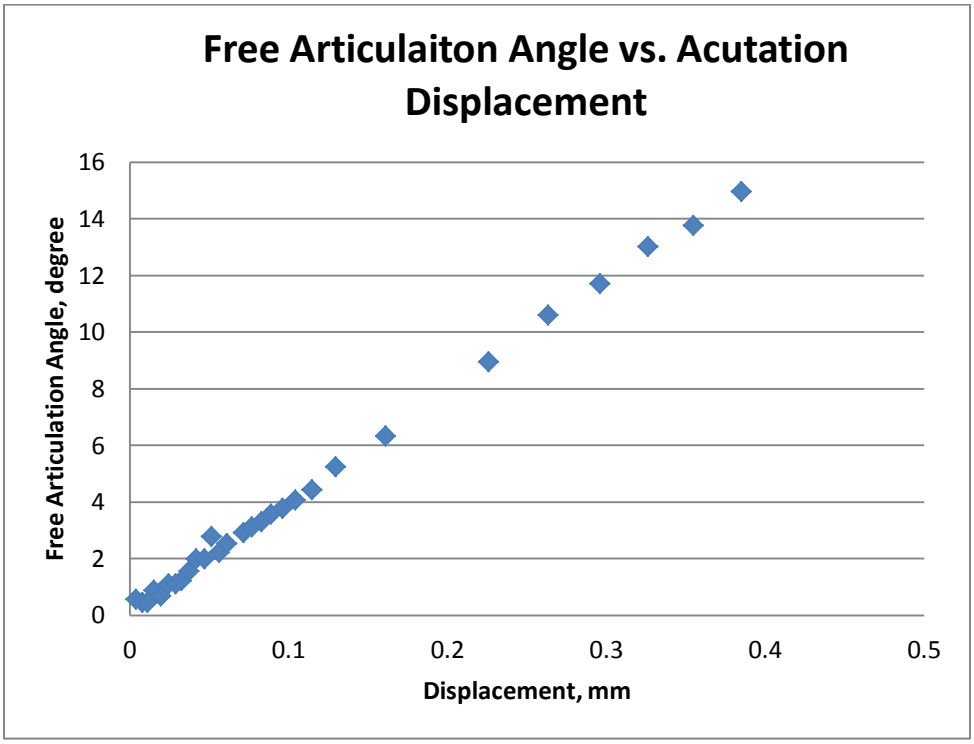

Figure 3-6 Free articulation angle versus tip actuation displacement which is a linear relationship.

3.3 Summary

This chapter has presented the fabrication process and experimental results obtained through testing the articulation structure. First, laser processing was presented. Two different laser systems were used to fabricate the articulation structure from NiTiNOL tube. Fabricated parts were compared and a better fabrication system is selected. Three designs were then fabricated using the Miyachi Unitek system. Second, three major variances, material properties, geometry and loading condition were discussed. And four simulations were run to evaluate these differences. The experiment was conducted to measure the actuation force and corresponding free articulation angle. The hysteresis behavior of actuation force and deflection angle due to the NiTiNOL material was obtained. Finally, experiment results were compared to simulations. It shows that the simulation is more sensitive to material properties than either geometric dimensions or loading conditions.

Chapter 4

Contact-aided Compliant Spine using NiTiNOL for Passive Wing Morphing

In this chapter, we will focus on another application of compliant mechanisms using superelastic NiTiNOL. A contact-aided compliant mechanism called a compliant spine has been developed in our Engineering Design and Optimization Lab at the Pennsylvania State University. The original design is manufactured using Delrin. The feasibility of using superelastic NiTiNOL is assessed in the compliant spine in order to reduce the volume, weight and increase the deflection. A new contact-aided compliant spine design using superelastic NiTiNOL will be analyzed using ANSYS. Finally, a comparison is done between compliant spine of Delrin and NiTiNOL.

4.1 Introduction

A contact-aided compliant spine was developed in the Engineering Design and Optimization Lab at the Pennsylvania State University. One of the compliant spine designs is shown in Figure 4-1, which has three compliant joints.

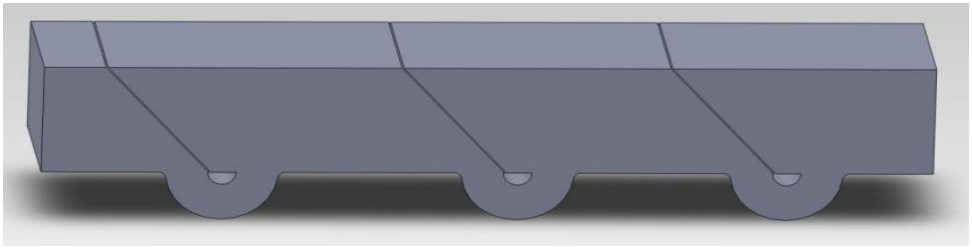

Figure 4-1 Three-joint contact-aided compliant spine (courtesy: Yashwanth Tummala).

The compliant spine will be inserted into the leading edge of the flapping wing. Two important mechanisms as mentioned in section 1.3.5 are the compliant hinge and contact pair. During upstroke, the compliant hinge provides flexibility so that the spine can deform a lot (Figure 4-2, Left). On the other hand, contact happens during downstroke so that the spine becomes much stiffer and has little deformation (Figure 4-2, Right). The compliant spine inserted

in the wing leading edge spar helps change the wing shape during flapping. So the leading edge will bend during upstroke and fully extend during downstroke.

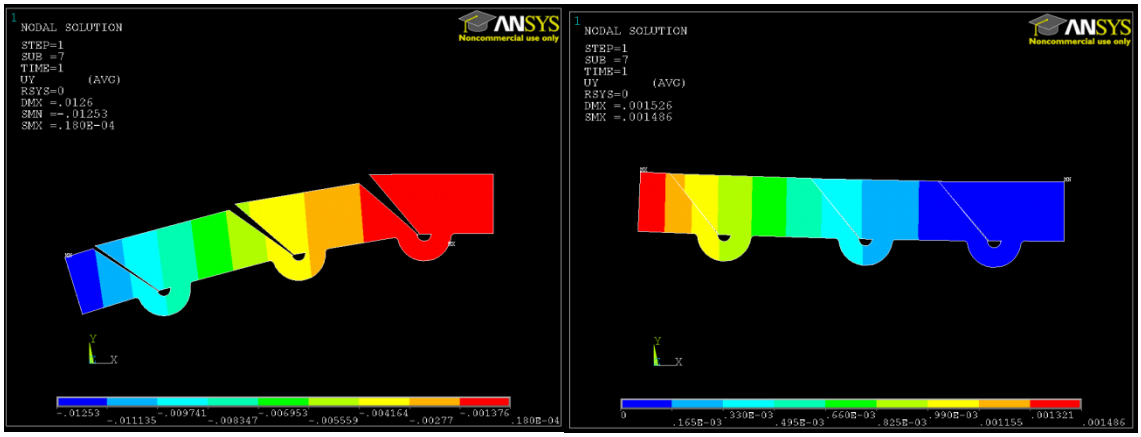

Figure 4-2 (Left) Compliant spine deformed shape during upstroke; (Right) Compliant spine deformed shape during downstroke.

This biomimetic design was found to reduce power by 45% and produce an additional 16% mean lift compared to the same ornithopter without the compliant spine [65]. However, during a recent flight test, it was found that the angle of attack had to be increased in order to compensate for the weight added by the compliant spine. Thus superelastic NiTiNOL is investigated as a means to reduce the volume and weight of the spine while providing large deflection.

4.2 Design and Model of NiTiNOL Compliant Spine

By using the contact-aided compliant spine, significant improvement has been seen in both simulation and bench test compared to the wing with the solid spar [65]. In this section, superelastic NiTiNOL will be integrated into the compliant spine to replace Delrin. First, boundary and loading conditions of the simulation will be discussed. Then previous compliant spine designs are simulated using superelastic NiTiNOL, and results are evaluated. In order to achieve a smaller and lighter design, the compliant spine is redesigned. Also, an elliptical compliant hinge is introduced to provide an even stress distribution and reduce stress concentration. Finally, NiTiNOL design is compared with optimal Delrin design.

4.2.1 Boundary and Loading Conditions

In order to estimate the loading on the compliant spine (CS), a bench top experiment was performed without the compliant spine to record the strain level in the leading edge during flapping. This experiment was carried out by our collaborators, Aimy Wissa and Dr. James Hubbard, and it is summarized here. The experiment setup is shown in Figure 4-2. In a test ornithopter with solid spars (without compliant spines) two CEA-06-125UN-120 Vishay® strain gages were mounted on the leading edge spar, with their centers at the locations where the compliant spine root and tip would be located, namely 19.75 cm and 26.1 cm from the wing root (4-3(a)). The strain gages were connected to a Vishay® 3800 strain indicator and the spars inserted in the test ornithopter wing. The ornithopter was flapped at 5 Hz, the steady level flight flapping frequency. Figure 4-3(b) shows the experiment setup. The leading edge spars of the test ornithopter are Graphlite^{TM} carbon fiber rods [104].

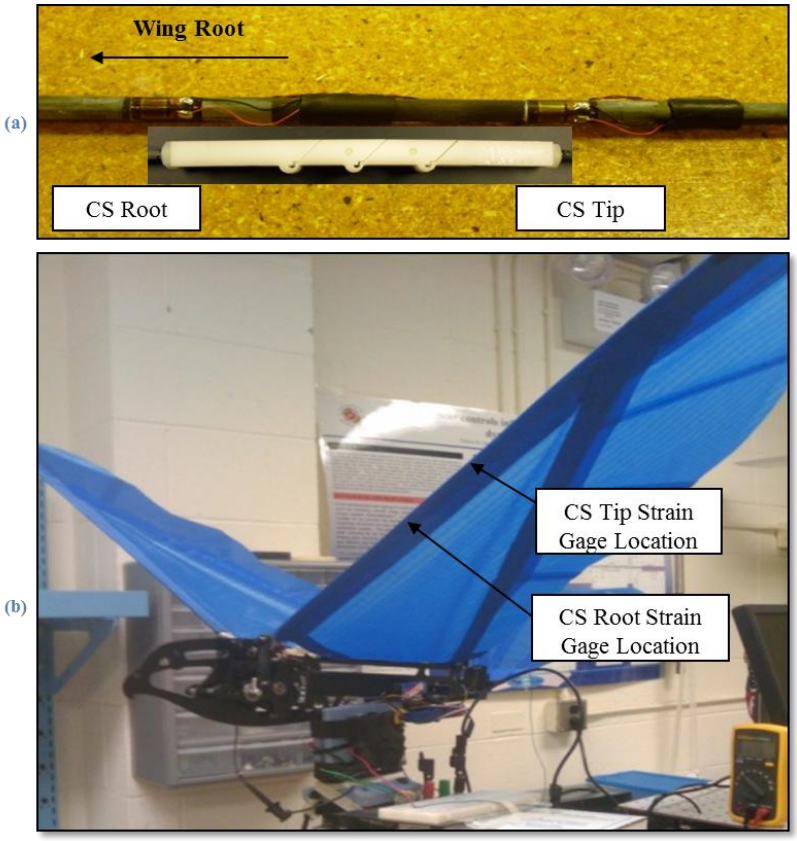

Figure 4-3 (a) Strain gages mounted on the leading edge spar at the locations of the CS root and tip. (b) Experiment setup for measuring the aerodynamic loads on the CS [105].

The bending strains in the spar at the CS root (inboard) and CS tip (outboard) locations were recorded for several flapping cycles. Figure 4-4 shows the strains measured over one flapping cycle. During the experiment it was observed that maximum compressive inboard strain was 1975.4με and the maximum compressive outboard strain was 1317.4με. These values occur at the transition point from upstroke to downstroke [105] and are recorded for future analysis.

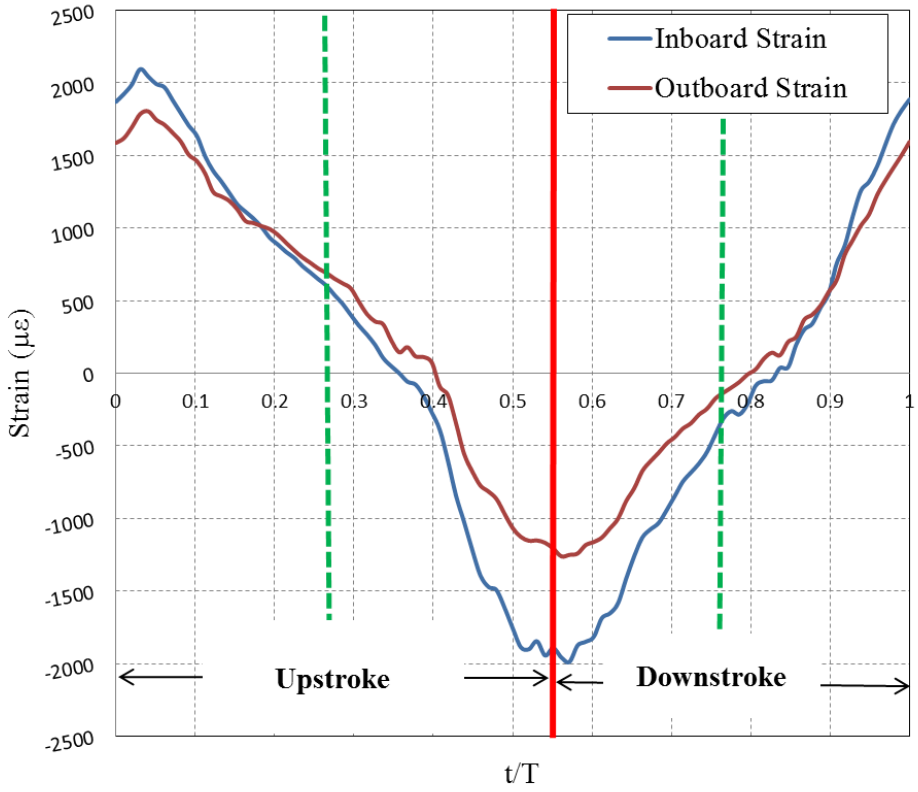

Figure 4-4 Inboard and outboard strains at the location of the CS root and CS tip [105].

The same spar was then modeled in ANSYS. This simulation was conducted by a graduate student in our lab, Yashwanth Tummala, and is summarized here. To approximate the distributed aerodynamic loads acting on the spar, a uniform load with a fixed magnitude was applied on the spar. Maximum values of strains from experiment were chosen because that will to give the maximum possible load acting on the spar and a CS design designed for such a load will be a conservative design. During the simulation, the magnitude of the dynamic load on the spar was incremented slowly until the resulting strains at corresponding locations were very close to the measured strains. The total aerodynamic load calculated from the simulation is 10 N [105]. This experiment was conducted without a CS in the spar. For a spar with a CS in it, it was assumed that the CS bears all the load acting on the spar from the root of the CS to the tip of the

spar (i.e., 10N). Another assumption was that all the load acts as a tip load on the CS instead of a distributed load on the CS. Such an assumption was made because the moment caused by a distributed load at the CS root is less than the moment caused by a tip load of same magnitude. Finally, instead of applying the tip load on the model, this load (10N) was transformed to a pure moment (0.635N·m) to avoid stress concentration at loading region.

The loading and boundary conditions in upstroke are shown in Figure 4-5. The CS is fixed at the right end and the pure moment is applied as two forces with the same magnitude but opposite directions. For downstroke, CS will also be fixed at right end. However, the moment will have opposite direction which means forces in Figure 4-5 will swap directions in downstroke simulation.

Figure 4-5 Boundary and loading condition for compliant spine in upstroke.

4.2.2 Two-joint Compliant Spine Using Superelastic NiTiNOL

Several two-joint compliant spines using superelastic NiTiNOL were simulated first to have an overall understanding. Superelastic NiTiNOL material properties from Table 2-2 NiTiNOL material properties for the dog bone specimen [67]. are used in this chapter for all the simulations. The schematic of a two-joint compliant spine is shown in Figure 4-6. Maximum Y displacement from the simulation is regarded as the deflection of the compliant spine. The compliant hinge can be defined by two semi-circles with radius r_{in} and r_{out} . Two compliant spines with different radius combinations are simulated (Table 4-1) assuming quasi static analysis using boundary and loading conditions mentioned above. Similar to compliant articulation structure, Solid 186 elements and uniform mesh are applied here.

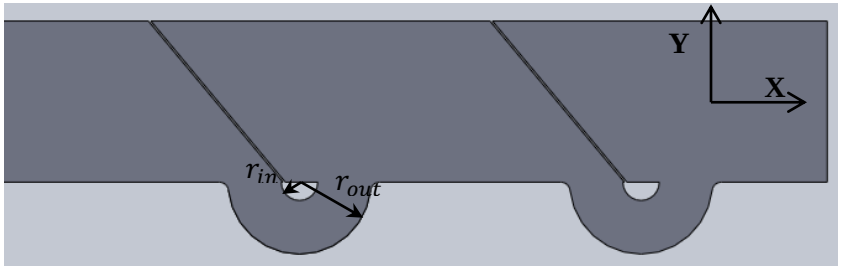

Figure 4-6 A schematic of two-joint compliant spine.

Table 4-1 Inner and outer radius of compliant hinges, unit: mm.

Compliant Spine #	r_{in}	r_{out}
1	1	4
2	3	4

The von Mises stress and Y-displacement plots for compliant spine #1 are shown in Figure 4-7. A maximum von Mises stress of 60.2 MPa and maximum Y-displacement of 1.06 mm are observed. The von Mises stress and Y-displacement plots for compliant spine #2 are shown in Figure 4-8. And a maximum von Mises stress of 175 MPa and maximum Y-displacement of 40.4 mm, which is about 3 times the deflection of the optimal Delrin design, are observed. In compliant spine #1, the compliant hinge is thick so that little deflection is obtained. However, the maximum stresses in both designs are lower than the phase transformation stress (339 MPa) of this particular superelastic NiTiNOL. It means that neither of these designs takes advantage of superelastic effect. Also, large stress concentration can be seen in stress plot of Figure 4-8. Thus new designs are needed to make good use of the superelastic effect and reduce the stress concentration.

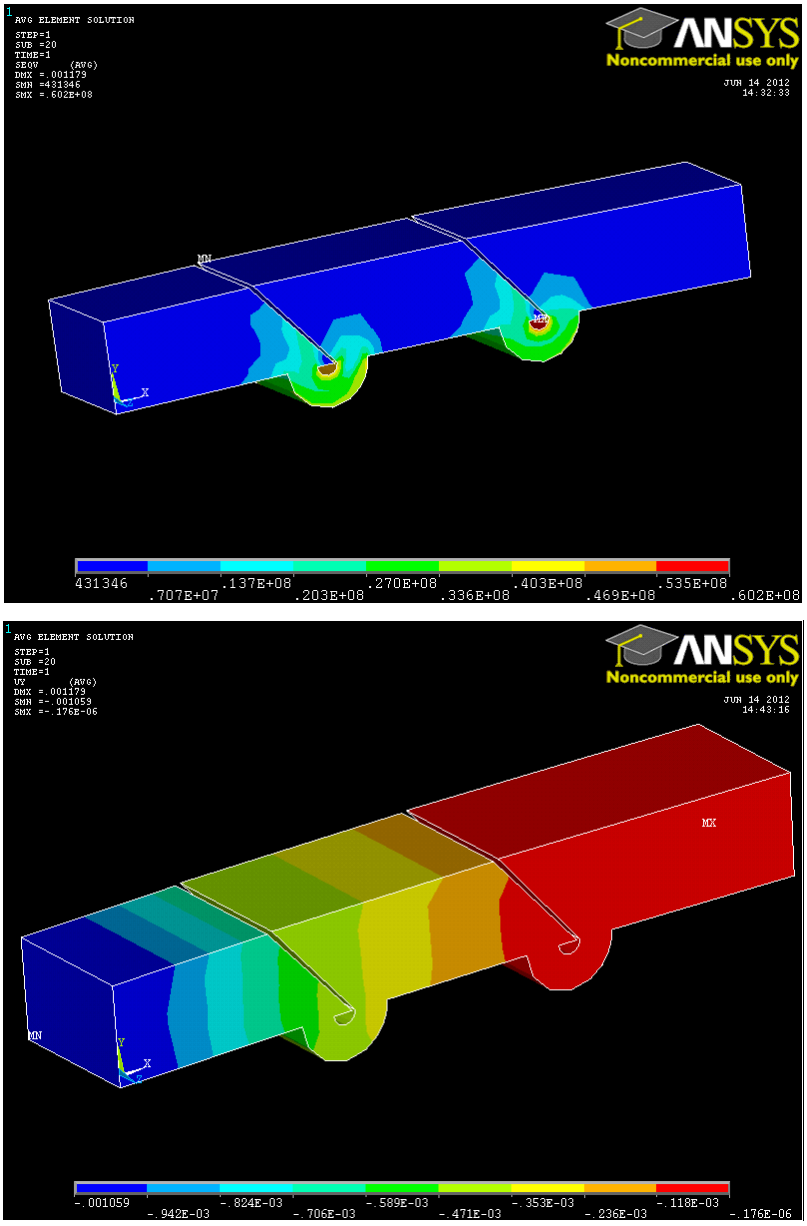

Figure 4-7 Von Mises stress and vertical displacement of compliant spine #1.

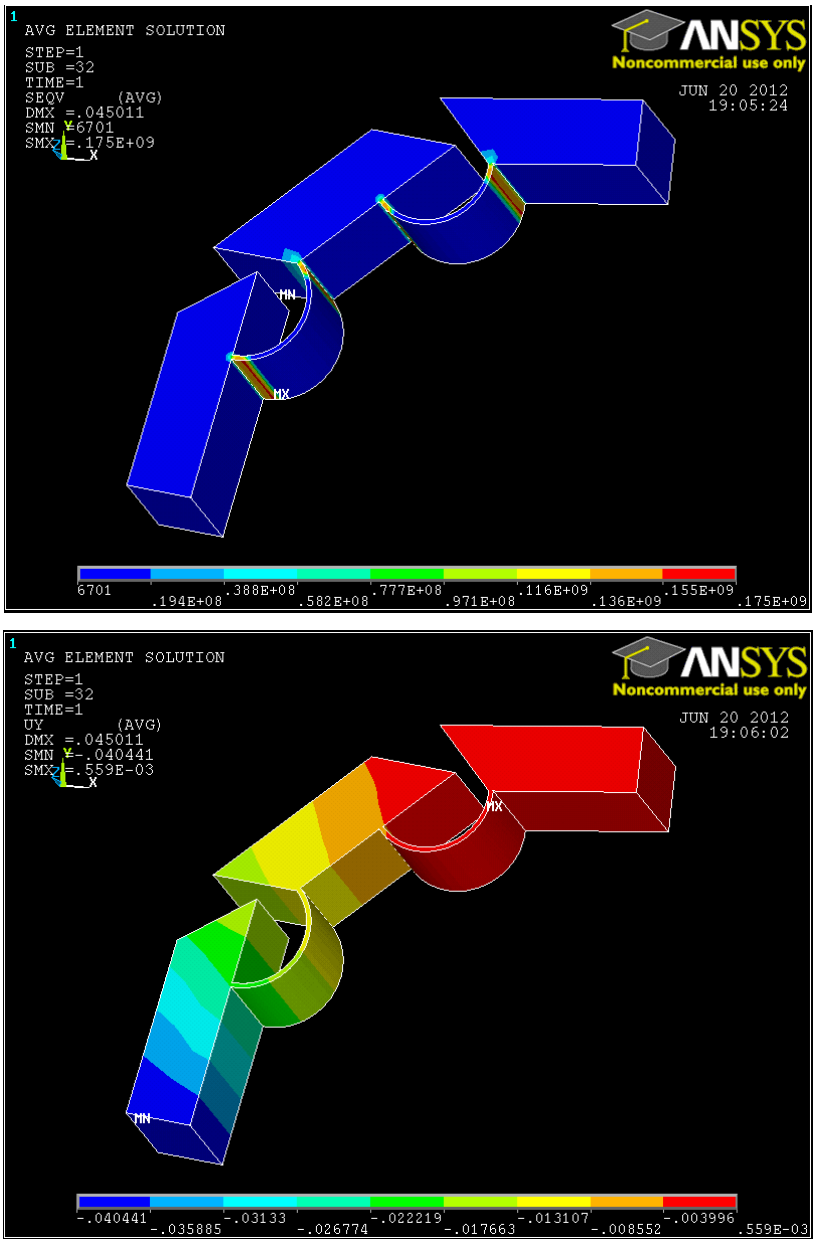

Figure 4-8 Von Mises stress and deflection plot of two-joint compliant spine #2 using superelastic NiTiNOL.

4.2.3 Modified One-joint Compliant Spine

A new compliant spine design is needed for superelastic NiTiNOL to achieve smaller size, weight and a distributed stress along the joint. From the previous simulation, it was seen that

large deflection can be achieved even without superelastic effect. Also, the deflection increases with the number of compliant joints. Thus, single joint compliant spine is investigated. In order to avoid stress concentration at the compliant hinge, an elliptical design is proposed, since the stress concentration mostly happens at the root of hinge. By enlarging the root of the hinge, the stress concentration can be reduced. A conceptual elliptical-joint compliant spine was simulated and its stress plot is shown in Figure 4-9. The simulation proved that stress concentration could be avoided by adopting elliptical shape for compliant hinge.

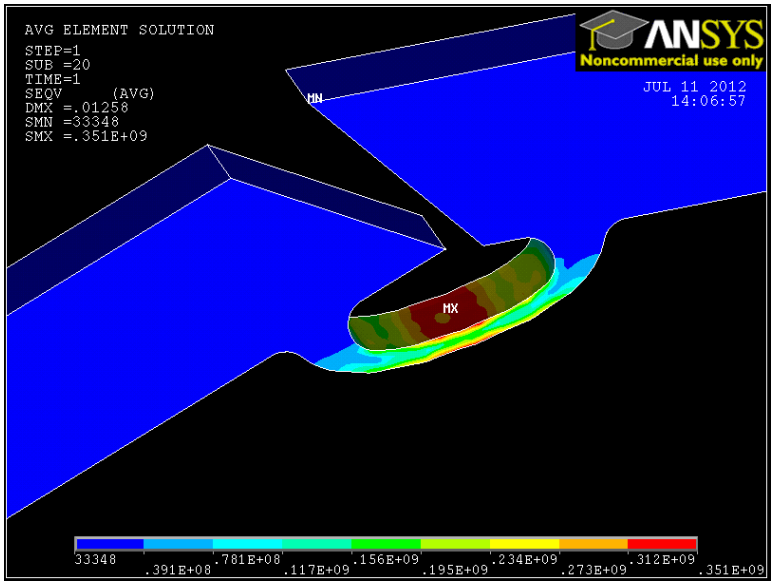

Figure 4-9 Von Mises stress plot of compliant spine with elliptical joint.

Considering the need for small size, low weight and low stress concentration, a new one-joint compliant spine with an elliptical hinge is proposed in Figure 4-10. Its geometric properties are listed in Table 4-2.

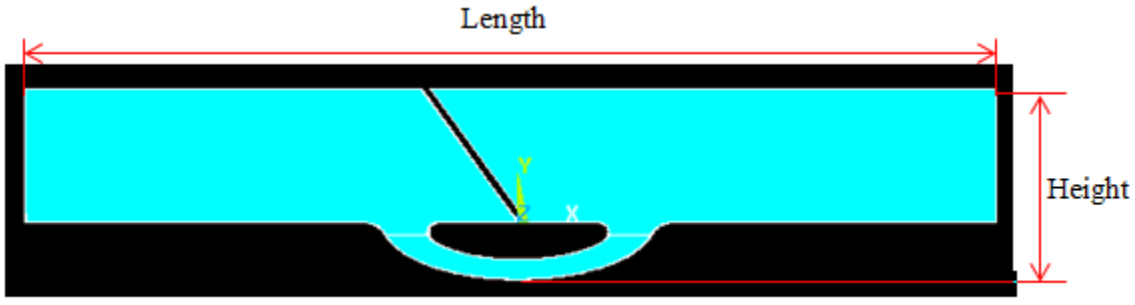

Figure 4-10 One-joint compliant spine with elliptical hinge.

Table 4-2 Design parameters for new NiTiNOL compliant spine.

Number of complaint joints	1
Length, mm	39.4
Height, mm	7.7
Thickness, mm	7.65
Joint Geometry	Ellipse Inner major axis = 4mm, Inner minor axis = 1.5 mm, Outer major axis = 5.5 mm, Outer minor axis = 2.3mm,

The new one-joint design is analyzed in ANSYS. The von Mises stress and strain plots from ANSYS simulation are shown in Figure 4-11. This new design using superelastic NiTiNOL is then compared with a similar Delrin design in Table 4-3. To reach a similar amount of deflection, NiTiNOL design needs only one joint and about 50% of the size compared to the Delrin design, while not exceeding the weight of Delrin design. The tip deflection and length ratio of the NiTiNOL design is about 150% of Delrin design, which means that NiTiNOL could make the compliant spine much smaller thus possibly lighter while still providing large deformation.

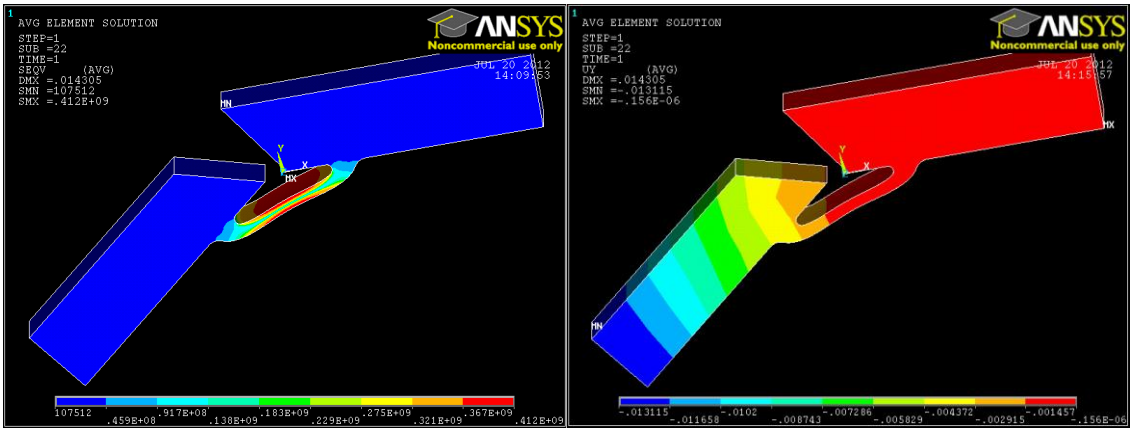

Figure 4-11 Von Mises stress (left) and strain (right) plot of the one-joint ellipse compliant spine.

Table 4-3 Comparison of NiTiNOL design and Delrin design.

	NiTiNOL Design	Delrin Design
Number of complaint joints	1	3
Upstroke Tip Deflection, mm	13.11	12.53
Upstroke Peak Stress/Allowable Stress	$\frac{412\ MPa}{440.95\ MPa} = 93.2\%$	$\frac{27.9\ MPa}{47\ MPa} = 59.4\%$
Length, mm	39.4	63.3
Height, mm	7.7	12.96
Thickness, mm	7.65	12.7
Weight, gram	10.9	11.36
Tip Deflection/Length	0.333	0.198
Downstroke Tip Deflection, mm	1.14	1.66
Downstroke Peak Stress/Allowable Stress	$\frac{179\ MPa}{440.95\ MPa} = 40.6\%$	$\frac{9.53\ MPa}{47\ MPa} = 20.3\%$

The downstroke is also analyzed, and its von Mises stress and Y-displacement plots are shown in Figure 4-12. Under the same load as the upstroke (0.635N·m), a maximum von Mises stress of 179 MPa and deflection of 1.14 mm are observed. It can be seen from the deformation plot that contact has happened at this load. The tip deflection of the NiTiNOL design is smaller than that of Delrin design, which is needed for compliant spine.

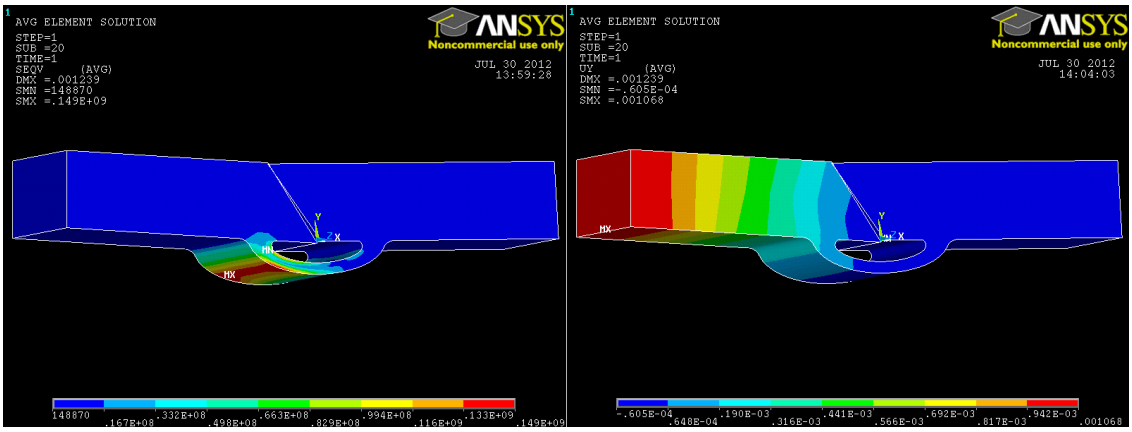

Figure 4-12 Von Mises stress and Y-displacement plots for downstroke in NiTiNOL design.

Furthermore, the stiffness of the NiTiNOL design and Delrin design are compared in Figure 4-13. When the contact happens during downstroke, the spine becomes very stiff. During upstroke the spine is relatively flexible. Thus a large amount of deflection can be achieved. From

this plot, it is also can be observed that the NiTiNOL spine exhibits a different loading and unloading path due to its hysteresis behavior, which does not occur in the Delrin design. This loading dependent behavior may help increase damping during wing flapping.

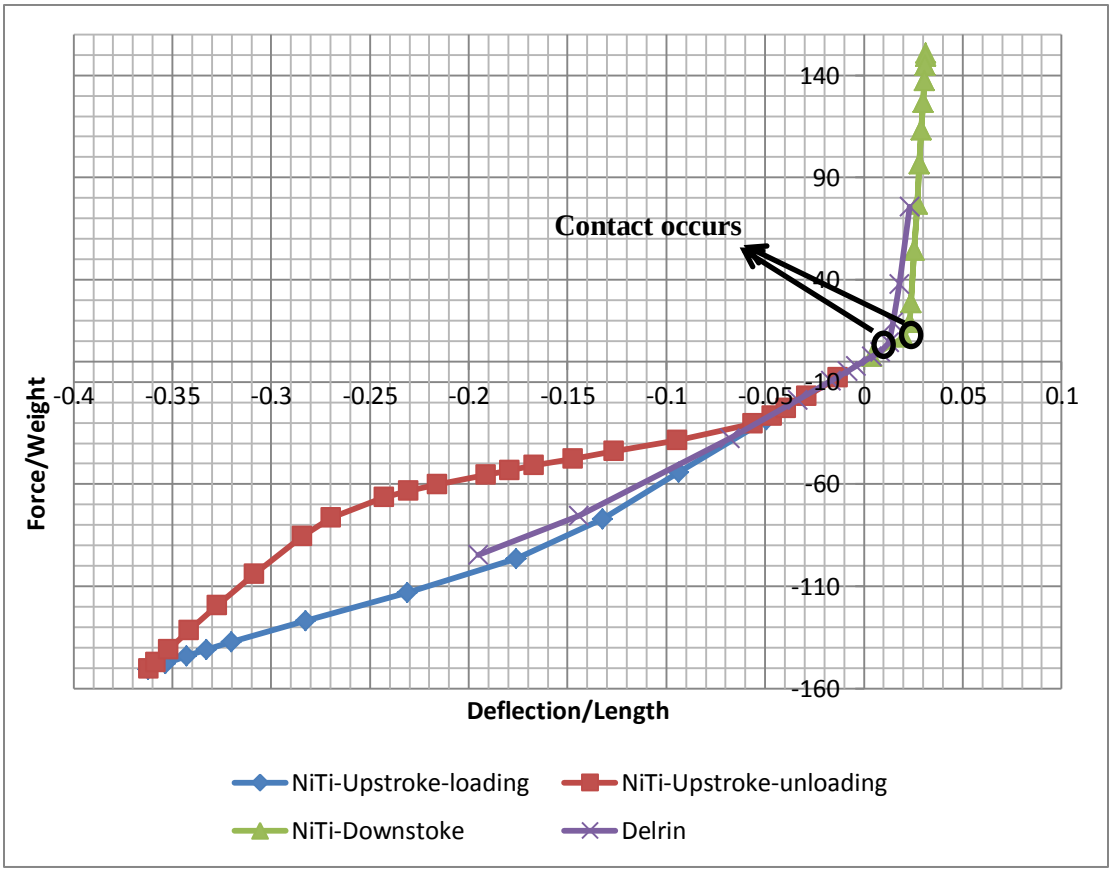

Figure 4-13 Stiffness plots of both NiTiNOL compliant spine and Delrin compliant spine, showing its non-linear force-deflection curve.

4.3 Summary

This chapter has presented a new compliant spine using superelastic NiTiNOL. The details of the new compliant spine and its modeling were discussed. The loading and boundary conditions are inherited from modeling of the Delrin designs. Simply replacing the material and using the optimal three-joint Delrin design cannot take full advantage of the superelastic effect. Therefore, considering smaller size, distributed stress and lighter weight, a new one-joint design

was proposed. Using an elliptical joint to replace the semi-circular joint, distributed stress was achieved. By comparison, the new NiTiNOL design can be about 50% smaller than Delrin design and still provide similar deflection. Also, the NiTiNOL design presents larger deflection-to-length ratio, which indicates that smaller and lighter NiTiNOL could be designed and optimized.

Chapter 5

Conclusions, Recommendations and Future Work

This thesis has presented design and analysis of compliant mechanisms using superelastic NiTiNOL. The goal of this work was to evaluate the performance of compliant mechanisms using superelastic NiTiNOL. In order to do this, two designs using superelastic NiTiNOL are modeled and analyzed. The preceding chapters of this thesis have presented a review of the related existing work, and the design and analysis, fabrication and mechanical testing. This chapter will summarize the thesis, discuss the major conclusions drawn from the work, present the contributions made, and suggest possible future work.

5.1 Summary and Conclusions

First, superelastic NiTiNOL is introduced with several applications on compliant mechanisms. Recent research on two applications, natural orifice translumenal endoscopic surgery and flapping wing UAVs or ornithopters, is reviewed. Several manufacturing methods for fabricating meso-scale product are also presented.

In order to design and simulate compliant structures using superelastic NiTiNOL, the material model was first studied using ANSYS step by step. Simple tension and bending problems were modeled using the superelastic model in ANSYS. Their results were then compared with simulation and experimental results from the literature for verification. A more complex case of orthodontic wire was modeled and verified by results from literature. Based on these studies, the element type and meshing method were obtained for modeling of superelastic NiTiNOL.

Next, a medical device application for NOTES was studied. A compliant articulation structure using superelastic NiTiNOl was proposed in order to provide non-linear accessibility for tool tips during NOTES. The compliant articulation structure is defined by six geometric parameters. Parametric variation studies were conducted to evaluate each geometric parameter based on fabrication constraints, reducing stress concentration and geometric constraints. And a

design guide with the design domain of each parameter was concluded. According to the application in NOTES, free deflection angle and blocked force were calculated for 108 NiTiNOL designs within based on the design guide. The same designs using stainless steel were also simulated and then compared with NiTiNOL results. Computational results show that using NiTiNOL can improve the maximum free deflection angle to 64.8^{o} and maximum blocked force to 24.7 N. A parameter variation study plot was obtained with free deflection angles and blocked forces of 108 designs. This plot could help designers decide the type or size of articulation structure based on the intended application. Furthermore, a buckling study was conducted to prove that all designs within the design study would not suffer buckling during surgical application.

After simulation, three sample compliant articulation structures were fabricated from NiTiNOL tube using 1064 nm Miyachi Unitek 200 W single mode fiber laser system (Sigma Laser Tube Cutter) with a repetition rate of 1.5 kHz and pulse energy of 50 mJ with a 500 micron output nozzle and 55 psi coaxially driven flow of O_2 assist gas. The fabricated articulation structure with width of 500 microns was then tested. The articulation angle was recorded in a loading cycle. The same experiment was simulated in ANSYS considering manufactured geometry, material properties and experimental loading conditions. Results show that using the material properties provided by the manufacturer results in better agreement with experiment results. It also shows that the simulation is more sensitive to material properties than the other two variations, geometry and loading conditions.

Finally, another application, flapping wings in UAV, was studied. A new contact-aided compliant spine using superelastic NiTiNOL is proposed. The new design using superelastic NiTiNOL can reduce the spine size of 50% compared to Delrin design while still providing large deflection during upstroke. The NiTiNOL design can also provide a smooth stress distribution and avoid stress concentration.

5.2 Contributions

This work has contributed to the design of compliant mechanisms using superelastic NiTiNOL. In previous literature, superelastic NiTiNOL and compliant mechanism have both been presented. NiTiNOL superelastic model was successfully modeled in ANSYS. Suitable element type and meshing approach were also obtained, which was not explicitly discussed in the

literature. Two applications, articulation structure in NOTES and compliant spine in flapping wings using superelastic NiTiNOL, were studied.

A novel compliant articulation structure was designed. In the previous literature, no articulation designs for NOTES can fit to a standard 3-mm endoscope working channel. The compliant articulation structure that was proposed is small enough to fit into a 3-mm working channel and can be fabricated within current ability. A parametric model was built and analyzed in ANSYS. The same design was improved by variable studies. And a design guide is proposed for the articulation structures used in NOTES, with the potential to be used in other articulation applications as well. A summary design plot was obtained with articulation angle and blocked force of each design from the parametric variation analysis. Designers can utilize this plot to choose a suitable articulation structure based on specific application. Furthermore, the NiTiNOL meso-scale articulation structure was fabricated using laser processing. An experiment was conducted to validate the computational model.

In the compliant spine application, a NiTiNOL design with elliptical hinge was developed. In the previous literature, the compliant spine was designed and fabricated using Delrin. The superelastic effect increases the deflection-to-length ratio which allows a smaller and lighter compliant spine. Therefore, energy cost can be reduced during flight. This high deflection-to-length ratio also might allow the compliant spine to be used in micro air vehicles.

5.3 Recommendations for Future Work

There are several ways to continue or expand the current work in the future. For the compliant articulation structure, the actuation method was not considered explicitly in the current research. One possible method is to utilize wires for mechanical actuation. Metal wires like stainless steel wire can be welded to the NiTiNOL articulation structure at two sides (Figure 5-1) using laser welding. By pulling one of the wires, the articulation structure will bend in the corresponding direction. Also, wires could be placed inside the articulation structure to avoid adding additional size to the small structure. Another method is similar but using shape memory wires. For example, NiTiNOL shape memory wires can also be welded on the articulation structure. Instead of mechanical actuation, the wire would be heated to utilize the shape memory to make the NiTiNOL wire contract or extend.

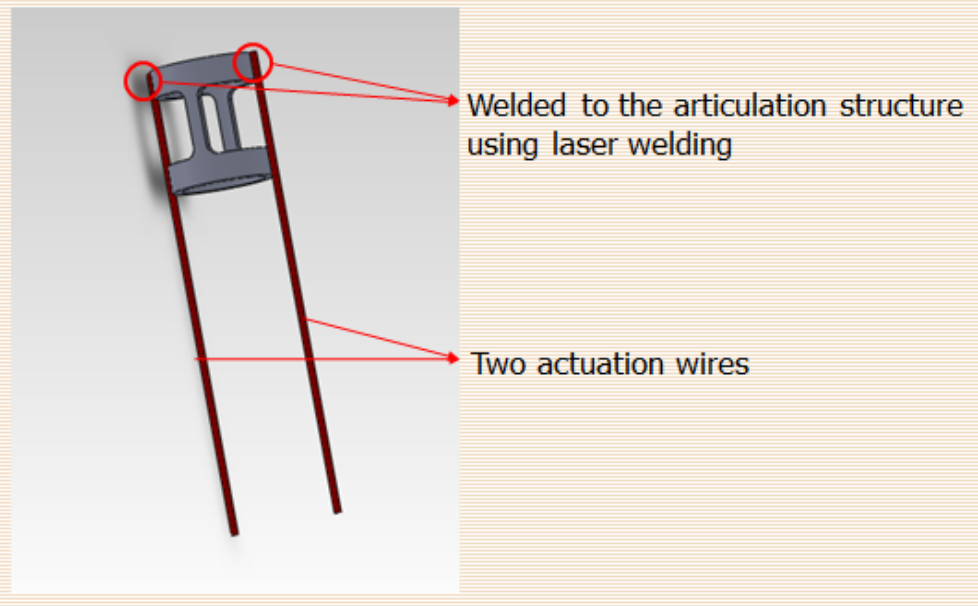

Figure 5-1 Mechanical actuation for compliant articulation structure using wires.

In the compliant spine application, it might be valuable to find the wing deformation within a flapping cycle. According to our collaborator, the load applied on the wing in one flapping cycle can be obtained in the flight test. With the load information, the wing deformation with respect to time within a flapping cycle can be calculated. Since the hysteresis behavior in superelastic NiTiNOL, we will expect highly non-linear wing shape change of the compliant spine within a flapping cycle.

NiTiNOL material properties are the next thing that can be further explored. Laser processing is utilized here for manufacturing compliant meso-scale parts. An accurate model of the material properties is needed for prediction of a new design as well as for optimization. However, how this fabrication process will affect the material properties has not been fully quantified. During laser processing, there will be heat affected zone (HAZ) due to the laser beam. Although the HAZ needs to be minimized and can be reduced by different cooling methods like using flowing water [99], it will have larger impact if the part is very small. As preliminary research, the microstructure of fabricated parts can be investigated and compared to the same NiTiNOL material before laser processing.

Finally, it would be beneficial to explore 3D additive manufacturing using laser processing in the future. Currently, laser micro machining can only fabricate 2D parts, which limits the design. Selective laser melting (SLM) process allows the rapid manufacture of

components that cannot be produced by conventional additive or subtractive techniques [106]. In the selective laser melting process, an individual part is created from powdered materials by melting them with a laser [106]. SLM could help expand design space to 3D parts. Also, considering the material properties, it would be desirable to control the laser so that desired superelastic NiTiNOL can be formed during SLM.

Appendix A: NiTiNOL Tube Tensile Test from Manufacturer

47533 Westinghouse Drive
Fremont, CA-94539
Phone: (510) 683-2000
Fax : (510) 683-2001
Web : nitinol.com

Sample Description	87349 N-202
Specimen Type	Tube
Test Method	ASTM F2516
Outer diameter	0.1210 in
Wall thickness	0.0112 in
Test Temperature (C)	22.0

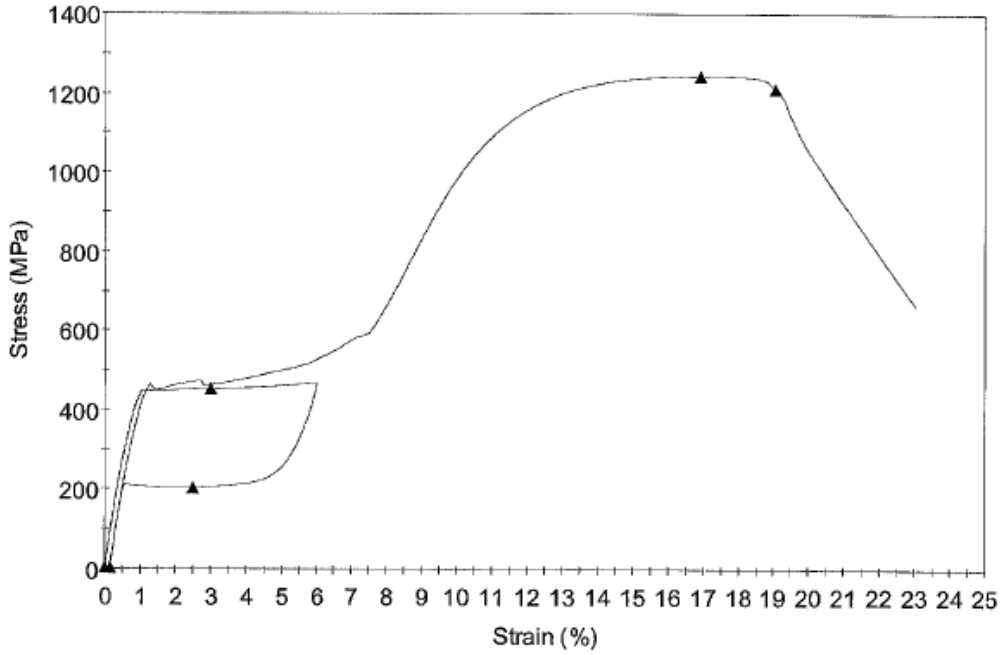

UPS @3% (MPa)	LPS @2.5% (MPa)	UTS (MPa)	Elr @7Mpa (%)	Elu (%)	El @ Break (%)	Test Temperature (C)	Af Temp.	Ext Gage ID#	Load Cell Gage ID#
455	207	1244	0.1	16.9	19.0	22.0		EXT-0002	N-175

UPS @3% (ksi)	LPS @2.5% (ksi)	UTS (ksi)
66.0	30.1	180.4

Test Performed by: ACS Date: 2/01/12

Appendix B: NiTiNOL Tube Properties from Manufacturer

NDC
47533 Westinghouse Drive
Fremont, CA 94539
USA

Phone: 510-683-2000
Fax: 510-683-2001

Sales Order: 72778

Sales Order Acknowledgement

Page: 1 of 1

Sold To:
Jiening Liu
Pennsylvania State University
314 Leonhard building,
State College PA 16802

Email: liujiening@gmail.com

Ship To:
Jiening Liu
Pennsylvania State University
314 Leonhard building,
State College PA 16802

Order Date: 1/24/2012
PO Number: credit card
NDC Sales Person: Irene Bullen
FOB: Destination
Ship Via: Fed Ex Ground
Terms: NDC Net 0 day

Line	Part Number/Description	Rev	Order Qty	Unit Price	Ext. Price
1	6970		0.20 meters	$0.0000 /1	$0.00
	SE508 T 3.073X2.505XFAB STRAIGHT GROUND				

Rel	Ship By	Quantity
1	1/25/2012	0.20

SE508 NiTi Tube, 3.07mmOD x 2.50mmID, straight, ground
OD: 0.12098" - 0.12105"
ID: 0.0990" - 0.0985"
UTS: 177.29 ksi
Upper plateau: 70.29 ksi
Permanent set: 0.32%
Elongation: 19.75
Af: -2.33C
Straightness: pass table roll test

Sample for Evaluation

Line Total:	$0.00
Line Miscellaneous Charges:	$0.00
Order Miscellaneous Charges:	$0.00
Order Total	**$0.00**

SOForm2:001:00

All Amounts are in USD

Bibliography

[1] Buehler, W. J., and Wiley, R. C. (1965). "Nickel-based alloys, Technical report." US-Patent 3174851, U.S.A.

[2] Frederick E, W. (1986). "Nitinol, a "memory" alloy in action," *Metallography*, 19(2), 257-259.

[3] Mantovani, D. (2000). "Shape memory alloys: properties and biomedical applications," *Journal of the Minerals, Metals and Materials Society*, 52(10), 36-44.

[4] Eaton-Evans, J., Dulieu-Barton, J. M., Little, E. G., and Brown, I. A. (2008). "Observations during mechanical testing of Nitinol," *Proceedings of the Institution of Mechanical Engineers, Part C: Journal of Mechanical Engineering Science*, 222(2), 97-105.

[5] Melton, K. N., and Mercier, O. (1981). "The mechanical properties of NiTi-based shape memory alloys," *Acta Metallurgica*, 29(2), 393-8.

[6] Andrea Biscarini, G. M. a. A. T. (2008). "Enhanced NiTiNOL Properties for Biomedical Applications," *Recent Patents on Biomedical Engineering*, 1, 180-196.

[7] Pelton, A. R., DiCello, J., and Miyazaki, S. (2000). "Optimisation of porcessingand properties of medical-grade nitinol wire," *Minimally Invasive Therapy Allied Technologies*, 9(2), 107-118.

[8] Ryhanen, J., Niemi, E., Serlo, W., Niemela, E., Sandvik, P., Pernu, H., and Salo, T. (1997). "Biocompatibility of nickel-titanium shape memory metal and its corrosion behavior in human cell cultures," *Journal of Biomedical Materials Research*, 35(4), 451-457.

[9] Ryhänen, J., Kallioinen, M., Tuukkanen, J., Junila, J., Niemelä, E., Sandvik, P., and Serlo, W. (1998). "In vivo biocompatibility evaluation of nickel-titanium shape memory metal alloy: Muscle and perineural tissue responses and encapsule membrane thickness," *Journal of Biomedical Materials Research*, 41(3), 481-488.

[10] Haider, W., Munroe, N., Pulletikurthi, C., Gill, P. K. S., and Amruthaluri, S. (2009). "A Comparative Biocompatibility Analysis of Ternary Nitinol Alloys," *Journal of Materials Engineering and Performance*, 18(5-6), 760-4.

[11] Shabalovskaya, S. (1996). "On the nature of the biocompatibility and on medical applications of NiTi shape memory and superelastic alloys," *Biomed Mater Eng*, 6(4), 267-289.

[12] Duerig, T., Pelton, A., and Stöckel, D. (1999). "An overview of nitinol medical applications," *Materials Science and Engineering: A*, 273-275(0), 149-160.

[13] Trepanier, C., Tabrizian, M., Yahia, L. H., Bilodeau, L., and Piron, D. L. "Improvement of the corrosion resistance of NiTi stents by surface treatments," *Proceedings of the 1996 MRS Fall Symposium, December 2, 1996 - December 5, 1996*, Boston, MA, USA, 363-368.

[14] F.D, W. (1997). "Simulation of in vivo loading conditions of nitinol vascular stent structures," *Computers & Structures*, 64(5-6), 1005-1011.

[15] Szold, A. (2006). "Nitinol: shape-memory and super-elastic materials in surgery," *Surgical Endoscopy*, 20(9), 1493-1496.

[16] Schellhammer, F., Zahringer, M., and Lackner, K. (2002). "Nitinol Micro-Forceps for Retrieval of Intravascular Objects First In Vitro Experience," *Investigative Radiology*, 37(10), 577-579.

[17] Itin, V. I., Gyunter, V. E., Shabalovskaya, S. A., and Sachdeva, R. L. C. (1994). "Mechanical properties and shape memory of porous nitinol," *Materials Characterization*, 32(3), 179-187.

[18] Stent Manufacturing, www.pulsesystems.com/stent.php, Access Date 9/25/2012.

[19] Howell, L. L. (2001). *Compliant Mechanisms*, Wiley, New York.

[20] Frecker, M. I., Ananthasuresh, G. K., Nishiwaki, S., Kikuchi, N., and Kota, S. (1997). "Topological Synthesis of Compliant Mechanisms Using Multi-Criteria Optimization," *Journal of Mechanical Design*, 119(2), 238-245.
[21] Ananthasuresh, G. K., and Kota, S. (1995). "Designing compliant mechanisms," *Mechanical Engineering*, 117(11), 93.
[22] Kota, S., Lu, K. J., Kreiner, Z., Trease, B., Arenas, J., and Geiger, J. (2005). "Design and Application of Compliant Mechanisms for Surgical Tools," *Journal of Biomechanical Engineering*, 127(6), 981-989.
[23] Frecker, M. I., Powell, K. M., and Haluck, R. (2005). "Design of a Multifunctional Compliant Instrument for Minimally Invasive Surgery," *Journal of Biomechanical Engineering*, 127(6), 990-993.
[24] Cronin, J. A., Frecker, I. V. M. I., and Mathew, A. (2008). "Design of a Compliant Endoscopic Suturing Instrument," *Journal of Medical Devices*, 2(2), 025002-9.
[25] Aguirre, M. E., Hayes, G. R., Meirom, R. A., Frecker, M. I., Muhlstein, C. L., and Adair, J. H. (2011). "Optimal design and fabrication of narrow-gauge compliant forceps," *Journal of Mechanical Design, Transactions of the ASME*, 133(8).
[26] Antolino, N. E., Hayes, G., Kirkpatrick, R., Muhlstein, C. L., Frecker, M. I., Mockensturm, E. M., and Adair, J. H. (2009). "Lost mold rapid infiltration forming of mesoscale ceramics: Part 1, fabrication," *Journal of the American Ceramic Society*, 92, S63-S69.
[27] Antolino, N. E., Hayes, G., Kirkpatrick, R., Muhlstein, C. L., Frecker, M. I., Mockensturm, E. M., and Adair, J. H. (2009). "Lost mold-rapid infiltration forming of mesoscale ceramics: Part 2, geometry and strength improvements," *Journal of the American Ceramic Society*, 92, S70-S78.
[28] Hayes, G. R. F., M. I. Adair, J. H. (2011). "Fabrication of compliant mechanisms on the mesoscale," *Mechanical Sciences*, 2(1), 129-137.
[29] Baron, T. H. (2007). "Natural orifice transluminal endoscopic surgery," *British Journal of Surgery*, 94(1), 1-2.
[30] Erica A. Moran, M. D., and Christopher J. Gostout, M.D. (2008). "Surgeons without scalpels. A review of natural orifice translumenal endoscopic surgery," *Minnesota Medicine*, 91(6), 34-37.
[31] Hussain, A., and Mahmood, H. (2008). "NOTES: current status and expectations," *European Surgery*, 40(4), 176-186.
[32] Rattner, D., and Kalloo, A. (2006). "ASGE/SAGES Working Group on Natural Orifice Translumenal Endoscopic Surgery, White Paper," *Gastrointestinal Endoscopy* 63(2), 199-203.
[33] Rattner, D. W., and SAGES/ASGE Joint Committee on NOTES. (2008). "NOTES: Where have we been and where are we going?," *Surgical Endoscopy*, 22(5), 1143-1145.
[34] (2010). "Current Status of Natural Orifice Translumenal Endoscopic Surgery (NOTES)," *Current Problems in Surgery*, 630-668.
[35] Swanström, L., M. Whiteford, and Y. Khanjanchee. (2008). "Developing essential tools to enable transgastric surgery," *Surgical Endoscopy*, 22, 600-604.
[36] Pearl, J., and Ponsky, J. (2008). "Natural Orifice Translumenal Endoscopic Surgery: A Critical Review," *Journal of Gastrointestinal Surgery*, 12(7), 1293-1300.
[37] Melvin, K. M. R. W. S. (2008). "Advanced endoscopic technologies," *Surgical Endoscopy*, 22, 1533-1546.
[38] Swanstrom, L., Kozarek, R., Pasricha, P., Gross, S., Birkett, D., Park, P.-O., Saadat, V., Ewers, R., and Swain, P. (2005). "Development of a new access device for transgastric surgery," *Journal of Gastrointestinal Surgery*, 9(8), 1129-1137.

[39] Swanström, L., P. Swain, and P. Denk. (2009). "Development and Validation of a New Generation of Flexible Endoscopie for NOTES," *Surgical Innovation*, 16(2), 104-110.
[40] Miedema, B. W., Sporn, E., Astudillo, J. A., and Thaler, K. (2008). "Epilogue: the future of NOTES," *European Surgery*, 40(3), 117-119.
[41] Auyang, E., Santos, B., Enter, D., Hungness, E., and Soper, N. (2011). "Natural orifice translumenal endoscopic surgery (NOTES): a technical review," *Surgical Endoscopy*, 25(10), 3135-3148.
[42] Moran, E., Bingener, J., Murad, F., Levy, M., and Gostout, C. (2011). "The challenges with NOTES retroperitoneal access in humans," *Surgical Endoscopy*, 25(4), 1096-1100.
[43] Bardaro, S. J., and Swanström, L. (2006). "Development of advanced endoscopes for Natural Orifice Transluminal Endoscopic Surgery (NOTES)," *Minimally Invasive Therapy & Allied Technologies*, 15(6), 378-383.
[44] Horgan, S., Thompson, K., Talamini, M., Ferreres, A., Jacobsen, G., Spaun, G., Cullen, J., and Swanstrom, L. (2011). "Clinical experience with a multifunctional, flexible surgery system for endolumenal, single-port, and NOTES procedures," *Surgical Endoscopy*, 25(2), 586-592.
[45] Chin, W. J., and Nelson, C. A. (2010). "Mechanism Designs for Natural Orifice Surgery: A Review," *ASME Conference Proceedings*, 2010(44106), 1221-1229.
[46] Lee, S., Oelschlager, B., Wright, A., Soares, R., Sinan, H., Montenovo, M., and Hwang, J. (2011). "Assessment of a simple, novel endoluminal method for gastrotomy closure in NOTES," *Surgical Endoscopy*, 25(10), 3448-3452.
[47] Moyer, M., Pauli, E., Gopal, J., Mathew, A., and Haluck, R. (2011). "Durability of the self-approximating translumenal access technique (STAT) for potential use in natural orifice translumenal surgery (NOTES)," *Surgical Endoscopy*, 25(1), 315-322.
[48] Rau, A. C., Frecker, M., Mathew, A., and Pauli, E. (2011). "Multifunctional forceps for use in endoscopic surgery-initial design, prototype, and testing," *Journal of Medical Devices, Transactions of the ASME*, 5(4).
[49] Kencana, A. P., Phee, S. J., Low, S. C., Sun, Z. L., Huynh, V. A., Ho, K. Y., and Chung, S. C. "Master and slave robotic system for natural orifice transluminal endoscopic surgery," *2008 IEEE Conference on Robotics, Automation and Mechatronics (RAM), 21-24 Sept. 2008*, Piscataway, NJ, USA, 296-300.
[50] Phee, S. J., Kencana, A. P., Huynh, V. A., Sun, Z. L., Low, S. C., Yang, K., Lomanto, D., and Ho, K. Y. (2010). "Design of a master and slave transluminal endoscopic robot for natural orifice transluminal endoscopic surgery," *Proceedings of the Institution of Mechanical Engineers, Part C (Journal of Mechanical Engineering Science)*, 224(C7), 1495-503.
[51] Phee, S. J., Low, S. C., Huynh, V. A., Kencana, A. P., Sun, Z. L., and Yang, K. "Master and slave transluminal endoscopic robot (MASTER) for natural orifice transluminal endoscopic surgery (NOTES)," *2009 31st Annual International Conference of the IEEE Engineering in Medicine and Biology Society. EMBC 2009, 3-6 Sept. 2009*, Piscataway, NJ, USA, 1192-5.
[52] Lehman, A. C., Wood, N. A., Dumpert, J., Oleynikov, D., and Farritor, S. M. "Dexterous miniature in vivo robot for NOTES," *2nd Biennial IEEE/RAS-EMBS International Conference on Biomedical Robotics and Biomechatronics, BioRob 2008, October 19, 2008 - October 22, 2008*, Scottsdale, AZ, United states, 244-249.
[53] Lehman, A. C., Wood, N. A., Dumpert, J., Oleynikov, D., and Farritor, S. M. "Robotic natural orifice translumenal endoscopic surgery," *2008 IEEE International Conference on Robotics and Automation, ICRA 2008, May 19, 2008 - May 23, 2008*, Pasadena, CA, United states, 2969-2974.

[54] Abbott, D. J., Becke, C., Rothstein, R. I., and Peine, W. J. "Design of an endoluminal NOTES robotic system," *2007 IEEE/RSJ International Conference on Intelligent Robots and Systems, IROS 2007, October 29, 2007 - November 2, 2007*, San Diego, CA, United states, 410-416.

[55] Augirre, M. E. (2011). "Design and Optimization of Narrow-Gauged Contact-Aided Compliant Mechanisms for Advanced Minimally Invasive Surgery ", The Pennsylvania State University, State College.

[56] Rau, A. C. (2010). "Design of a multifunctional forceps for use in endoscopic surgery," Pennsylvania State University, State College.

[57] Hayes, G. R. (2011). "Mesoscale Fabrication and Design," The Pennsylvania State University, State College, PA, U.S.A.

[58] Rau, A. C., and Frecker, M. (2009). "A review of scaling and performance considerations for articulating technologies," *ASME 2009 Conference on Smart Materials, Adaptive Structures and Intelligent Systems*, 271-280.

[59] Loeve, A. J., Bosma, J. H., Breedveld, P., Dodou, D., and Dankelman, J. (2010). "Polymer Rigidity Control for Endoscopic Shaft-Guide `Plastolock' --- A Feasibility Study," *Journal of Medical Devices*, 4(4), 045001-6.

[60] Yi, C., Tanaka, S., and Hunter, I. W. "Disposable endoscope tip actuation design and robotic platform," *Engineering in Medicine and Biology Society (EMBC), 2010 Annual International Conference of the IEEE*, 2279-2282.

[61] McEuen, S., Tzeranis, D., Hemond, B., Dirckx, M., Lee, L., and Slocum, A. (2008). "Design of an endoscopic full-thickness lesion removal device," *Journal of Medical Devices*, 2(1), 015002-1.

[62] Harada, K., Tsubouchi, K., Fujie, M. G., and Chiba, T. "Micro Manipulators for Intrauterine Fetal Surgery in an Open MRI," *Robotics and Automation, 2005. ICRA 2005. Proceedings of the 2005 IEEE International Conference on*, 502-507.

[63] Jha, A. K., and Kudva, J. N. (2004). "Morphing aircraft concepts, classifications, and challenges," *Proceedings of SPIE - The International Society for Optical Engineering*, 213-224.

[64] Shyy, W., Berg, M., and Ljungqvist, D. (1999). "Flapping and flexible wings for biological and micro air vehicles," *Progress in Aerospace Sciences*, 35(5), 455-505.

[65] Wissa, A. A., Tummala, Y., Hubbard, J. E., Jr., and Frecker, M. I. (2012). "Passively morphing ornithopter wings constructed using a novel compliant spine: design and testing," *Smart Materials and Structures*, 21(9), 094028 (9 pp.).

[66] Fenelon, M. A. A., and Furukawa, T. (2010). "Design of an active flapping wing mechanism and a micro aerial vehicle using a rotary actuator," *Mechanism and Machine Theory*, 45(2), 137-146.

[67] Buselli, E., Valdastri, P., Quirini, M., Menciassi, A., and Dario, P. (2009). "Superelastic leg design optimization for an endoscopic capsule with active locomotion," *Smart Materials and Structures*, 18(1), 015001 (8 pp.).

[68] Takahata, K. (2009). "Chapter 10 Micro-Electro-Discharge Machining Technologies for MEMS," *Micro Electronic and Mechanical Systems*, 143-164.

[69] Myunghoon, S., Mohanchandra, K. P., Yohan, L., and Carman, G. P. (2008). "Development of a 'bi-layer lift-off' method for high flow rate and high frequency Nitinol MEMS valve fabrication," *Journal of Micromechanics and Microengineering*, 18(7), 075034 (10 pp.).

[70] Muhammad, N., Whitehead, D., Viejo, F., Abuaisha, R., Boor, A., Oppenlaendar, W., Liu, Z., and Li, L. "Picosecond laser fabrication of nitinol for coronary stent applications," *29th International Congress on Applications of Lasers and Electro-Optics, ICALEO 2010, September 26, 2010 - September 30, 2010*, Anaheim, CA, United states, 1474-1479.

[71] http://www.photonics.com/Article.aspx?AID=43367. (2012). "Laser Machining Drives Improvements in Medical Devices." Lynn Savage.
[72] Elahinia, M. H., Hashemi, M., Tabesh, M., and Bhaduri, S. B. (2012). "Manufacturing and processing of NiTi implants: A review," *Progress in Materials Science*, 57(5), 911-946.
[73] Tanaka, K., and Nagaki, S. (1982). "A THERMOMECHANICAL DESCRIPTION OF MATERIALS WITH INTERNAL VARIABLES IN THE PROCESS OF PHASE TRANSITIONS," *Ingenieur-Archiv*, 51(5), 287-299.
[74] Liang, C., and Rogers, C. A. (1997). "One-dimensional thermomechanical constitutive relations for shape memory materials," *Journal of Intelligent Material Systems and Structures*, 8(4), 285-302.
[75] Brinson, L. C. (1993). "One-dimensional constitutive behavior of shape memory alloys: Thermomechanical derivation with non-constant material functions and redefined martensite internal variable," *Journal of Intelligent Material Systems and Structures*, 4(2), 229-242.
[76] Boyd, J. G., and Lagoudas, D. C. (1996). "A thermodynamical constitutive model for shape memory materials. I. The monolithic shape memory alloy," *International Journal of Plasticity*, 12(6), 805-42.
[77] Huang, M., and Brinson, L. C. (1998). "A multivariant model for single crystal shape memory alloy behavior," *Journal of the Mechanics and Physics of Solids*, 46(8), 1379-409.
[78] Siredey, N., Patoor, E., Berveiller, M., and Eberhardt, A. (1999). "Constitutive equations for polycrystalline thermoelastic shape memory alloys. I. Intragranular interactions and behavior of the grain," *International Journal of Solids and Structures*, 36(28), 4289-315.
[79] Auricchio, F., Taylor, R. L., and Lubliner, J. (1997). "Shape-memory alloys: macromodelling and numerical simulations of the superelastic behavior," *Computer Methods in Applied Mechanics and Engineering*, 146(3-4), 281-312.
[80] Brinson, L. C., Lammering R. (1993). "Finite element analysis of the behaviour of shape memory alloys and their applications," *International Journal of Solids and Structures*, 30, 3261-3280.
[81] Qidwai, M. A., and Lagoudas, D. C. (2000). "Numerical implementation of a shape memory alloy thermomechanical constitutive model using return mapping algorithms," *International Journal for Numerical Methods in Engineering*, 47(6), 1123-68.
[82] Govindjee, S., and Miehe, C. (2001). "A multi-variant martensitic phase transformation model: formulation and numerical implementation," *Computer Methods in Applied Mechanics and Engineering*, 191(3-5), 215-38.
[83] Jung, Y., Papadopoulos, P., and Ritchie, R. O. (2004). "Constitutive modelling and numerical simulation of multivariant phase transformation in superelastic shape-memory alloys," *International Journal for Numerical Methods in Engineering*, 60(2), 429-460.
[84] ANSYS. (2009). "Theory Reference for the Mechanical APDL and Mechanical Applications, Release 12.1." 4.6 Shape Memory Alloy.
[85] Milton A. Deherrera, N. D. (2004). "Finite Element Analysis of a Percutaneous Stent-Mounted Heart Value." ABAQUS Users' Conference, 209-223.
[86] Seong, M., Mohanchandra, K. P., Lin, Y., and Carman, G. P. "Development of a high flow-rate/high operating frequency Nitinol MEMS valve," *Sensors and Smart Structures Technologies for Civil, Mechanical, and Aerospace Systems 2008, 10 March 2008*, USA, 69322-1.
[87] Wu, W., Qi, M., Liu, X.-P., Yang, D.-Z., and Wang, W.-Q. (2007). "Delivery and release of nitinol stent in carotid artery and their interactions: A finite element analysis," *Journal of Biomechanics*, 40(13), 3034-3040.

[88] Terriault, P., Theriault, P., Brailovski, V., and Gallo, R. (2006). "Finite element modeling of a progressively expanding shape memory stent," *Journal of Biomechanics*, 39(15), 2837-44.
[89] Hongwei, M., and Chongdu, C. (2007). "Application of superelasticity of SMAs in bolted end-plate connection," *Key Engineering Materials*, 3039-42.
[90] ANSYS. (2009). "Structural Analysis Guide, Release 12.1." 8.4.1.8 Shape Memory Alloy Material Model.
[91] Gall, K., Sehitoglu, H., Chumlyakov, Y. I., and Kireeva, I. V. (1999). "Tension–compression asymmetry of the stress–strain response in aged single crystal and polycrystalline NiTi," *Acta Materialia*, 47(4), 1203-1217.
[92] Reedlunn, B., Churchill, C., Nelson, E., Daly, S., and Shaw, J. (2011). "Bending of Superelastic Shape Memory Alloy Tubes," *ASME 2011 Conference on Smart Materials, Adaptive Structures and Intelligent Systems* 249-258.
[93] Siddons, D. J., and Moon, J. R. (2001). "Tensile and compression performance of superelastic NiTi tubing," *Materials Science and Technology*, 17(9), 1073-8.
[94] ASTM, E. E. M. (2011). "Standard Test Methods for Tension Testing of Metallic Materials." ASTM International, West Conshohocken, PA, 2011, 10.1520/E0008_E0008M-11.
[95] Ballew, W., and Seelecke, S. "A comparison of FE beam and continuum elements for typical nitinol stent geometries," USA, 72890R (11 pp.).
[96] Auricchio, F. (2001). "A robust integration-algorithm for a finite-strain shape-memory-alloy superelastic model," *International Journal of Plasticity*, 17(7), 971-90.
[97] Rahman, M. A., Jinhao, Q., and Junji, T. (2001). "Buckling and postbuckling characteristics of the superelastic SMA columns," *International Journal of Solids and Structures*, 38(50-51), 9253-65.
[98] Wu, M. H. "Fabrication of Nitinol Materials and Components," *2001 International Conference on Shape Memory and Superelastic Technologies*, Kunming, China, 285-292.
[99] Leitz, K.-H., Redlingshöfer, B., Reg, Y., Otto, A., and Schmidt, M. (2011). "Metal Ablation with Short and Ultrashort Laser Pulses," *Physics Procedia*, 12, Part B(0), 230-238.
[100] Schuessler, A., Strobel, M. "Status and Trends of Nitinol Micromachining Techniques," *International Conference on Shape Memory and Superelastic Technologies*, Pacific Grove, CA, USA, 135-141.
[101] Haferkamp, H., von Busse, A., Bunte, J., Fargas, M., Hustedt, M., and Paschko, S. (2004). "Machining of superelastic instruments for minimal invasive surgery with ultrashort laser pulses," *2004 Proceedings of the SPIE - The International Society for Optical Engineering*, 5340, 146-152.
[102] Zheng, H., Zareena, A., Huang, H., Lim, G. (2003). "Studies of Femtosecond Laser-Processed Nitinol," *Materials Science Forum*, 437-438, 277-280.
[103] Huang, H., Zheng, H. Y., and Lim, G. C. (2004). "Femtosecond laser machining characteristics of Nitinol," *Applied Surface Science*, 228(1–4), 201-206.
[104] Wissa, A., Tummala, Y., Hubbard Jr, J. E., Frecker, M., and Brown, A. (2011). "Testing of novel compliant spines for passive wing morphing," *ASME 2011 Conference on Smart Materials, Adaptive Structures and Intelligent Systems*, 733-742.
[105] Tummala, Y. (2012). "Design and Optimization of Contact Aided Compliant Mechanisms with Tailorable Nonlinear Stiffness," The Pennsylvania State University, State College.
[106] Adam T. Clare, P. R. C., Sean Davies, Christopher J. Sutcliffe, Sozos Tsopanos. (2008). "Selective Laser Melting of High Aspect Ratio 3D Nickel-Titanium Structure Two Way Trained for MEMS Applications," *Int J Mech Mater Des*, 4, 181-187.